# MODELING THE MAMMALIAN OVARY: A CELL-BASED COMPUTATIONAL MODEL OF EARLY OVARIAN DEVELOPMENT IN MICE AND PRELIMINARY DATA FOR A MODEL OF FOLLICULOGENESIS IN RHESUS MONKEYS.

A Thesis

Presented to

The Institute of Environmental Health

Oregon Health & Science University

In partial fulfillment of the requirements for the degree

Master of Science

By

Hannah M. Wear

August 2016

# TABLE OF CONTENTS

## LIST OF TABLES

## LIST OF FIGURES

## ACKNOWLEDGEMENTS

I would like to first thank my graduate advisor, Dr. Karen Watanabe, for all of the guidance, support, and patience. Her advice has inspired my research in computational modeling and made this thesis possible. I would additionally like to thank Dr. Mary Zelinski for her assistance with the model of folliculogenesis, providing access to ovarian tissue histology. I am grateful for the enthusiasm about the research from Dr. Bruce Schnapp and advice from Dr. Peter Zuber. Also, I greatly appreciate the assistance with coding in the model from Annika Eriksson, PhD candidate. Last, I want to thank all those who have supported and encouraged my thesis research.

This research was funded in part by Alternatives Research & Development Foundation. This research was also funded in part by the U.S. Army's Environmental Quality and Installations 6.1 Basic Research program, and contracts WP912HZ-15-A-0044 and W912HZ-15-C-0002. Opinions, interpretations, conclusions, and recommendations are those of the author(s) and are not necessarily endorsed by the U.S. Army.

## ABSTRACT

Proper development and function of the ovary is vital for female mammalian reproduction. Development of the ovary plays an important role in the formation of the ovarian follicle reserve, which governs the female reproductive lifespan. One of the main functions in the developed ovary is the maturation of ovarian follicles, a process known as folliculogenesis. Exposure to reproductive toxicants and reproductive diseases can cause adverse reproductive outcomes, possibly leading to infertility. Computational modeling is a cost-effective, efficient, and humane method for studying the effects of disease and toxicant exposure to ovarian development and function. Understanding normal development and function of the ovary can aid in the study of the effects from disease and toxicant exposure. Computational models of normal ovarian development and function can be utilized as a baseline for modeling toxicity and disease, to make predictions and hypotheses about ovarian physiology, and as a learning resource. Despite its importance in reproduction, a model for mammalian early ovarian development does not exist. Likewise, a model of the preantral stages of folliculogenesis does not exist. The purpose of this thesis was to construct a model of early ovarian development, spanning the origin primordial germ cells to formation of primordial follicles, in mice and to gather data to be used for the development of a model of the preantral stages of folliculogenesis, the generation of secondary follicles from primordial follicles, in rhesus macaque. Early ovarian development was chosen to be modeled in mice due to the abundance of data in the literature compared to other mammalian species. Data gathering for a model of the preantral stages of folliculogenesis was undertaken in rhesus macaques due to the fidelity

with human ovarian physiology and the role of rhesus macaques in reproductive disease research.

Before the construction of a computational model, a graphical model of the molecular signaling interactions involved in early ovarian development in mice was constructed. Both graphical and computational models of early ovarian development in mice were constructed from data in the literature. CompuCell3D, a cell-based modeling software, was utilized for computational model construction. Experimental images and cell abundances reported in the literature were used to verify the model. Hypothesized mechanisms about primordial germ cell migration and germ cell nest breakdown were tested and incorporated into the ovarian development model. A sensitivity analysis was run to assess sensitivity of model parameters. Data gathering for a model of the preantral stages of folliculogenesis in rhesus macaques produced resources for preliminary model development and highlighted missing information necessary for model construction. The early ovarian development model and the preliminary model development of the preantral stages of folliculogenesis provide baseline information for the development of models that can be used to assess effects from exposure to reproductive toxicants and diseases. The ovarian development model can continue to be extended to incorporate additional known molecular signaling. Future work after the development of the folliculogenesis model will focus on extending the model to include the antral stages of folliculogenesis.

# Chapter 1. Introduction

Reproduction is key for species survival. Sexual reproduction is dependent on the fusion of two distinct specialized cells, the sperm and the ovum. Proper development and function of the mammalian ovary is vital for successful female reproduction (Edson, Nagaraja, & Matzuk, 2009; Richards & Pangas, 2010). The main function of the ovary is the production of a healthy, mature, fertilizable egg that is ready to be ovulated, also known as a preovulatory oocyte (Richards & Pangas, 2010). Production of a preovulatory oocyte begins with the development of the ovary. In mammals, ovarian development and the formation of ovarian follicles, an oocyte surrounded by supporting somatic cells, occurs predominantly during the embryonic period. The number of ovarian follicles formed during ovarian development governs the size of the follicle reserve, and thus the length of a female's reproductive lifespan (Wallace & Kelsey, 2010; Wilkosz, Greggains, Tanbo, & Fedorcsak, 2014). Recent studies have debated the role of ovarian germ stem cells contributing to the follicle reserve in adult mammals, however it remains unclear if the ovarian germ stem cells are able to produce progenitor germ cells that develop to mature ovarian follicles (D. Bhartiya, Unni, Parte, & Anand, 2013; Zhang et al., 2012). The formation and maturation of ovarian follicles greatly influences the success of female reproduction; disruption to these processes can lead to adverse reproductive outcomes.

In mice, early ovarian development occurs almost entirely during the embryonic phase, continuing to two days after birth; primordial germ cells (PGCs), the precursors to oocytes, undergo development to become primordial follicles in the growing ovary (Edson et al., 2009). Early ovarian development has two phases, 1) the origin and migration of PGCs to the gonadal ridge (Fig. 1.1 and Fig. 1.2) the development of PGCs

to oocytes in the differentiating gonad. Expression of pre-PGC markers, bone morphogenetic proteins (BMPs) and wingless-type mouse mammary tumor virus integration site family member 3 (WNT3), are first detected in the mouse ovary on embryonic day 5.5 (E5.5) (Edson et al., 2009; Ying, Qi, & Zhao, 2002). From E5.5 to E7.5, PGCs maintain pluripotency and promote histone methylation through Brachyury expression to maintain specification from somatic cells (Ohinata et al., 2005). PGCs are observed in the posterior region of the mouse embryo on E7 via staining for the unique biomarker, alkaline phosphatase (Fig. 1.2) (Ginsburg, Snow, & McLaren, 1990). PGCs remain in the posterior region until migration signals are activated.

PGC migration to the gonadal ridge (future gonad) is governed by alpha chemokine receptor and ligand-tyrosine kinase receptor interactions: stromal cell-derived factor 1-chemokine receptor type 4 (SDF1-CXCR4) and stem cell growth factor Kit-stem cell growth factor Kit receptor (KIT ligand-c-KIT) (Gu, Runyan, Shoemaker, Surani, & Wylie, 2009; K. Molyneaux & Wylie, 2004; K. A. Molyneaux et al., 2003; Runyan et al., 2006). SDF1 and KIT ligand are expressed by the gonadal ridge and hindgut (future gastrointestinal tract), respectively. PGCs are observed experimentally migrating along the hindgut to the gonadal ridge (Francis & Lo, 2006; K. A. Molyneaux et al., 2003; Yeom et al., 1996). On E11.5-12.5, PGCs reach the gonadal ridge and migration halts.

In the gonad, PGCs undergo rapid proliferation, then expression of female sex differentiation factors begins. PGCs enter meiosis, halting at prophase I, developing to oocytes through retinoic acid 8 (STRA8) expression (Achermann, Meeks, & Jameson, 2001; Anderson et al., 2008). See Chapter 2 for more information about the molecular signaling governing female sex differentiation in mice. On E14, aryl hydrocarbon

chemicals bind to the aryl hydrocarbon receptor (AhR), activating apoptotic processes in oocytes (Benedict, Lin, Loeffler, Peterson, & Flaws, 2000). The onset of apoptosis is associated with the formation of germ cell nests, which are composed of several oogonia connected due to incomplete cytokinesis and are surrounded by granulosa cells (Fig. 1.3) (Lei & Spradling, 2013b). At birth, the maternal estrogen supply is cutoff and total estrogen in the embryo decreases. The decrease in maternal estrogen supply is associated with granulosa cells invading the germ cell nests and surrounding an individual oocyte, to form primordial follicles. Primordial follicle formation occurs from birth to postnatal day 2 (P2) and is the last process in early ovarian development in mice (Edson et al., 2009). Primordial follicles remain quiescent in the ovary until activated through folliculogenesis.

Folliculogenesis encompasses the growth and maturation of an ovarian follicle, which is composed of a single oocyte surrounded by supporting somatic cells (Gosden & Lee, 2010). Folliculogenesis begins with the activation of a primordial follicle and finishes with the development of a preovulatory follicle. The early stages of folliculogenesis (primordial to preantral follicle stage) involve preantral development and the later stages (small antral to preovulatory stage) are dependent upon hormone cycles (Dunlop & Anderson, 2014; Oktem & Urman, 2010). In mammals, preantral folliculogenesis continues after the formation of primordial follicles, while antral folliculogenesis does not occur until the onset of puberty when hormonal signaling begins. The work in this thesis focuses on the preantral stages of folliculogenesis; for more information on the antral stages of folliculogenesis, please refer to (Dunlop & Anderson, 2014; Gosden & Lee, 2010; Oktem & Urman, 2010; van den Hurk & Zhao, 2005).

Folliculogenesis in non-human primates has been studied due to its similarity to folliculogenesis in humans (Dizerega & Hodgen, 1981). Though rhesus macaques are not the most-well studied species for folliculogenesis, folliculogenesis research in this thesis focuses on the rhesus macaque because of its importance in studying reproductive diseases. In preantral folliculogenesis, the morphological development of follicles involves the growth of the oocyte and proliferation of surrounding somatic cells (i.e. granulosa cells and theca cells). The first process in folliculogenesis is the activation of primordial follicles and development to primary follicles (Erickson, 1995). Primordial follicles are composed of an oocyte surrounded by a single layer of squamous granulosa cells (Fig. 1.4). In rhesus macaques, androgens have been shown to play a role in the activation of primordial follicles to primary follicles *in vitro* (Vendola et al., 1999). Activation is detected by a growth in the oocyte and a change in the shape of the surrounding single layer of granulosa cells from squamous to cuboidal. The primary morphological distinction between primordial follicles and primary follicles is the shape of the granulosa cells (Fig. 1.4). The oocyte in a primary follicle continues to grow and the layer of granulosa cells proliferate. Follicles are considered secondary follicles when two or more layers of granulosa cells are present in the follicle and theca cells begin to surround the outer layer of granulosa cells (Fig. 1.4). Both granulosa and theca cells are follicular cells involved in steroidogenesis. Secondary follicles are the last stage of preantral folliculogenesis. The *in vivo* molecular mechanisms involved in follicle growth in rhesus macaques still need to be experimentally verified. In mammals, folliculogenesis and early ovarian development play crucial processes that directly affect female

reproduction; understanding these processes and their potential stressors is highly important.

Abnormal ovarian development or folliculogenesis can lead to adverse reproductive outcomes (Donnez & Dolmans, 2013; Richards & Pangas, 2010; Sarraj & Drummond, 2012). Understanding mechanisms involved in normal ovarian development and folliculogenesis aid in the prediction of adverse outcomes associated with exposure to reproductive toxicants. The National Academy of Sciences released a report in 2007 called Toxicity Testing in the 21st Century: a vision and a strategy, which proposes an alternative to traditional toxicity testing methods in animals, by combining *in vitro* assays with computational models to make predictions about adverse outcomes caused by exposure to toxicants (Krewski et al., 2010). Computational models, combined with *in vitro* assays, are a more efficient, cost-effective, and humane method compared to toxicity testing in animals. Though computational models cannot replace all lab experiments, they have the ability to test hypotheses, suggest and refine experiments, and integrate and unify knowledge (Brodland, 2015). Before computational models can be developed to predict adverse outcomes, a computational model simulating the normal biological processes must first be developed. In addition to providing a baseline for the development of computational models for toxicology and disease, models of normal biological processes can be utilized for testing hypothesis and highlight research areas lacking in data.

Computational models can be used to study molecular interactions that govern cell behavior. Angiogenesis, tumor growth, and epithelial to mesenchymal transition, and cell sorting have been simulated using CompuCell3D, which is based on the Cellular Potts

model (aka Glazier-Graner-Hogeweg algorithm) (Abdulla, Imms, Dillenseger, Schleich, & Summersa, 2011; Gao, Tangney, & Tabirca, 2011; Graner & Glazier, 1992; Scianna & Preziosi, 2012; Shirinifard et al., 2009). The Cellular Potts model is a lattice-based computational modeling method used to simulate cellular behavior (Merks & Glazier, 2005). The Cellular Potts model utilizes mathematical equations to explain tissue-scale biological phenomenon that are mediated by cell interactions. Cells in the Cellular Potts model are assigned parameters defining cell attributes (e.g. cell types, cell volumes, cell to cell contact adhesion). The mathematical equations used in Cellular Potts modeling describe how various cell attributes contribute to the energy of the system (see Equation 3 Appendix A). The energy is not indicative of the physical energy of cells, but rather is used to produce cell behaviors in the model. Constraints on the defined (or target) volume for cells and the contact energy between cells at each bordering pixel location (Fig. 1.5) influence the effective energy in the model. Compucell3D (CC3D) software uses Cellular Potts modeling to simulate multi-cell biological systems at the single cell scale (M. H. Swat et al., 2012).

CC3D consists of a main computational kernel, a tool for creating the initial layout of the lattice used in the model (CellDraw), a user-friendly script editor and code generator (Twedit++-CC3D), and a graphical output tool for visualizing the simulation (CC3D Player) (M. H. Swat et al., 2012). CellDraw is used to create a picture interchange file format (PIFF) that describes the initial layout of the lattice in the model. The lattice in CC3D is made up of pixels where cells are defined as a group of pixels; the PIFF defines lattice size, cell size, and the location of cell types in the lattice. Scripts describing the functions used in the model to define cell attributes are generated using Twedit++-CC3D.

There are two types of functions defined in the model, Plugins and Steppables, which perform operations on pixels and cells, respectively. Operations performed on a pixel controls whether the pixel cell type will remain the same or change to a different cell type, known as a pixel copy attempt (Fig. 1.6). Pixel copy attempts are governed by changes in the energy calculations determined from model functions, also called the effective energy change. Plugins calculate effective energy changes for every pixel copy attempt for all pixels in the domain per Monte Carlo Step (MCS). Steppables, performed every MCS, update cell parameters, store simulation data and results, and solve partial differential equations. CC3D has preset functions to describe cell behaviors (e.g. Mitosis Steppable); preset functions, which are adapted for particular model, by defining parameter values (e.g. mitotic rate). CC3D also allows the ability for users to write code for new functions not preset in the software (e.g. Cell Abundance Tracking Steppable used in the model of early ovarian development in mice—see Chapter 3). For more information about CC3D functions used for this research see Chapter 3 and Appendix A. Simulations of the model can then be observed in the CC3D Player.

Models can be developed at different biological scales (e.g. cell scale, organ scale) depending on the purpose of the model. Early ovarian development and folliculogenesis are best modeled at the cellular scale, because these biological processes occur at the cellular level (Gosden & Lee, 2010; Sarraj & Drummond, 2012). No cell-based computational models exist for mammalian early ovarian development or for the preantral stages of folliculogenesis. The purpose of this thesis research was to develop the first computational model of early ovarian development in mice (*Mus musculus*) and to

gather and review data for the development of a cell-based computational model of the preantral stages of folliculogenesis in rhesus macaque (*Macaca mulatta*).

Early ovarian development was modeled in mice due to the availability of data in the literature for mice. Before the construction of the model was undertaken, a conceptual model and review of molecular signaling during early ovarian development in mice was conducted (see Chapter 2). The purpose of conceptual model construction was to produce a theoretical framework of the most important mechanisms governing early ovarian development in mice that could be used for the development of a cell-based computational model. The aims of model development were to develop a model of normal ovarian development in mice (as a basis for future development of a model to predict effects of toxicant exposure), test hypothesized biological mechanisms using the model, and to highlight research areas lacking in data (see Chapter 3). Assessment of the model parameters was done using a univariate sensitivity analysis (see Chapter 4) and by comparison with data in the literature (e.g. experimental images).

Rhesus macaque was chosen as the species for gathering data to use for the development of a model of the preantral stages of folliculogenesis. Experiments in rhesus macaque and other non-human primates are generally expensive and time consuming. Computational models can be used as a tool to mitigate some of the issues associated with such experiments, thus rhesus macaques were selected for development of the model. The goals of data gathering were to identify data that can used to define parameters for a model of folliculogenesis through literature searches and histological analysis of ovarian tissue (see Chapter 5).

The cell-based computational model of early ovarian development in mice and the data gathering for the development of a model of the preantral stages of folliculogenesis provide a baseline for simulating normal ovarian development and function. The early ovarian development model can be used as a tool to test hypotheses, utilized as a teaching resource, and provides a framework for the development of a model to predict adverse outcomes from toxicant exposure. Folliculogenesis data can be used to develop a cell-based computational model of the preantral stages of folliculogenesis and contributes information that has not yet been reported in the literature for rhesus macaque. Research presented in this thesis provides a foundation for cell-based modeling of the mammalian ovary.

# Chapter 2. A conceptual model of early ovarian development in mice

## 2.1. Project Involvement

Before the construction of a computational model for early ovarian development in mice occurred, a conceptual model of molecular signaling involved in ovarian development was created. Conceptual model development was done in collaboration with Matthew McPike, MS and Karen Watanabe, PhD. My involvement in the project was assisting in the literature review, writing the conceptual model manuscript for publication, and development of Figs. 2.1 and 2.4. This chapter was published in the Journal of Ovarian Research (Wear, McPike, & Watanabe, 2016).

## 2.2. Introduction

Successful reproduction in males and females is vital to survival and is dependent on several factors including development of reproductive organs. For females, normal development of the ovaries includes multiple cell types (e.g., oogonia, theca and granulosa cells) that provide structure and function vital for reproduction. Ovarian development in mammals can be split into two phases, 1) growth of the ovary and establishment of the founding primordial follicle pool and 2) maturation of follicles and release of a fertilizable egg starting at puberty. The first phase of ovarian development, or early ovarian development, occurs predominantly during the embryonic period. Explicitly, early ovarian development in mice begins on embryonic day five (E5) and finishes on postnatal day two (P2). Development of the ovaries is a highly regulated

process dependent on a series of molecular signaling factors. Disruption in the signaling can lead to adverse reproductive outcomes, such as a smaller primordial follicle pool, incomplete development of follicles, and failure of normal sexual differentiation (Edson et al., 2009; Sarraj & Drummond, 2012). Recognizing the importance of molecular signaling and the associated phenotypic outcomes is vital for understanding ovarian development.

Visual representations can be helpful for understanding complex concepts like molecular signaling networks. We created a visual representation of early ovarian development to highlight key molecular signaling processes and corresponding phenotypic outcomes. Many factors are involved in development of the gonad, however we chose to only include signaling events that are critical to producing viable oocytes and those that are susceptible targets for reproductive toxicity (e.g. aryl hydrocarbon receptor). Starting on embryonic day five (E5) and ending on postnatal day two (P2), molecular events and phenotypic outcomes that occur on a given day within corresponding cell types are shown in the figures (Fig. 2.2, 2.3, 2.5-2.8). All materials used to develop the figures were based on data from primary literature. Studies were chosen based on research quality and the species studied. In our review, early ovarian development in mice was divided into five different stages: 1) origin of germ cells and maintenance of pluripotency; 2) germ cell migration; 3) sex differentiation; 4) formation of germ cell nests; and 5) germ cell nest breakdown and primordial follicle formation.

A few days after birth, neo-oogenesis and formation of primordial follicles were traditionally believed to permanently cease, meaning the germ cell pool size in mammalian females is fixed at birth. Emerging studies have shown evidence for the

presence of active germ stem cell types, very small embryonic-like stem cells (VSELs), female germline stem cells (FGSCs), ovarian stem cells (OSCs), ovarian germ stem cells (OGSCs), etc., in the postnatal ovary in several mammalian species, with the potential to contribute to the germ cell pool (Bukovsky, 2011; Guo, Li, Wang, He, & Zheng, 2016; Lu et al., 2016; Pacchiarotti et al., 2010). VSELs have been observed in studies with similar characteristics to developing primordial germ cells (e.g. maintenance of pluripotency) giving rise to progenitors that are associated with increased meiosis and appearance of primordial follicles in the adult mouse ovary (Deepa Bhartiya, Sriraman, Gunjal, & Modak, 2012; Szotek et al., 2008), however other studies continue to claim absence of active germ cells in the postnatal ovary (Lei & Spradling, 2013a; Zhang et al., 2014; Zhang et al., 2012). Though the controversy over the role of OSCs is important in understanding the size of the germ cell pool and female reproduction, it is outside the scope and timeline of our focus on early ovarian development in mice.

### 2.3. Origin of germ cells and maintenance of pluripotency factors (E5 to E7)

Primordial germ cells (PGCs) are diploid cells that give rise to the germline in both males and females (Edson et al., 2009; McLaren & Chuva de Sousa Lopes, 2009; Saitou, 2009). They are the precursors of oocytes and spermatozoa in the ovaries and testes, respectively. Six PGCs arise on E5 from a cell population located in the extraembryonic ectoderm (Fig. 2.1a). PGCs undergo mitosis, dividing into a larger population of undifferentiated cells. By E7, about 40 PGCs are detected in the primitive streak in the cleft between the yolk sac and developing allantois near the posterior of fthe

extraembryonic mesoderm tissue (Fig. 2.1b) (De Sousa Lopes, Hayashi, & Surani, 2007). Extraembryonic tissues in mammals are important for fetal development, though they do not remain attached after birth. PGCs are the only cell type to originate outside of embryonic tissue that remains in the animal after birth. It is hypothesized that PGCs are located external to embryonic tissue to avoid differentiation signals and maintain pluripotency (Lanner, 2014).

The initial appearance of six PGCs is identified by increased bone morphogenetic protein (BMP) and proto-oncogene wingless-type mouse mammary tumor virus integration site family member 3 (WNT3) levels (Fig. 2.2). BMPs (i.e., BMP2, BMP4, and BMP8) are extracellular signaling peptides that bind to mothers against decapentaplegic homologs 1 and 4 (SMAD1/4) and SMAD4/5 receptors (Edson et al., 2009; Ying et al., 2002). It is not known which BMP binds to which dimeric SMAD receptor. Studies have shown BMP4 alone is sufficient for PGC development, however BMP2 and 8 enhance the quantity of viable PGCs formed (Lawson et al., 1999; Ohinata et al., 2009; Ying & Zhao, 2001). Activation of the Wnt3/β-catenin signaling pathway is also necessary to activate transcription factors that promote pluripotency and prevent differentiation (Saitou, 2009). WNT3 binds to the Frizzled-related receptor protein (FRIZZLED) on the surface of the PGC activating the β-catenin pathway, which leads to promotion of pluripotency factors through activation of Brachyury (Aramaki et al., 2013). Binding of BMPs and WNT3 to their receptors also leads to the activation of Brachyury, an intracellular transcription factor.

From E6 to E7, Brachyury activates proteins that promote expression of pluripotency factors and histone methylation (Aramaki et al., 2013). Histone methylation in the PGC

helps maintain pluripotency by allowing transcription factors more access to regions of DNA. Brachyury activates positive regulatory domain zinc finger protein 1 (PRDM1), a transcription repressor, which blocks transcription of differentiation factors homeobox A1 (HOXA1) and HOXB1 (Ohinata et al., 2005). PRDM1 additionally promotes activity of nanos homolog 3 (NANOS3), which leads to the expression of genes (e.g. sex determining region Y-box 2 (*Sox2*), octamer-binding transcription factor 4 (*Oct4*), and homeobox transcription factor (*Nanog*)) involved in maintaining pluripotency (Kurimoto et al., 2008). PRDM1 can form a dimer with protein arginine n-methyltransferase 5 (PRMT5), a histone methyltransferase, to dimethylate the genome at the arginine 3 residue of histone 4 preventing gene silencing (Ancelin et al., 2006). Freeing the genome is necessary for meiotic division to produce functional gametes. PRDM1 and PRDM14, also a transcription factor, are able to upregulate each other to stimulate PGC development. Similar to PRDM1, PRDM14 plays a role in cellular pluripotency and is also involved in epigenetic reprogramming. PRDM14 activates developmental pluripotency associated 3 (DPPA3), a pluripotency factor, and enhances expression of *Sox2*, *Oct4*, and *Nanog* (Elliman, Wu, & Kemp, 2006). DPPA3, SOX2, OCT4, NANOG, and NANOS3 are all involved in the continued pluripotency of PGCs (Elliman et al., 2006; Rizzino, 2009; Tsuda et al., 2003). Protein lin-28 homolog A (LIN28) plays a role in maintaining pluripotency by forming a complex with a small inhibitory mRNA (siRNA), lethal 7 (LET7), to free *Prdm1* genes for transcription (Viswanathan, Daley, & Gregory, 2008). When LET7 is not bound to LIN28, LET7 binds to *Prdm1* inhibiting transcription and reducing pluripotency.

On E7, an increase in the levels of alkaline phosphatase (ALP) is observed in the Golgi apparatus of PGCs (Ginsburg et al., 1990). The dark staining properties of ALP allow PGCs to be identified in the embryo quite easily at this stage. It is unknown why ALP is expressed; however localization in the Golgi implies active protein synthesis. Studies of ALP knockout mice do not show inhibited PGC development or migration (MacGregor, Zambrowicz, & Soriano, 1995), which suggests that ALP is not critical for the process of ovarian development, but is important for identifying PGCs at this stage.

### 2.4. PGC migration to the gonadal ridge (E8 to E9)

PGCs originate in extraembryonic tissue posterior to the location of the future gonad, thus cellular migration must occur for the PGCs to become a part of the gonad in both males and females. PGC migration begins a couple days after the expression of pluripotency factors and initiation of histone methylation. Two schools of thought exist with respect to mitosis during PGC migration to the gonadal ridge: (i) before migration occurs, the founding population of PGCs must receive proper signals to halt mitosis and initiate factors necessary for cellular motility and migration (Sekl et al., 2007); and (ii) PGCs continue to proliferate during PGC migration (K. A. Molyneaux et al., 2003; Runyan et al., 2006). The two hypotheses about PGC proliferation during migration were tested using the computational model (Chapter 3). On E7.5 a population of PGCs is formed in the posterior region of the embryo awaiting migration signals. β-catenin production reduces E-Cadherin, decreasing PGC to PGC cellular adhesion (Fig. 2.3) (Bendel-Stenzel, Gomperts, Anderson, Heasman, & Wylie, 2000; Di Carlo & De Felici,

2000). The decrease in adhesion allows the PGCs to become more motile and enhances their ability to migrate. PGCs have been observed to adopt polarized morphology with cytoplasmic protrusions just prior to migration, yet the factors causing these morphological changes are still unknown.

PGC migration begins on E8 and is mainly controlled through two separate ligand-receptor chemoattractant signaling interactions. Ligand proteins involved in PGC migration are secreted from the gonadal ridge and from the hindgut. The gonadal ridge is the region of tissue that will become the future gonad and the hindgut will develop into part of the gastrointestinal tract. The gonadal ridge secretes a ligand, stromal cell-derived factor 1 (SDF1), that binds to the chemokine receptor type 4 (CXCR4) receptor on the PGC causing the PGCs to migrate to the gonadal ridge (McCoshen & McCallion, 1975; K. A. Molyneaux et al., 2003). SDF1-CXCR4 mediated migration of PGCs was first observed in zebrafish embryos and later confirmed in mice (Doitsidou et al., 2002; Knaut et al., 2003).

PGCs do not migrate in a direct path to the gonadal ridge, but rather move along the basal surface of the hindgut until they are parallel with the gonadal ridge and then migrate to the gonadal ridge (Fig. 2.4) (K. Molyneaux & Wylie, 2004). The hindgut secretes the stem cell growth factor Kit (KIT) ligand (also called Steel factor) that binds to the KIT receptor (also called c-Kit) on the PGC. KIT ligand-receptor signaling plays a role in the motility of PGCs during migration as opposed to dictating the direction of migration (Gu et al., 2009). Activation of the KIT signaling pathway also activates a tyrosine kinase and promotes survival factors like NANOS3 and dead end protein

homolog 1 (DND1), that prevent apoptosis and halt mitosis of PGCs during migration (Cook, Coveney, Batchvarov, Nadeau, & Capel, 2009).

Survival factors are necessary to ensure that a sizable population of PGCs reach the gonadal ridge. It is proposed that survival factors are also involved in regulating apoptosis of cells that deviate from the migratory pathway. PGCs that end up in a region of the embryo too far from secreted survival factors will be signaled for apoptosis (Edson et al., 2009). Factors involved in the survival of PGCs during migration include integrin beta-1 (ITGB1), 3-hydroxy-3-methylglutaryl-CoA reductase (HMGCR), DND1, and B-cell lymphoma 2 (BCL2)-associated protein X (BAX) (Richardson & Lehmann, 2010). ITGB1, HMGCR, and DND1 support survival of PGCs during migration, although are not critical to the process and were not included in the visual representation. BAX is an apoptosis regulator and also plays an important role in controlling the oocyte population later in early ovarian development (Benedict et al., 2000). On E10 (Fig. 2.5), the cessation of migration begins once the PGCs interact with somatic cells upon reaching the gonadal ridge.

### 2.5. The undifferentiated gonad and sex differentiation (E10 to E15)

During PGC migration, cells in the gonadal ridge express Wilms tumor protein homolog (WT1) (Fig. 2.5), which promotes the thickening, organization, and growth of the gonadal ridge (Chen, Jefferson, Newbold, Padilla-Banks, & Pepling, 2007). WT1 is additionally involved in PGC proliferation and female differentiation during this period (Wilhelm, Palmer, & Koopman, 2007). In males and females, empty spiracles homeobox 2 (EMX2) plays a role in development of gonads and other reproductive organs

(Miyamoto, Yoshida, Kuratani, Matsuo, & Aizawa, 1997). Another factor involved in gonad development is secreted during PGC migration, LIM/homeobox protein 9 (LHX9), which regulates somatic cell proliferation (Birk et al., 2000). EMX2 and LHX9 are not included since neither factor is directly involved in the development of viable oocytes. Upon colonizing the undifferentiated gonadal ridge, PGCs undergo a period of rapid mitosis, dividing to 3,000 cells by E12.5 (Lei & Spradling, 2013b). On E14.5 there are approximately 18,000 cells in the ovary and PGCs have developed to oogonia.

Shortly after the period of mitosis, differentiation factors begin to be promoted. The normal development of the undifferentiated gonad produces female reproductive organs, unless male-specific factors are upregulated; this critical juncture in the undifferentiated gonad is mediated by steroidogenic factor 1 (SF1) (Edson et al., 2009; Liu, Bingham, Parker, & Yao, 2009). Ovary formation occurs through uninhibited expression of female differentiation factors (R-spondin-1 (RSPO1), WNT4, β-catenin, and dosage sensitive sex reversal, adrenal hypoplasia critical region, on chromosome X, gene 1 (DAX1)), and the downregulation of cytochrome P450, family 11, member A1 (CYP11A1) (Fig. 2.5). RSPO1 plays an essential role in ovary formation by activating the WNT4/β-catenin signaling pathway on E11 (Chassot et al., 2008; Liu et al., 2009). Upregulation of WNT4/β-catenin inhibits production of CYP11A1 delaying steroidogenesis and promotes production of female differentiation factors, FOLLISTATIN and DAX1 (Mizusaki et al., 2003). DAX1 plays a role in steroidogenesis inhibition and activation of steroidogenesis stimulated by retinoic acid 8 (STRA8) (see Fig. 2.6) (Achermann et al., 2001; Anderson et al., 2008). Male-specific factors were omitted because our focus is upon ovarian

development. However, male sex differentiation would take place during this period with the expression of male-specific factors as described briefly below.

On E12 (Fig. 2.5), β-catenin controls follistatin signaling leading to the accumulation of retinoic acid through the downregulation of the retinoic acid metabolizing protein, CYP26B1 (Bowles et al., 2006). Follistatin binds to activin, regulating CYP26B1. CYP26B1 is a sex determination regulator involved in the degradation of retinoic acid. In males, CYP26B1 is upregulated which causes the breakdown of retinoic acid, suppressing *Stra8*-dependent meiotic pathway and a *Stra8*-independent mitotic pathway and promoting male germ cell differentiation (Saba, Wu, & Saga, 2014).

The build up of retinoic acid stimulates STRA8 to activate factors that promote meiosis of oogonia during early ovarian development. STRA8 (Fig. 2.6) first activates synaptonemal complex proteins 1, 2, and 3 (SYCP1, SYCP2, and SYCP3), which play a role in the formation of the synaptonemal complex (Kouznetsova, Benavente, Pastink, & Höög, 2011). During meiosis the synaptonemal complex organizes and pairs homologous chromosomes for genetic recombination. STRA8 also activates meiotic recombination protein SPO11, and DNA meiotic recombinase 1 (DMC1), which are involved in initiating homologous recombination through double-stranded DNA breaks and repairing double-stranded breaks, respectively (Baltus et al., 2006). Double-stranded DNA breaks are necessary for recombination during meiosis. Oogonia develop into oocytes prior to entering meiosis.

After the period of mitosis and sex determination, some oocytes undergo apoptosis. Death of oocytes begins on E14.5 (Fig. 2.6) and continues until the end of early ovarian development. The number of oocytes decreases to 13,000 oocytes on E18 and to about

8,000 on P2 (Lei & Spradling, 2013b). The intracellular apoptosis pathway is initiated through activation of the aryl hydrocarbon receptor (AHR) via a natural occurring AHR ligand. AHR activates BAX, causing BAX to bind with apoptosis regulator BCL2 allowing formation of an apoptosome in the cytosol of the oocyte (Benedict et al., 2000). Apoptosome formation activates caspase-9 (CASP9) leading to apoptosis (Wei et al., 2001). It is proposed that the apoptotic process is activated to eliminate abnormal or inferior cells that may not produce healthy, fertilizable eggs during the later phase of ovarian development.

### 2.6. Germ cell nest formation (E16 to E18)

During the period of oocyte apoptosis, oocytes form clusters called germ cell nests. Germ cell nests are interconnected oogonia formed by incomplete cytokinesis and surrounded by somatic cells, like granulosa cells (Haglund, Nezis, & Stenmark, 2011). Germ cell nest size and abundance, prior to birth, show no significant difference between cortex and medullar regions (Lei & Spradling, 2013b). The topic of germ cell nest formation is not well studied, thus signaling factors involved in formation and the purpose of nest formation is unknown (Fig. 2.7).

### 2.7. Germ cell nest breakdown and primordial follicle formation (E16 to P2)

Signaling factors involved in the breakdown of germ cell nests are expressed a few days prior to the actual breakdown of germ cell nests. On E16, the neurogenic locus

notch homolog protein 2 (NOTCH2) signaling pathway is activated in granulosa cells by surface protein jagged-1 (JAGGED1) binding to the NOTCH2 receptor and continues into early postnatal stages (Liang, Soyal, & Dean, 1997; Xu & Gridley, 2013). Activation of the NOTCH2 signaling pathway upregulates transcription factors hairy and enhancer of split-1 (HES1) and hairy/enhancer-of-split related with YRPW motif protein 2 (HEY2), which are necessary for germ cell nest breakdown and primordial follicle formation (Trombly, Woodruff, & Mayo, 2009). Factor in germline alpha (FIGLA), a transcription factor, is involved in the upregulation of zona pellucida sperm-binding protein 1 (ZP1), ZP2, and ZP3; proteins that are involved in recognition and binding of an oocyte to granulosa cells (Soyal, Amleh, & Dean, 2000).

The final stage of early ovarian development occurs two days after birth with the breakdown of germ cell nests and formation of primordial follicles (Fig. 2.8). For the majority of mouse strains, the embryonic period ends and mice are born at about E20-21 (P0); at this stage, germ cell nests are present in the developing ovary. Breakdown of the germ cell nests is initiated after birth and is associated with a decrease in estradiol concentrations from the removal of the placental connection (Chen et al., 2007). During the breakdown of germ cell nests, granulosa cells begin to invade and encircle a single oocyte, eventually forming a primordial follicle (Tingen, Kim, & Woodruff, 2009). Primordial follicles are morphologically distinguished as a single oocyte, larger in size than one in a germ cell nest, completely surrounded by a single layer of flattened, squamous shaped granulosa cells. Oocytes in primordial follicles have a larger cytoplasm to nucleus ratio compared with oocytes in germ cell nests (Griffin, Emery, Huang, Peterson, & Carrell, 2006). Primordial follicles formed during early ovarian development

make up the pool of potential fertilizable eggs at sexual maturity. Follicles remain quiescent until activated through folliculogenesis. Those activated prior to puberty will undergo atresia, death of ovarian follicles, during folliculogenesis, while those activated post-puberty may produce fertilizable eggs or also undergo atresia (Peters, 1969). As with germ cell nest formation, the mechanisms of germ cell nest breakdown, and primordial follicle formation in mice are also not fully understood.

### 2.8. Evidence for ovarian stem cells

In mammals, the abundance of potentially fertilizable germ cells was originally thought to be limited to the number of primordial follicles formed during early ovarian development, however studies have observed the presence of stem cells in the mouse ovary after P2. OSCs were discovered in the ovarian surface epithelium and presence of cells in the ovary was detected weeks to months after birth (Imudia et al., 2013; Johnson, Canning, Kaneko, Pru, & Tilly, 2004; Niikura, Niikura, & Tilly, 2009). Controversy remains whether or not the observed stem cells actively contribute to the germ cell pool. A recent study found germ cells in the ovary expressing factors related to the entry of meiosis and germ cell mitosis up to 4 months after birth (Guo et al., 2016). In contrast, cell-lineage tracing studies show no evidence for presence of putative germ stem cells in juvenile and adult mice (Lei & Spradling, 2013a; Zhang et al., 2014; Zhang et al., 2012). The presence of active germ stem cells producing viable germ cells would modify our understanding of the size of the female germ cell pool, the female reproductive lifespan, and select infertility issues. With respect to our review and visual representation, OSCs

may influence the size of the ovarian follicle population beyond P2. Our visual representation of early ovarian development would continue to reference the stages and timeline presented here, because this process is important for producing the founding population of primordial follicles in the ovary. Additional research is required to fully understand the elusive role of the mammalian OSC.

## 2.9. Conclusion

This review summarizes the molecular signaling and regulation associated with the current scientific understanding of early ovarian development in mice. It is the first visual representation, to our knowledge, that shows the known signaling networks vital to ovarian development, elucidating the pathways connected to specific processes. The figures show how different molecular events are involved in similar developmental activities. For example, PGC migration is influenced by both SDF1-CXCR4 and KIT ligand-receptor interactions, though the two chemoattractant interactions are not controlled by the same molecular signaling. In addition, this study visually highlights areas of ovarian development that lack data, such as germ cell nest formation and germ cell nest breakdown.

Applications of this review include serving as a foundation for cell-based computational model development, using it as an education resource for early ovarian development instruction, and predicting adverse reproductive outcomes due perturbations (e.g. exposure to reproductive toxins) at the molecular and cellular levels. Phenotypic abnormalities resulting from toxicant exposure can be linked to a molecular event(s) in

the visual representation, highlighting a potential biological target(s) of the compound. Information of the connection between phenotypic outcomes and biological targets can ultimately be used for a predictive computational model that simulates changes in morphology and cell counts based upon perturbations in molecular-level targets. While ovarian development is relatively well understood in mice, more research is needed to fill data gaps in our understanding of the ovarian developmental process.

# Chapter 3. Cell-based computational model of early ovarian development in mice

## 3.1. Introduction

In mammalian females, the ovary is crucial for reproduction, supporting the growth and maturation of viable eggs. Proper development of the ovary is necessary for normal ovarian function during reproductive maturity. Abnormal ovarian development may lead to adverse reproductive consequences, such as improper development of ovarian follicles, which could possibly result in female infertility (Sarraj & Drummond, 2012). In mammals, early ovarian development occurs predominantly during fetal life and plays a large role in the health and longevity of the female reproductive lifespan. Exposure to stressors (e.g. reproductive toxicants) during early ovarian development can produce adverse outcomes to ovarian function and reproduction. Predicting adverse outcomes to ovarian function associated with the toxicant-mediated molecular effect can be done by combining information from studies about distinct ovarian development processes. Putting the toxic effect into perspective of the physiology of the ovary can aid understanding of the negative reproductive effects caused by toxicant exposure. Computational models can be used as a theoretical framework to bring together studies on specific processes into a holistic view.

Early ovarian development, like many developmental processes, is composed of several molecular signaling pathways, which are highly dependent on expression of select proteins (Edson et al., 2009). A biologically based computational model can integrate information on key biological processes involved in early ovarian development, and

could be used to predict the effects of toxicant exposure on the ovary (Raies & Bajic, 2016). In order to construct a computational model to predict the adverse reproductive outcomes from toxicant exposure, there is a need to first develop a computational model of normal ovarian development.

Existing computational models for normal reproduction focus on various biological functions using a variety of model platforms. For example, Wallace and Kelsey (Wallace & Kelsey, 2010) developed a model predicting the ovarian follicle pool over a woman's lifespan. Iber and Geyter (Iber & Geyter, 2013) constructed a bovine model of the spatial-temporal growth of ovarian follicles and the associated hormonal signaling under normal conditions. In the bovine model, data on multiple processes involved in folliculogenesis were combined to create a holistic model. Reproductive toxicity models have a variety of uses from predicting toxicokinetics to predicting impacts a toxicant has on hormone concentration levels during reproductive maturity and production of eggs (Kozlovsky & Gefen, 2013; Li et al., 2011; Quignot & Bois, 2013; Watanabe et al., 2016). Combined models of normal reproduction and toxicokinetics can be used to predict adverse reproductive outcomes in an organism. Though many models of reproduction and related processes in mammals exist, there are no models of normal early ovarian development.

Modeling early ovarian development needs to be done at the cellular level because developmental processes occur at the cellular level (e.g. cellular proliferation, migration, formation of germ cell nests, and formation of primordial follicles), and cannot be simplified to a broader biological scale. For example, formation and breakdown of germ cell nests and formation of primordial follicles involve the interactions of individual

oocytes and granulosa cells. To best model these processes, CompuCell3D (CC3D) (M. H. Swat et al., 2012) software was selected to develop the model.

CC3D is based on a Cellular Potts Model (Merks & Glazier, 2005) that incorporates a Monte Carlo method to model stochastic single-cell behavior. Model domains are made up of pixels where cells are defined as a group of pixels. Specifications of cellular behaviors (e.g. mitotic rates, cellular adhesion) are defined by functions in the model. There are two types of functions defined in the model, Plugins and Steppables, which perform operations on pixels and cells, respectively (M. H. Swat et al., 2012). See Chapter 1 for more information about CC3D. CompuCell3D has been used to model various biological processes such as tumor growth and angiogenesis, but has not been applied to models of mammalian ovarian function or development. This model is the first cell-based computational model of early ovarian development in mice.

## 3.2. Materials and Methods

### *3.2.1. Initial setup of the model*

To simplify the model, it was separated into two Phases; Phase I represents embryonic day 5.5 (E5.5) to E12.5 and Phase II represents E12.5 to postnatal 2 (P2). Phase I models the origin and migration of PGCs to the gonadal ridge and Phase II models development of germ cells and tissues in the gonad. One day of development *in vivo* is simulated by 600 MCS, and is consistent for both phases. The simulation length was 4200 MCS (7 days) for Phase I, and 6000 MCS (10 days) for Phase II. Phase II is meant to be a continuation of early ovarian development from Phase I, not a separate

model. Simulations were run on a Mac Pro, with a Quad-Core processor and took about 20 minutes to run Phase I and 30 minutes to run Phase II.

The picture interchange file format (PIFF) used as the initial lattice for the model was constructed from whole mount images of a mouse embryo and an embryonic mouse ovary for Phase I (Fig. 3.1) and Phase II (Fig. 3.2), respectively. A whole-mount image of a mouse embryo on E7.5 stained with alkaline phosphatase was used for the spatial scaling of tissues and PGCs in the PIFF for Phase I (Ginsburg et al., 1990). The PIFF for Phase II was constructed from a whole mount image of an XX mouse gonad on E12.5 stained for follistatin (Manuylov, Smagulova, Leach, & Tevosian, 2008).

Cell Draw, a PIFF generation program within CC3D, was used to trace the whole mount images to map the tissues and cells that were included in the model. The simulation domain size in Phase I and Phase II was 320 x 320 pixels and all cells defined in the PIFF had an initial volume of 4-6 pixels. The model is two-dimensional, simulating what would be experimentally observed in a cross-section as opposed to the whole embryo or gonad. Only cell types vital to ovarian development in each phase were included in construction of the PIFF. Because the model was designed to represent a cross-section of the embryo or ovary, the abundance of PGCs and oocytes set in the model represent one-sixth of the total abundance reported in the literature. The abundance of PGCs in the initial layout of Phase II corresponded to the abundance of PGCs at the end of the simulation in Phase I. Germ cells and somatic cells within the ovary were placed randomly within the gonad. The different CC3D cell types included in Phase I and Phase II of the model are listed in Table 3.1.

### *3.2.2. Model functions and parameters*

A thorough literature review for experimental data on the abundance of cells, biological processes (e.g. chemotaxis, mitosis, apoptosis), morphology, and the developmental timeline was conducted to define parameter values and identify model evaluation data. In the case of unknown or controversial data reported in the literature, parameters were fitted and hypothesized mechanisms were used in the model to best simulate outcomes consistent with outcomes reported in the literature. Hypothesized mechanisms included: continued proliferation during PGC migration to the gonadal ridge; sequential KIT signaling in hindgut epithelial cells; SDF1 and KIT signaling as the main signals involved in PGC migration (see Chapter 2 for more information on SDF1 and KIT); and a change in cellular adhesion in oocytes and granulosa cells to produce primordial follicles associated with a decrease in the concentration of maternal estrogen. Sequential signaling in the model is the activation of signaling in a cell when the concentration of the signal detected by that cell is greater than zero. When experimental data were not available, fitted parameter values were selected based on values from other CC3D models and to produce outputs consistent with other available experimental data such as immunohistochemistry images, micrographs and cell abundances. Parameter values for contact energy, lambda chemotaxis, lambda volume, and secretion rates in the model were kept within range of the values defined in other CC3D studies (see Appendix A for more information about parameters in CC3D functions) (Boas & Merks, 2014; Kleinstreuer et al., 2013; Maciej H. Swat, Thomas, Shirinifard, Clendenon, & Glazier, 2015).

CC3D functions control cell size, cell abundance, chemotaxis, cellular adhesion, and secretion of compounds, monitor lattice information in the simulation, and store data. Functions require parameter values, which were set initially to CC3D preset values and then calibrated based on model results to best simulate experimental observations. Data on PGC and oocyte abundance were recorded every 10 MCS in Phase I and Phase II, respectively. Phase I and Phase II parameters were organized into biological categories and parameter values are reported in Table 3.2 and Table 3.3, respectively. Descriptions of CC3D pre-set functions with additional detail can be found in Appendix A. Functions described below and in Appendix A are listed by biological category.

### Volume Steppable

In both phases, the target volume was fitted to remain as close to the initial volume values without causing cells to exhibit abnormal behavior (e.g. fragmentation, death). After an initial increase in volume of all cell types in Phase I and Phase II, cell volumes were programmed to remain constant throughout the simulation. Lambda volume values and the growth rate for cells were fitted to the data with a constraint that they were in range of other CC3D models. See Appendix A, eqn. 1 for how lambda volume is used in the model.

### Initial Contact Energy Plugin

Contact energies were fitted based on values for target volume and based on observed tissue morphology (Table 3.4 and Table 3.5). In Phase II, contact energy values control the morphology of germ cell structures in the ovary (e.g. germ cell nests and primordial

follicles). See Appendix A, eqn. 2 and eqn. 3 for information how contact energy is used in the model and how it contributes to the effective energy, respectively.

Contact Steering Steppable

The Contact Steering Steppable was used to adjust the contact energy between cell types. In Phase I, the contact energy between PGCs was programmed to increase to 21.0 at 1800 MCS, representing the decrease in E-cadherin expression prior to PGC migration (Bendel-Stenzel et al., 2000; Di Carlo & De Felici, 2000). In Phase II, the contact energy between oocytes increases to 31.0 and contact energy between oocytes and granulosa cells decreases to 15.5 when the maternal estrogen field becomes undetectable (when concentration equals 0 μM). The maternal estrogen field concentration was programmed to go to zero at 4800 MCS, the equivalent time of birth (Lei, Jin, Mayo, & Woodruff, 2010).

Secretion Steppable

The Secretion Steppable was used to define the rate of secretion of SDF1 and KIT in Phase I and maternal estrogen in Phase II. No experimental data for the secretion rate of these chemicals was found, so rates were fitted to be within range of secretion rates used for other CC3D models. In Phase I, the Secretion Steppable is called after 1500 MCS, which is equivalent to the time period in experimental data when migration signals begin being expressed. The constant secretion rate of SDF1 (2.0 μM/MCS) was set to be greater than the constant secretion rate of KIT (0.5 μM/MCS). When SDF1 secretion was greater than KIT secretion, PGCs would exhibit a normal pattern of migration to the

gonadal ridge. If KIT secretion was greater than SDF1, PGCs in the model would exhibit abnormal migration (i.e. PGCs would adhere to the hindgut instead of migrating to the gonadal ridge). In Phase II, secretion of maternal estrogen is present until 4800 MCS, the equivalent time period when birth occurs.

### Chemotaxis Plugin

The Chemotaxis Plugin is only defined in Phase I and controls the response of PGCs to the SDF1 and KIT chemical fields during PGC migration to the gonadal ridge. Parameter values for lambda chemotaxis were fitted since no measured data exists. The lambda chemotaxis value for the SDF1 field was set at a greater value than the lambda chemotaxis for the KIT field at 30 and 10, respectively.

### Diffusion Solver Steppable

In both phases, diffusion and decay rates were fitted to be within range of values from other CC3D models. The diffusion rate constant of SDF1 was fitted at a higher value to allow a concentration great enough to reach the PGCs in the posterior region of the embryo. The decay rate of KIT was greater than the decay rate of SDF1, to allow the SDF1 field to reach the posterior region of the embryo.

### Mitosis Steppable

The Mitosis Steppable defines the rate of mitosis for PGCs in Phase I and all cell types in Phase II. Mitotic rates of PGCs and oocytes were derived from data in the literature (De Sousa Lopes et al., 2007; Lei & Spradling, 2013b); mitotic rates of other

cell types in Phase II were set to be within range of other CC3D models. Of cell types programmed to undergo mitosis, cells were selected randomly to undergo mitosis. For Phase I, two theories exist about PGC proliferation during migration: 1) PGCs continue to undergo mitosis during migration and 2) PGCs halt mitosis during migration (K. A. Molyneaux et al., 2003; Runyan et al., 2006; Sekl et al., 2007). The model assumes the continued proliferation of PGCs during migration at the same mitotic rate as observed prior to migration. PGCs that undergo mitosis are selected at random and could be in the posterior region of the embryo, in the migration process, and at the location of the gonadal ridge. In Phase II, oocytes undergo mitosis from 0-1200 MCS during a rapid proliferation period. PGCs and oocytes are required to have at least twice the initial volume before undergoing division.

### Cell Death Steppable

In Phase I, the Cell Death Steppable is used to represent cell death that occurs during migration when PGCs do not receive enough survival signals. PGCs are programmed have a target volume of zero if they are in a location where the concentration of SDF1 is below 400 μM. The concentration was fitted to the boundaries around the gonadal ridge, so PGCs outside the gonadal ridge underwent apoptosis. In Phase II from 1200-6000 MCS, 0.008% of oocytes randomly selected and oocytes not in a cluster of other oocytes were selected per MCS to have a target volume of zero, representing the onset of apoptosis on E14.5. The percentage of oocytes to be randomly selected was defined from experimental data in the literature (Lei & Spradling, 2013b). To keep the model simple, the death of other cell types is not defined.

### Cell Activation Steppable

The Cell Activation Steppable, a non-preset Steppable written by H. Wear and Annika Eriksson, PhD Candidate, is a Steppable in Phase I that activates KIT signaling. This function activates KIT signaling through a change in the model cell type, from a non-secreting to a secreting hindgut epithelial cell. When the first two cells, which are initially defined as secreting hindgut epithelial cell types, start secreting KIT, as described in the Secretion Steppable, non-secreting hindgut epithelial cells that detect a concentration of KIT greater than 0.5 μM are programmed to change into a secreting hindgut epithelial cell. This creates a sequential expression of KIT in the secreting hindgut epithelial cells.

### Cell Abundance Tracking Steppable

Cell Abundance Tracking, a non-preset Steppable written by H. Wear and Annika Eriksson, PhD Candidate, is designed to keep track of and record the abundance of PGCs in Phase I and the abundance of oocytes in Phase II. It was used to record cell counts in the model to be compared with experimental data. For 25 full simulation runs in Phase I and Phase II, the function recorded the number of PGCs every 10 MCS to an external file. Data were combined to assess PGC abundance on a temporal scale.

### Model Code

See Appendix B for the code used for the model of early ovarian development in mice.

### *3.2.3. Sensitivity analysis*

A univariate analysis was performed to evaluate the influence individual variables have on the model outputs. More information on the sensitivity analysis including methods and results can be found in Chapter 4.

## 3.3. Results

### *3.3.1. Phase I*

Phase I of the model simulates processes that occur from E5.5 to E12.5: PGC origin, proliferation, and migration to the gonadal ridge (Fig. 3.3). PGCs remain in the posterior region of the embryo and undergo proliferation prior to migration. The model assumes SDF1 and KIT as the main chemoattractants during PGC migration. When chemoattractant signals activate, PGCs respond by moving to the gonadal ridge in a line comparable to what is observed in experimental images. Figures 3.4A and 3.5B show simulation outputs of PGCs during migration to the gonadal ridge, which follow a parade-like structure similar to experimental images (Figs. 3.4B and 3.5B) (Francis & Lo, 2006; Yeom et al., 1996).

In Phase I, the model incorporates the hypothesis of continued proliferation during migration. Experimental images (Fig. 3.5B) and reports in the literature (K. A. Molyneaux et al., 2003; Runyan et al., 2006) describe an increase in the number of PGCs, indicating PGCs continue to undergo mitosis while migrating. Incorporating continued proliferation results in PGC abundances more similar to experimental data (Fig. 3.6).

Experimental data falls within one standard deviation of 25 model simulation runs. Without continued mitosis, a lower number of PGCs reach the gonadal ridge. Following the hypothesis that PGCs continue to proliferate during migration produces model results that better align with data in the literature.

In the model, KIT signaling is hypothesized to be sequential. PGC abundance results when integrating sequential signaling, versus static signaling from hindgut epithelial cells, are more consistent with experimental data; fewer PGCs migrate to the gonadal ridge when KIT signaling is static, than when signaling is sequential. Under static signaling conditions in the model, the majority of PGCs appear adhered to the hindgut and few PGCs are observed migrating to the gonadal ridge. Sequential KIT signaling was incorporated in the model because results better aligned with experimental observations.

### *3.3.2. Phase II*

Phase II of the model simulated development of the ovary from E12.5 to P2: once PGCs reach the gonadal ridge, germ cell proliferation, germ cell nest formation and breakdown, and formation of primordial follicles (Fig. 3.7). Simulation outputs exhibited similar morphology to experixmental images. At the start of Phase II, the gonad appears in a long oval shape with germ cells scattered throughout the gonad and a relatively large volume of mesonephros tissue (embryonic tissue that facilitates nutrient supply to the developing gonad) present, similar to experimental images (Fig. 3.8). At 1800 MCS (E15.5), the number of oocytes in the gonad has increased and the gonad has a greater size due to continued mitosis of all cell types in Phase II. Experimental data show an increase in the number of oocytes dispersed randomly throughout the ovary (Fig. 3.9). At

this stage, apoptosis is initiated and germ cell nests begin to form. In Fig. 3.9 and Fig. 3.10, simulation outputs show oocytes in clusters similar to the germ cell nests observed in experimental images. In Phase II, proliferation of all cell types in the ovary has caused the shape of the ovary to become a more rounded. Simulation outputs in Phase II from 0-4800 MCS show similar morphologies to experimental images of the developing mouse ovary.

Phase II integrated one hypothesized mechanism that germ cell nest breakdown and primordial follicle formation is governed by a change in cell adhesion (change in contact energies in the model) associated with a loss of maternal estrogen. At 4800 MCS, the contact energies increase between oocytes and decrease between oocytes and granulosa cells, due to a decrease of maternal estrogen programmed in the model, causing the separation of oocytes and formation of primordial follicles. From 4800-6000 MCS, the majority of oocytes in the model become surrounded by granulosa cells and resemble primordial follicle formation as seen in experimental images (Fig. 3.11). The model however, does not simulate the squamous shape of granulosa cells in primordial follicles or the localization of primordial follicles to the cortex of the ovary as described in the literature. Additional information about the mechanisms controlling these processes is needed for future model refinement.

Oocyte abundance in Phase II follows the same pattern of increase, from 0-1200 MCS (E12.5-E14.5), and decrease, from 1200-6000 MCS (E14.5-P2), as observed in experimental data (Fig. 3.12) (Lei & Spradling, 2013b). The period of oocyte proliferation, exhibits exponential growth, consistent with the pattern of increased abundance due to mitosis. Oocyte decrease during the apoptotic period is linear. Models

results for oocyte abundance in Phase II closely resemble total germ cell count data in Fig. 4F from Lei and Spradling (Lei & Spradling).

### 3.4. Discussion

The cell-based model of early ovarian development in mice simulates the appearance of PGCs, migration to the gonadal ridge, germ cell proliferation in the gonad, formation and breakdown of germ cell nests, and formation of primordial follicles. Parameters were defined from data in the literature or fitted when data were absent. Keeping the values within range of other CC3D models increases the likelihood that values are biologically plausible. For instance, decreasing the cell target volume caused fragmentation and distortion of cells. Values were then further adjusted to produce simulation outputs with similar morphology to experimental images. For example, to best fit observed tissue structures, in Phase I, contact energies between PGCs and epithelial and hindgut cells had to be lower than contact energies between extracellular matrix and epithelial and hindgut cell. The contact energy values are involved in defining the location of cell types within the model. The model also assumed continued PGC mitosis during migration in Phase I. PGC abundances without continued mitosis results in a lower abundance of PGCs reaching the gonadal ridge. When PGC migration is assumed to be governed by one signal (e.g. only SDF1 is present in the model), fewer PGCs migrate to the gonadal ridge, resulting in a lower abundance of PGCs reaching the gonadal ridge than what has been reported in the literature (Lei & Spradling, 2013b). In addition, the pathway of PGC migration to the gonadal ridge with only SDF1 signaling present is inconsistent with

experimental observations; PGCs do not migrate along the hindgut, but migrate through embryonic tissue. PGCs do not migrate to the gonadal ridge when the lambda chemotaxis value for KIT was about equal to or greater than the chemotaxis value for SDF1.

In Phase II, the contact energy values for granulosa cells and oocytes were altered to produce germ cell nests and primordial follicles. Alternate fitted values producing similar outputs to the model may exist, however it was outside the scope of this study to assess all combinations of fitted parameter values to produce the same results.

The model can be used as an interdisciplinary tool, with one application being the ability to make hypotheses about mechanisms of development. The model tested four hypotheses about early ovarian development in mice due to absent or conflicting data (see section 3.2 Methods for details on hypothesized mechanisms incorporated to the model). Hypotheses that produced results with a higher resemblance to experimental observations were chosen to be integrated in the model.

Studies have debated whether or not PGCs undergo mitosis during migration to the gonadal ridge (K. A. Molyneaux et al., 2003; Runyan et al., 2006; Sekl et al., 2007). Our model requires continuous proliferation during migration to best fit the experimental data. This hypothesis produces cell abundance results in Phase I that align better with experimental results on PGC abundance once PGCs migrate to the gonadal ridge. Halting mitosis during PGC migration resulted in a lower abundance of PGCs reaching the gonadal ridge than what is reported in the literature. Experimental images tracing PGC migration also show an increase in the number of PGCs, in a linear formation, migrating along the hindgut through an increased expression of Oct-4 during the migration period (Francis & Lo, 2006).

Mechanisms of signaling for germ cell migration in mice is not well understood. Our model hypothesizes expression of SDF1 from the gonadal ridge to be static and the expression of KIT from hindgut epithelial cells to be sequential starting with hindgut epithelial cells closest to the posterior region of the embryo moving towards the gonadal ridge. Programming sequential signaling in the model resulted in individual PGCs moving towards the gonadal ridge in a line formation comparable to experimental images and abundances of PGCs migrating to the gonadal ridge consistent with the literature (Francis & Lo, 2006; Yeom et al., 1996). Modeling KIT as a static signal secreted from the hindgut epithelium resulted in the migration of only part of the PGC population to the gonadal ridge, while the non-migrating population remained proximate to the hindgut in the posterior region of the embryo. Thus, our model assumes sequential KIT signaling.

Mechanisms governing germ cell nest formation, nest breakdown, and primordial follicle formation in mice are not well-understood. Studies have shown primordial follicles to be located within the cortex region of the ovary (Zheng et al., 2014), while earlier in development, germ cell nests are dispersed throughout the ovary (Lei & Spradling, 2013b). It is unknown what mechanisms cause this localization, however one observation suggests the localization is due to proliferation of granulosa cells in the center of the ovary, pushing the primordial follicles to the cortex (Hennebold 2016, personal communication). Additional data is needed so to simulate the distribution of primordial follicles isolated only to the cortex

The cell-based computational model of early ovarian development in mice was constructed using the most up-to-date information in the literature. Hypotheses and predictions about the mechanisms controlling PGC migration and primordial follicle

formation were made during development of the model. In addition, the model can be applied to making predictions about the outcomes from reproductive toxicity. Parameters in the model can be altered according to the molecular effects from toxicant exposure and prediction about ovarian development can be made using the model. Adverse reproductive outcome predictions have yet to be made with our model. Lastly, the model can serve as an educational learning tool to better understand ovarian development. The model contains the potential to be refined for more specific applications and can be extended to simulate proceeding phases of ovarian development.

# Chapter 4. Sensitivity Analysis for the Computational Model of Early Ovarian Development in Mice

## 4.1. Introduction

Model parameters in Phase I and Phase II were defined from data in the literature or fitted to produce outcomes similar to what has been observed during early ovarian development. Data on cell volume, mitotic rate, and apoptotic rate were derived from primary studies, while parameter values for contact energy, lambda volumes, growth rate, secretion variables and chemotaxis were fitted. For additional details of the data and methods for setting the parameter values see Chapter 3. To analyze parameter uncertainties and identify which parameters have the highest control over the model behaviors, a sensitivity analysis was conducted.

Univariate sensitivity analysis is a method to evaluate the influence that individual variables have on the model outputs. In a univariate sensitivity analysis, each parameter is modified by a specified percentage of the original value, keeping all other parameters at their original values, and then endpoints are evaluated (Tu & Gilthorpe, 2008). Changes in model endpoints are unambiguously attributed to modifications made to the single variable, thus outcomes observed when modifying each parameter can be compared to one another to assess which variables have the greatest control over model behavior.

For Phase I and Phase II of the model selected parameters were modified ±10% one at a time. Four outcomes were evaluated: (i) PGC and oocyte abundance for Phase I and Phase II, respectively; (ii) cell structure integrity; (iii) developmental process accuracy;

and (iv) the number of incomplete trials. The number of incomplete trials was gathered from the number simulations that did not fully run when running 25 full simulations (i.e. there would be 5 incomplete simulations if it took 30 simulation runs to produce 25 full simulations). Parameter sensitivity was determined by ranking parameters according the results of the four endpoints listed above; Phase I and Phase II parameters were evaluated separately.

## 4.2. Methods

The following model parameters were analyzed for sensitivity. For Phase I of the ovarian development model, evaluated parameters were PGC growth rate ($g_{\tau 1}$), lambda SDF1 ($\lambda_{SDF1(\tau 1)}$), lambda KIT ($\lambda_{KIT(\tau 1)}$), lambda volume ($\lambda_{V\tau}$), cell target volumes ($V_\tau$), secretion rate of sdf1($\Theta_{SDF1}$), secretion rate of KIT ($\Theta_{\mathrm{KIT}}$), diffusion rate of SDF1($D_{SDF1}$), diffusion rate of KIT ($D_{KIT}$), decay rate of SDF1 ($k_{SDF1}$), decay rate of KIT ($k_{KIT}$), mitotic rate of PGCs ($m_{\tau 1}$), and contact energy ($J_{\tau\text{-}\tau}$) (see Table 3.2 and 3.4 for full parameter definitions). Parameters evaluated in Phase II were contact energies ($J_{\tau'\text{-}\tau'}$), cell death rate ($d_{\tau'}$), lambda death rate ($\lambda_{d\tau}$), lambda volume ($\lambda_{V\tau'}$), mitotic rate of all Phase II cell types ($m_{\tau'}$), and cell target volumes ($V_{\tau'}$) (see Table 3.3 and 3.5 for full parameter definitions). The contact energy parameters (i.e. $J_{\tau\text{-}\tau}$ and $J_{\tau'\text{-}\tau'}$) represent contact energies between all cell types in the model. For each parameter undergoing sensitivity analysis, 25 full simulations were run for a 10% increase to the original value and 25 full simulations for a 10% decrease. That is, changes in some parameter values resulted in incomplete simulations, and required additional simulations until results from 25 full simulations

were obtained. Cell structure integrity and accuracy of developmental processes were evaluated through visual comparison. The abundance of PGCs in Phase I and oocytes in Phase II were compared with cell abundances reported in the literature.

### *4.2.1. Cell structure and accuracy of developmental processes*

Cell structure integrity and accuracy of developmental processes were analyzed visually by comparing screenshots and videos of the simulations with immunohistochemistry fluorescent images and histologic images. Screenshots of the simulation domain were taken every 150 Monte Carlos steps (MCS) in both Phase I and Phase II, and videos were recorded for a subset of simulations. Experimental images (Fig. 3.4, 3.5, 3.9, 3.10, and 3.11), used to verify the model in Chapter 3, were also used for the sensitivity analysis. In addition to experimental images, morphological descriptions in the literature were used to develop the model and assess parameter sensitivity, especially for periods of development with limited image data (Edson et al., 2009; Ginsburg et al., 1990; Lei & Spradling, 2013b; K. Molyneaux & Wylie, 2004; Sarraj & Drummond, 2012). Assessment of sensitivity for the accuracy of developmental processes compared the morphology observed in experimental images (3.4, 3.5, 3.9, 3.10, and 3.11). Parameters were considered sensitive if the developmental stages occurred on a different timeline than reported in the literature, morphology was altered, or if a developmental stage did not occur. Alterations to the normal cell size was also analyzed when assessing developmental process accuracy. Parameters were ranked based on the occurrence of applicable sensitivity issues—parameters were then categorized as sensitive or not sensitive for developmental process accuracy.

Assessment of cell structure integrity was based on the shape of the cell surface. A normal cell appears as an oval-shape with little to no fragmentation. A cell with a jagged surface and/or signs of fragmentation would be considered irregular and biologically inaccurate. See Fig. 4.1 for examples of distinguishing between regular and irregular shaped cells. In addition, images from Chapter 3 (Fig. 3.4, 3.5, 3.9, 3.10, and 3.11), used to evaluate the accuracy of developmental processes, were also used to assess cell size of PGCs and oocytes. Parameters were ranked as sensitive or not sensitive for cell structure sensitivity.

### *4.2.2. Cell abundance*

Cell abundance was also used to assess the sensitivity of adjusted parameters in Phase I and Phase II. Abundance of PGCs and oocytes in Phase 1 and Phase 2, respectively, was recorded every 10 MCS during the entire simulation length for 25 simulations. The average of 25 simulations ran under normal conditions ± one standard deviation was considered the "normal range" for cell abundance. For each tested parameter, cell abundances were compared with the normal range; the number of simulations with cell abundances outside the normal range were recorded for sensitivity evaluation. The number of simulations that were unable to run the full length, due to death of germ cells, were also recorded. A parameter with a greater number of trials outside of the normal abundance range or more incomplete simulations was categorized with higher sensitivity.

For Phase I and Phase II, parameters showing the highest sensitivity (in the top one-third) in at least three of the four endpoint categories were ranked as highly sensitive.

Parameters with the highest sensitivity for one to two of the endpoints were categorized as having medium sensitivity in the model, and parameters without sensitivity for an endpoint were considered low sensitivity.

## 4.3. Results

### *4.3.1. Phase I: Cell structure integrity and developmental process accuracy*

Comparison between the model and real images on E5-E8 were limited due to lack of image data during this developmental period. Evaluation of PGC migration and entrance into the gonadal ridge, E8-E12, utilized images found in the literature. $J_{\tau\text{-}\tau}$, $m_{\tau 1}$, $\lambda_{KIT(\tau 1)}$, $\lambda_{SDF1(\tau 1)}$, $D_{KIT}$, $D_{SDF1}$, and $\Theta_{SDF1}$ had the greatest influence on the model visual endpoints and were sensitive for both developmental process accuracy and cell structure integrity (Table 4.1). Cell structure and developmental process endpoints for each parameter tested are described in sections 4.3.1a to 4.3.1i.

#### 4.3.1a. Contact energy ($J_{\tau\text{-}\tau}$)

Adjustments to $J_{\tau\text{-}\tau}$ affected both cell structure and developmental processes (Table 4.1). A decrease in $J_{\tau\text{-}\tau}$ results in increased fragmentation and lower stability of cells. PGC migration is also abnormal with a reduction in $J_{\tau\text{-}\tau}$, resulting in disjointed clumps of PGCs moving along the hindgut. A 10% increase in $J_{\tau\text{-}\tau}$ causes cells to be less motile, disrupting the timeline of developmental processes. PGC migration occurred slower than reported in the literature and the number of PGCs that migrated into the gonadal ridge decreased, suggesting the modified $J_{\tau\text{-}\tau}$ produced simulation outputs showing abnormal

PGC migration. The $J_{\tau\text{-}\tau}$ ranks high for sensitivity (Table 4.2). See Fig. 4.2 for PGC abundance results.

4.3.1b. Rate of Mitosis

A reduced rate of mitosis causes developmental processes to occur on a slower timeline than normal conditions and times reported in the literature. PGC migration appears slower and fewer PGCs make it to the gonadal ridge. Increasing the $m_{\tau 1}$ produces smaller cells compared to normal conditions and cells appear more clustered. Adjusting the rate of mitosis ±10% had no visible effects on the integrity of cellular structure. $m_{\tau 1}$ was sensitive for both developmental process accuracy and cell structure (Table 4.1) and had high sensitivity overall (Table 4.2). See Fig. 4.3 for PGC abundance results.

4.3.1c. Lambda value for chemotaxis to SDF1 field ($\lambda_{SDF1(\tau 1)}$)

There was no noticeable effect to cell structure when $\lambda_{SDF1(\tau 1)}$ was reduced. PGCs appear to adhere to the hindgut more, instead of migrating to the gonadal ridge, thus fewer PGCs move to the gonadal ridge under conditions with a lower $\lambda_{SDF1(\tau 1)}$. Increasing the $\lambda_{SDF1(\tau 1)}$ results in a higher frequency of cellular fragmentation and irregularity of the cell structure. A higher number of PGCs develop a more abnormal structure as they approach the gonadal ridge. An increased $\lambda_{SDF1(\tau 1)}$ produced a non-realistic migration process, causing PGCs to break off into fragments as they were migrating to the gonadal ridge. For PGC abundance results, see Fig. 4.4. This parameter has high sensitivity, and is one of the most sensitive parameters in Phase I (Table 4.1).

4.3.1d. Lambda value for chemotaxis to KIT field ($\lambda_{KIT(\tau 1)}$)

Decreasing $\lambda_{KIT(\tau 1)}$ did not affect the integrity of the cell structure, however it reduced the accuracy of PGC migration. A reduced $\lambda_{KIT(\tau 1)}$ caused PGCs to move further from the hindgut into the embryonic tissue beyond what has been shown in images from the literature. An increased $\lambda_{KIT(\tau 1)}$ causes PGCs to show high affinity for the hindgut resulting in abnormal cell structure with cells closest to the hindgut fragmenting and disintegrating. The abnormal cell structure and behavior leads to a slower migration and fewer PGCs moving into gonadal ridge. See Fig. 4.5 for PGC abundance results.

4.3.1e. Diffusion of SDF1($D_{SDF1}$)

Under conditions with a decreased $D_{SDF1}$, fewer PGCs migrate to the gonadal ridge, and migration occurs at a slower rate compared with normal conditions. Cell structure is not impacted with decrease in $D_{SDF1}$. However, an increase results in decreased cell structure and stability. A higher rate of $D_{SDF1}$ does not show any differences in developmental processes. $D_{\mathrm{SDF1}}$ has medium sensitivity. Results for PGC abundances can be seen in Fig. 4.6.

4.3.1f. Diffusion of KIT ($D_{KIT}$)

No visible changes in the integrity of the cell structure occurred with 10% decrease in $D_{KIT}$. PGCs did however, display slower migration to the gonadal ridge, with fewer PGCs migrating into the gonadal ridge. No visible changes in developmental process accuracy occurred with a 10% increase in $D_{KIT}$. However, an increased $D_{KIT}$ caused higher cell

fragmentation and instability. $D_{KIT}$ has medium sensitivity (Table 4.2). For PGC abundance results, see Fig. 4.7.

4.3.1g. Growth rate of PGCs ($g_{\tau 1}$)

A decreased $g_{\tau 1}$ shows no visible changes in developmental process accuracy or cell structure integrity. An increased $g_{\tau 1}$ results in an increased volume for PGCs relative to normal conditions and images from the literature. There were no visible changes in cell structure integrity, resulting in $g_{\tau 1}$ as having medium sensitivity (Table 4.2). PGC abundance results can be seen in Fig. 4.8.

4.3.1h. Secretion of SDF1 ($\Theta_{SDF1}$)

Reducing $\Theta_{SDF1}$ does not cause any cell structure abnormalities, however it does cause reduced PGC migration into the gonadal ridge. Migration occurs more slowly than under normal conditions and fewer PGCs reach the gonadal ridge. Increasing $\Theta_{SDF1}$ results in larger PGCs that become more fragmented as they approach the gonadal ridge. Cellular behavior during migration shows small, clumped groups of PGCs migrating, which is inconsistent with cell behavior during migration reported in the literature. This parameter had medium sensitivity (Table 4.2). Fig. 4.9 shows results for PGC abundance for $\Theta_{SDF1}$ adjusted ±10%.

4.3.1i. Secretion rate of KIT ($\Theta_{KIT}$), target volume ($V_\tau$), lambda volume ($\lambda_{V\tau}$), decay of SDF1 ($k_{SDF1}$), and decay of KIT ($k_{KIT}$)

No visible changes in developmental process accuracy or cell structure integrity occurred with a ±10% change to $\Theta_{KIT}$ (see Fig. 4.10 for PGC abundance results), $V_\tau$ (see Fig. 4.11 for PGC abundance results), $\lambda_{V\tau}$ (see Fig. 4.12 for PGC abundance results), $k_{SDF1}$ (see Fig. 4.13 for PGC abundance results), or $k_{KIT}$ (see Fig. 4.14 for PGC abundance results). These parameters were not sensitive for developmental process accuracy or cell structure; thus parameters were categorized as having low sensitivity (Table 4.2).

### *4.3.2. Phase I: PGC Abundances*

Cell abundances for each simulation in Phase I followed the same pattern, steadily increasing from 0-3600 MCS, then slightly decreasing until the end of the simulation at 4200 MCS (see PGC abundance figures). The majority of simulations for each adjusted parameter analyzed were within the normal range (Table 4.3). $\lambda_{V\tau}$, $V_\tau$, and $\Theta_{SDF1}$ had the most simulations outside of the normal range, while $\lambda_{KIT(\tau1)}$, $k_{KIT}$, and $J_{\tau\text{-}\tau}$ had the highest number of incomplete trials. No correlations were found between the number of simulations outside the normal range and the number of incomplete simulations in Phase I.

### *4.3.3. Phase II: Cell structure integrity and developmental process accuracy*

Cell structure integrity was normal for all parameters in Phase II of the model, except for $d_{\tau'}$ (Table 4.4). Sensitivity analysis of developmental process accuracy mainly assessed the formation of important morphological structures: germ cell nest formation,

nest breakdown, and primordial follicle formation; real images were the principle tool for evaluating morphology. $d_{\tau'}$ had the highest control over visual endpoints in Phase II, followed by $J_{\tau'\text{-}\tau'}$. Analysis of cell structure integrity and developmental process accuracy are described in more detail for each tested parameter in Phase II (sections 4.3.3a to 4.3.3c).

4.3.3a. Rate of Death ($d_{\tau'}$)

A change in $d_{\tau'}$ for oocytes causes distorted cell structure and morphology, resulting in inaccurate developmental processes. Germ cell nests do not properly form; a decrease in $d_{\tau'}$ causes large clusters of oocytes to form, larger than germ cell nests reported in the literature, and an increase causes single isolated PGCs. Increasing $d_{\tau'}$ also causes a higher frequency of cellular fragmentation and reduced cell structure. For oocyte abundance results see Fig. 4.15. $d_{\tau'}$ was sensitive for developmental process accuracy and cell structure (Table 4.4), thus had high sensitivity (Table 4.2).

4.3.3b. Contact energy ($J_{\tau'\text{-}\tau'}$)

There were no visible changes to cell structure integrity with a ±10% change in $J_{\tau'\text{-}\tau'}$. An increase or decrease in $J_{\tau'\text{-}\tau'}$ caused disruption of developmental processes through altered morphology. Crucial developmental structures, germ cell nests and primordial follicles, appeared distorted when compared to images for primary studies. This parameter was sensitive for developmental process accuracy but not cell structure (Table 4.4), thus the parameter was categorized as having medium sensitivity (Table 4.2). See Fig. 4.16 for oocyte abundance results.

4.3.3c. Lambda death rate ($\lambda_{d\tau'}$) and rate of mitosis ($m\tau'$) lambda volume ($\lambda_{V\tau'}$), and target volume ($V_{\tau'}$),

No visible changes in developmental process accuracy or cell structure integrity occurred with a ±10% change to $\lambda_{d\tau'}$ (see Fig. 4.17 for PGC abundance results) or $m\tau'$ (see Fig. 4.18 for PGC abundance results), $\lambda_{V\tau'}$ (see Fig. 4.19 for PGC abundance results) or $V_{\tau'}$ (see Fig. 4.20 for PGC abundance results). These parameters all have low sensitivity (Table 4.2).

### *4.3.4. Phase II: Oocyte abundance*

Simulations for each parameter tested in Phase II showed a rapid proliferation of oocytes from 0-1200 MCS and a steady, linear decrease from 1200-6000 MCS (see cell abundance figures). There were no incomplete simulations for any of the parameters assessed in Phase II. All parameters, except for $V_{\tau'}$, had at least one simulation within the normal range for oocyte abundance, however Phase II parameters showed an increase in the number of simulations outside the normal range when compared to Phase I parameters (Table 4.5). Oocyte abundance was greatly affected by manipulations to $V_{\tau'}$ and $m\tau'$, resulting in an increase in abundance, relative to the normal range, with a 10% increase in the parameter value and a decrease in abundance with a 10% decrease to the value. No correlations were observed between oocyte abundance and visual endpoints in Phase II.

### *4.3.5. Ranking sensitivity of parameters*

Parameters were categorized into high, medium, and low sensitivity based on the combined results at all endpoints (Table 4.2). There were no incomplete simulations for any of the parameters tested in Phase II, so only three endpoints were analyzed. Rankings in Phase II categorized high as the highest sensitivity for at least two endpoints, medium for one endpoint, and low for no endpoints. In Phase I, $J_{\tau\text{-}}$, $m_{\tau 1}$, $\lambda_{KIT}$, and $D_{SDF1}$ had high sensitivity and in Phase II, $d_{\tau 1}$, had high sensitivity to the model behavior.

## 4.4. Discussion

Sensitivity of parameters in Phase I and Phase II were evaluated by four endpoints: cell structure integrity, developmental process accuracy, germ cell abundance, and number of incomplete trials (for Phase I). In both Phases, there was no correlation between all endpoints assessed and parameter sensitivity ranking (e.g. the most sensitive parameter in regard to PGC abundance was different from the most sensitive parameter for cell structure integrity). Parameters were categorized according to their sensitivity in all endpoints evaluated, representing the influence a parameter has on specific endpoints and the overall control that a parameter has in the model behavior.

In Phase II the number of incomplete simulations was not used to evaluate parameter sensitivity because no incomplete simulations occurred. Incomplete simulations were the result of all germ cells in the model dying, causing a premature ending or incomplete simulation. Phase I started with fewer germ cells (one PGC) at the start of the simulation, compared to Phase II (150 oogonia). The difference in starting abundance of germ cells

combined with a variation in the functions influencing model behavior in Phase I compared to Phase II explains the dissimilarity in incomplete simulations between the Phases.

The majority of parameters causing abnormal cell structure integrity, including parameters with high sensitivity, also presented abnormal developmental process accuracy, which may indicate that there is a relationship between the two endpoints. For example, altering $d_{\tau'}$ ±10% in Phase II, caused fragmentation of oocytes, which led to abnormal formation of germ cell nests. Sensitivity analysis results indicate that irregular cell structure will lead to a disruption in the developmental process, although it is not necessary to produce an abnormal developmental process outcome (e.g. $\lambda_{KIT(\tau 1)}$ in Phase I and $J_{\tau'\text{-}\tau'}$ in Phase II). A greater percentage of parameters in Phase I showed developmental process and cell structure sensitivity, likely due to the number of parameters defined in Phase I compared to Phase II. To keep the model representative of the existing data, early ovarian development processes were modeled parsimoniously, relying on the fewest number of parameters (i.e. $J_{\tau\text{-}\tau'}$) to control the morphological changes observed.

Germ cell abundances in Phase II showed high sensitivity for the $V_{\tau'}$ and $m_{\tau'}$. $m_{\tau'}$ directly controls the abundance of cells, explaining its sensitivity. $V_{\tau'}$, when reduced, may not be a large enough volume for cells to undergo mitosis and when increased, may not have enough physical space within the tissue to undergo division. $V_{\tau}$ was also identified as a sensitive parameter in Phase I, with respect to cell abundance. Interestingly, $m_{\tau'}$ did not have high sensitivity and $\lambda_{V\tau}$ was the most sensitive. In Phase I parameters relating to volume have greater control over PGC abundance than a parameter directly controlling

cell proliferation. This observation may be explained by a relationship between multiple parameters, however it cannot be determined from the results of the univariate analysis.

The univariate sensitivity analysis allows for definitive evaluation of the impact that parameters in Phase I and Phase II had on the model behavior. This method was useful for the assessment of parameter influence in the model and the level of sensitivity for each parameter. A univariate sensitivity analysis, however does not analyze how interactions between multiple parameters may affect model behavior, assuming relationships between parameters exist. Evaluating the multivariate relationships was outside the scope of the sensitivity analysis method used for the model, as the original goal was to identify which parameters were most sensitive in the model.

The sensitivity analysis played an important role in model development. Identifying which parameters have high sensitivity helps with calibration of parameters, reduces uncertainty, and assists with simplification of the model. Results from this analysis can be used to focus future research on the parameters with high sensitivity (e.g. collecting in vivo data for a specific parameter, focus research on stressors that affect a parameter with high sensitivity). The sensitivity analysis also increases the understanding of parameter influence to the model behavior, allowing it to be a more compelling tool for assessing hypotheses and predicting adverse outcomes.

# Chapter 5. Gathering data and preliminary development for a cell-based model of folliculogenesis in monkeys

## 5.1. Introduction

Folliculogenesis is the process of ovarian follicle growth and maturation beginning with the activation of the primordial follicle and ending with the production of a pre-ovulatory follicle (Gosden & Lee, 2010; Richards & Pangas, 2010). It is an important process for reproduction, required for production of a mature, fertilizable egg. Folliculogenesis can be divided into two phases, the first encompassing the preantral growth, from primordial to preantral stage, and the second involving cyclical antral growth, from antral to pre-ovulatory stage (Dunlop & Anderson, 2014; Oktem & Urman, 2010). Preantral growth begins after the formation of primordial follicles, unlike antral growth which commences at puberty, and continues until the end of the female reproductive lifespan. Follicles activated prior to puberty undergo atresia (Kaipia & Hsueh, 1997). Growth and maturation of ovarian follicles during preantral growth occurs through intercellular and intracellular molecular signaling in oocytes and follicular cells. Disruption in the signaling processes may lead to improper or absent follicle development resulting in abnormal ovarian development (e.g. reduced follicle pool).

In humans, certain diseases of the ovary (e.g. primary ovarian insufficiency) can cause early loss of ovarian function, often resulting in infertility at a young age (Acton, 2012; Cannistra, 2004; Hamilton, 2012; Jose-Miller, Boyden, & Frey, 2007; Nelson, 2009). Due to fidelity in ovarian physiology, rhesus macaques (*Macaca mulatta*) are used as a model for human diseases of the ovary and related infertility issues (Brewer et al.,

2001; Marr-Belvin et al., 2010; Trounson, Gosden, & Eichenlaub-Ritter, 2013). For example, rhesus macaques have been studied as models for polycystic ovary syndrome and for methods of follicle preservation and maturation for certain cancer patients (Abbott et al., 2013; Shively & Clarkson, 2009; A. Y. Ting et al., 2013; Alison Y. Ting, Yeoman, Lawson, & Zelinski, 2011). Rhesus macaques play an important role in research of ovarian health, however studies in rhesus macaque can be expensive and time consuming. An approach to reduce the number of animals used experimentally is to use biologically based computational modeling.

A computational model of the preantral stages of folliculogenesis could be utilized as a tool for addressing questions and making predictions about factors that influence the follicle pool. A folliculogenesis model could also be used to develop and test hypotheses about the mechanisms involved in folliculogenesis or predict the adverse outcomes associated with disorders or exposure to stressors. Models are an efficient, cost effective, and humane tool that can be used as an alternative to certain animal experiments (e.g. rhesus macaques). To develop a computational model of the preantral stages of folliculogenesis in rhesus macaques, data about the morphological changes and biological mechanisms involved in follicle maturation and growth are required.

To determine what type of data are needed for model development, a modeling platform must be chosen. In previous work, we constructed a cell-based model of early ovarian development in mice using CompuCell3D (CC3D) software. CC3D is used to develop models at the cellular scale utilizing the Cellular Potts model (see Chapter 1 for additional details about CC3D). Folliculogenesis is a biological process that occurs at the cellular scale, thus CC3D was selected as the platform for model development. Data

about the preantral stages of folliculogenesis in rhesus macaques required for model development is based on the information needed to define parameters in a CC3D model.

Information needed for the development of a cell-based computational model of the preantral stages of folliculogenesis in rhesus macaques include molecular signaling data involved in growth and maturation of follicles and morphological data (i.e. follicle stages and abundances, growth rate of oocytes, proliferation rate of follicular cells, and sizes of follicles). This chapter describes preliminary steps in model development focused on gathering data about folliculogenesis in rhesus macaques. Data were collected from experimental studies in peer-reviewed literature and from histology slide analysis. Analysis of histology slides for morphological data captures the variance in data (e.g. follicle counts, spatial distribution of follicles) that is not always reported in the literature. In the cases when data do not exist, parameters must be fitted; strategies for fitting parameters are described in section 5.4 Preliminary Model Development. Data presented in this study can be used for the development of a CC3D model of the preantral stages of folliculogenesis.

## 5.2. Methods

The proposed model will simulate hormone independent folliculogenesis as it occurs prior to puberty, beginning on gestational day 130 and ending just prior to the onset of puberty. The model will simulate the growth and maturation of multiple follicles in a cross-section of the whole ovary, from primordial to secondary follicle stages (Fig. 5.1). Growth of oocytes, proliferation of granulosa cells, and any known signaling factors in

rhesus macaque will be simulated. To keep the model simple, it will focus on the growth of primordial follicles to secondary follicles and not morphological changes of other (non-follicular) somatic cells in the ovary (e.g. angiogenesis). The primary to secondary transition was also chosen since factors that regulate activation of primordial follicles are not known or well-studied in primates, relative to mice. Follicle growth will be programmed in the model using CC3D functions: Secretion Steppable, Diffusion Solver Steppable, Mitosis Steppable, Volume Steppable, and Cell Death Steppable (see Appendix 1 for descriptions of CC3D functions). The Secretion Steppable and Diffusion Solver Steppable govern molecular signaling (e.g. Anti-Mullerian hormone), while the Mitosis Steppable, Volume Steppable, and Cell Death Steppable control the morphological changes involved in the preantral stages of folliculogenesis. Data gathering was focused on defining parameters in the functions listed above (Table 5.1).

The model will be validated through assessment of morphology and follicle abundance from simulation results. The abundance of follicles and morphology in the model simulations will be compared with follicle abundance reported in the literature and experimental images of ovarian tissue in the literature from immature macaques (Baker & Franchi, 1972; Koering, Danforth, & Hodgen, 1994; Marr-Belvin et al., 2010; Nichols et al., 2005; Simpson & Van Wagenen, 1973).

### *5.2.1. Literature search*

A thorough literature search was conducted for preantral folliculogenesis data in rhesus macaque. Searches were done in Scopus for the following search terms “folliculogenesis” “ovarian follicle maturation”, “ovarian follicle growth”, “primordial

follicle", "primary follicle", secondary follicle", "follicle activation", and "ovarian development". Publications found were refined to studies in rhesus macaque and reviewed for folliculogenesis data. Some additional folliculogenesis data from other mammalian species was recorded.

### *5.2.2. Analysis of histology slides*

The preantral growth of ovarian follicles occurs following the formation of primordial follicles and continues until the end of the reproductive lifespan; to exclude variance that may occur due to age, histology analysis was restricted to ovarian tissue samples from rhesus macaques at gestational day 130 (in the third trimester). Pre-stained hematoxylin and eosin (H&E) stained ovarian tissue slides were provided by Dr. Mary Zelinski. Ovarian tissue was fixed in 4% paraformaldehyde (Sigma) overnight at 4°C (personal communication with M. Zelinkski). The following day, tissue was placed into 4% sucrose overnight and incubated at 4°C. Tissue was then placed into 70% ethanol at 4°C and embedded in paraffin within one week. Serial tissue sections (5 μm) were placed onto microscope slides. A subset of tissue sections (every $20^{th}$ section) was stained with hematoxylin and eosin (H&E) for morphological analyses.

Histology slides were analyzed for data about the stage and abundance of ovarian follicles, abundance of follicular cells and relative spatial scaling of cells and tissues in the ovary. Using Olympus cellSens Standard software (Eliceiri et al., 2012), photos of ovarian tissues at 20x magnification were taken on an Olympus DP72 camera connected to an Olympus BX40 compound microscope. Photos were then aligned using PTGui Pro software, creating an image of the entire tissue section. H&E stained sections from 50

randomly selected gestational day 130 ovarian tissue sections, from 5 animals, were analyzed for 1) follicle stages, 2) abundance of follicles, and 3) the spatial layout of follicle. Follicle stages were classified following the follicle architecture described in Erickson (Erickson); primordial follicles contain a single oocyte surrounded by one layer of squamous granulosa cells, primary follicles contain an oocyte surround by one layer of cuboidal granulosa cells, and secondary follicles contain an oocyte surrounded by at least two layers of granulosa cells and have theca cells present (Chapter 1, Fig. 1.4). Results for follicle stages and abundances of healthy, non-atretic follicles were recorded.

## 5.3. Results

Results from the literature are scarce and summarized in Table 5.2. Information of the abundance and sizes of follicles in primordial, primary, and secondary stages in rhesus macaque and baboon were reported. Data for the timeline of folliculogenesis, atretic rates of follicles, quantitative data for cell adhesion in ovarian follicles, and molecular signaling in rhesus macaques were not found in the literature search. Information in other species that could be used to help define parameters with absent data were also reported in Table 5.2. Data on molecular events governing preantral follicle development was scarce in rhesus macaques and other non-human primates, so data were recorded for mice and humans; the model would only incorporate signals confirmed in rhesus macaque. Abundances of follicles at various stages in non-human primates was found in baboons and recorded for rhesus macaque histology analysis. Data on the timing of folliculogenesis is from estimates in human folliculogenesis, however there is no concrete

evidence of the time interval for a resting primordial follicle to develop to an antral follicle.

Analysis of H&E stained ovarian tissue produced data for the abundance of follicles, stages of follicles, and spatial scaling of follicles (Table 5.3). Primordial follicles were the most abundant follicle stage observed in all ovaries at an average of about 207 primordial follicles per ovary cross-section. In pre-pubertal mammals, the majority of follicles observed are primordial stages, followed by primary and secondary (Amorim, Moya, Donnez, & Dolmans, 2016; McGee & Hsueh, 2000; Silva-Santos et al., 2013). An image of one the of ovarian tissue sections was selected as the representative image for all sections assessed to be used for PIFF design (Fig. 5.2).

## 5.4. Preliminary Model Development

This study presents data to be used to define parameters for preliminary development of a CC3D model of the preantral stages of folliculogenesis, focusing on the primary to secondary transition, in rhesus macaques. Morphological data was derived from the literature and from analysis of H&E stained ovarian tissues. Molecular signaling data was found in mice and humans; much of the known molecular signaling involved in the preantral stages of mammalian folliculogenesis has yet to be confirmed in rhesus macaques. For the purpose of model development, only data confirmed in rhesus macaque would be included; not enough molecular signaling data exists to construct a model of preantral follicle development for rhesus macaque at this time. Data defining molecular signaling, atresia rates, time periods that follicles reside in each stage, growth

rate of oocytes, and proliferation rates of follicular cells was not found in the literature and could not be determined from H&E stained ovarian tissue samples; these parameters could be fitted for model development, however this would limit the applications of the model (i.e. the model could not accurately be used to simulate reproductive disease). Data from other species, and parameters defined in other CC3D studies can be used to help fit parameters with absent data.

A preliminary CC3D model of the preantral stages of folliculogenesis can be developed using the data found in this study. The first step to constructing a CC3D model is the set up of the simulation domain; the spatial scaling of the domain can be set using an H&E stained ovarian tissue image that is representative of all tissues analyzed (i.e. Chapter 1, Fig. 1.4). Cell types defined in the initial layout will include those important for follicle growth (e.g. oocyte, granulosa cells, theca cells). Vasculature and interstitial cells will be categorized as individual stromal cells to simplify the model; specification of stromal cell types would increase the model complexity. Angiogenesis during follicle growth is not included in this preliminary model, but could be a future direction of model development once the initial model of folliculogenesis in rhesus macaque has been constructed. The initial model will focus on simulating the growth of multiple follicles in the ovary (Fig. 5.1) using functions summarized in Table 5.1.

Parameters controlling volume (i.e. initial volume, target volume) will be defined with data from the literature search and from relative sizes of cells in H&E stained ovarian tissue images. The lambda volume and growth rate will be fitted. The timeline for *in vivo* activation of primordial follicles and their growth rate for rhesus macaque is unknown, but can be fitted in the model using data on the estimated time periods that

human ovarian follicles remain in primordial, primary, and secondary stages (Gougeon, 1986). Growth rates from *in vitro* follicle maturation can additionally be used to determine the timeline. *In vitro* studies where primary follicles are cultured in a 3-dimensional alginate matrix and exposed to follicle stimulating hormone (FSH), have shown primary follicles reaching the secondary stage in four weeks, forming an antrum in nine weeks, and developing to the small antral stage in thirteen weeks (Xu et al., 2013). Follicle growth beginning with secondary follicles, using the same in vitro maturation methods, have shown three weeks for an antrum to form and five weeks to reach the small antral stage. Not all follicles possess the same growth potential in culture (see Xu et al. 2013 for more information about fast-growing, slow-growing, and non-growing follicles).

The model will simulate the proliferation of granulosa and theca cells; no data for the mitotic rate of follicular cells in primates exists, so the rate must be fitted. The timeline of follicle growth combined with follicle sizes will be used to estimate the mitotic rate for granulosa and theca cells. There has been recent debate about the about the presence of ovarian stem cells contributing the ovarian follicle pool in mammals, though it has not yet been reported in rhesus macaques (D. Bhartiya et al., 2013; Guo et al., 2016; Lei & Spradling, 2013a; Parte et al., 2014; Zhang et al., 2012). To simplify the model, an assumption will be made that the primordial follicle pool does not grow.

During folliculogenesis, follicles are selected for either continued growth or to undergo atresia. In pre-pubertal folliculogenesis, the absence of rising levels of FSH support causes growing follicles to become atretic (Kaipia & Hsueh, 1997). Atretic rates will be fitted from data in other species on the depletion of the primordial follicle pool

(Donnez & Dolmans, 2013; McLaughlin, Kelsey, Wallace, Anderson, & Telfer, 2015; Visser, Schipper, Laven, & Themmen, 2012; Wallace & Kelsey, 2010).

The Contact Energy Plugin describes cellular adhesion between cell types and is used in the model to represent the spatial distribution of cell types (e.g. oocytes surrounded by granulosa cells). Quantitative data for cellular adhesion in follicular cells does not exist, so parameters defining Contact Energy must be fitted to represent the layout of cell types observed in ovarian tissue slides.

Molecular signaling in the model will be simulated by the secretion, diffusion, and decay of chemical fields. The presence or absence of a chemical field can be programmed in the model to control other functions (i.e. the secretion of Anti-Mullerian hormone by granulosa cells controlling growth of the oocyte). Data on the secretion rate and diffusion rate will be fitted.

## 5.5. Discussion

Data gathered from the literature review and analysis of ovarian tissue histology provided a baseline of information that can be used for the development of a preliminary CC3D model. Results provide enough information to simulate the morphological changes associated with the preantral stages of folliculogenesis (e.g. oocyte size, follicle size, distribution of follicles in the young macaque ovary). Cĺement et al. (Cĺement, Michel, Monniaux, & Stiehl) modeled spatial ovarian follicle development, that is oocyte growth and follicular cell proliferation in a single oocyte associated with molecular signals in sheep. Data used to develop the sheep model are similar to the data collected for the

rhesus macaque model. The sheep model simulates the average growth rate of an oocyte and average proliferation rates of the surrounding granulosa cells and the associated molecular signals. The proposed folliculogenesis model would simulate oocyte growth and granulosa cell proliferation associated with known signaling, and additionally the variation in growth and proliferation rates by simulating the maturation of multiple follicles. The model would also make predictions about the timeline of folliculogenesis from estimates in humans and *in vitro* rhesus macaque data. Additional information is necessary for the development of a model of the preantral stages of folliculogenesis in rhesus macaque and application of the model (e.g. tool for reproductive disease), however the data from this study provides a baseline for model development. The preliminary model will be verified from analyses of ovarian tissues sections and follicle counts from prepubertal rhesus macaques.

The temporal scale of follicle development *in vivo* was not found in the literature search and is necessary to model the growth of oocytes and proliferation of granulosa and theca cells at the same rate that would occur *in vivo*. As a surrogate, temporal data may be derived from assumptions about the percentage of activated follicles at later prepubertal stages and *in vitro* data on atretic rates of follicles. Other than information on the role of androgens in primordial follicle activation, data on the molecular signaling mechanisms governing the preantral stages of folliculogenesis in rhesus macaque is limited to data collected from *in vitro* follicle culture studies wherein requirements for gonadotropins, insulin, and steroids have been established (Rodrigues, Navarro, Zelinski, Stouffer, & Xu, 2015; A. Y. Ting, Xu, & Stouffer, 2015). Incorporating experimentally verified molecular signaling mechanisms is crucial for applying the model as a tool for

making predictions, evaluating hypothesis, and studying reproductive diseases. To overcome the deficit, data on the temporal scale and molecular signaling in folliculogenesis in humans could be assumed for rhesus macaque until data are accumulated due to the similarity between human and rhesus macaque ovarian physiology.

The spatial development of multiple follicles in rhesus macaque can be simulated, however the model would have insufficient information to be applied for studying reproductive toxicity and disease. Once molecular signaling data and temporal activation of follicle growth is acquired in rhesus macaque, a model of the preantral growth of follicles in rhesus macaque can be constructed.

### *Future Work*

Future work with this research would include the construction of a CC3D model of the preantral stages of folliculogenesis (as outlined in section 5.4 Preliminary Model Development) and extending the model to include the antral stages of folliculogenesis. Continuation of morphological development, angiogenesis, molecular signaling mechanisms, and cyclical hormone signaling could be incorporated in the extended model. Molecular signaling mechanisms involved in folliculogenesis that have been studied in other organisms (e.g. mouse, human) need to be verified in rhesus macaque to better apply the model as a tool for studying folliculogenesis and associated reproductive diseases.

A CC3D model of the preantral stages of folliculogenesis in rhesus macaques can be applied as a tool to predict follicle pool sizes, study reproductive diseases, test

hypotheses, and as an educational resource. The model could be used to predict how disruptions to normal processes in preantral stages of the folliculogenesis affect the follicle pool size (e.g. increased percentage of activated follicles, slower follicle growth rate). For example, polycystic ovary syndrome is a reproductive disease that results an increased number of activated follicles associated with a greater presence of androgens (Beck-Peccoz & Persani, 2006; Homburg, 2008). A future model of folliculogenesis could be used as a tool for understanding polycystic ovary syndrome by using the model to study the relationship between androgen levels and follicle activation once information on molecular signaling is acquired. A future folliculogenesis model could also be used as a tool to study premature ovarian insufficiency. Premature ovarian insufficiency leads to early depletion of ovarian follicles and has multiple causes (e.g. follicle-stimulating-hormone-receptor mutation, aromatase deficiency, trisomy) (De Vos, Devroey, & Fauser, 2010). Chemotherapy treatments can also cause early depletion of ovarian follicles through oocyte cytotoxicity (Blumenfeld, 2012). A future model of folliculogenesis can be used to assess the risk of follicle depletion in cases of premature ovarian insufficiency or cases of chemotherapy treatment. Studying factors that contribute to the production of a fertilizable egg is important for understanding reproduction and reproductive diseases in rhesus macaque.

The model can also be used a tool for predicting hypothesized mechanisms and processes in the preantral stages of folliculogenesis. For instance, hypotheses about the role of ovarian stem cells in the follicle pool size could be tested by incorporating ovarian stem cell types in a future version of the model. Molecular mechanisms governing folliculogenesis in other species (e.g. mouse, human) could be tested in the model to

predict some of the molecular processes involved in folliculogenesis in rhesus macaque. Additionally, hypotheses about the timeline of follicle growth could also be tested by altering growth and proliferation rates in a folliculogenesis model.

Last, the model could be used as an educational resource for teaching about the molecular signaling and morphological changes in the preantral stages of folliculogenesis in rhesus macaque. The model would integrate data from multiple highly specific studies to capture the physiology of the whole ovary during folliculogenesis; the model could be used to teach about the relationships between biological processes that lead to normal ovarian function and how dysfunction may result in adverse outcomes. Data in this study provide the foundations for developing a CC3D model of folliculogenesis in rhesus macaque.

## REFERENCES


Abbott, D. H., Nicol, L. E., Levine, J. E., Xu, N., Goodarzi, M. O., & Dumesic, D. A. (2013). Nonhuman primate models of polycystic ovary syndrome. *Molecular and Cellular Endocrinology, 373*(0), 21-28. doi:10.1016/j.mce.2013.01.013

Abdulla, T., Imms, R., Dillenseger, J. L., Schleich, J. M., & Summersa, R. (2011). Computational modelling of epithelial to mesenchymal transition. *IRBM, 32*(5), 306-310. doi:10.1016/j.irbm.2011.09.001

Achermann, J. C., Meeks, J. J., & Jameson, J. L. (2001). Phenotypic spectrum of mutations in DAX-1 and SF-1. *Mol Cell Endocrinol, 185*(1-2), 17-25. doi:10.1016/S0303-7207(01)00619-0

Acton, A. Q. (2012). *Ovarian Diseases—Advances in Research and Treatment: 2012 Edition*: ScholaryEditions.

Amorim, C. A., Moya, C. F., Donnez, J., & Dolmans, M. M. (2016). Morphometric characteristics of preantral and antral follicles and expression of factors involved in folliculogenesis in ovaries of adult baboons (Papio anubis). *Journal of Assisted Reproduction and Genetics, 33*(5), 617-626. doi:10.1007/s10815-016-0681-9

Ancelin, K., Lange, U. C., Hajkova, P., Schneider, R., Bannister, A. J., Kouzarides, T., & Surani, M. A. (2006). Blimp1 associates with Prmt5 and directs histone arginine methylation in mouse germ cells. *Nature Cell Biology, 8*(6), 623-630. doi:10.1038/ncb1413

Anderson, E. L., Baltus, A. E., Roepers-Gajadien, H. L., Hassold, T. J., De Rooij, D. G., Van Pelt, A. M. M., & Page, D. C. (2008). Stra8 and its inducer, retinoic acid, regulate meiotic initiation in both spermatogenesis and oogenesis in mice. *Proceedings of the National Academy of Sciences of the United States of America, 105*(39), 14976-14980. doi:10.1073/pnas.0807297105

Aramaki, S., Hayashi, K., Kurimoto, K., Ohta, H., Yabuta, Y., Iwanari, H., . . . Saitou, M. (2013). A mesodermal factor, T, specifies mouse germ cell fate by directly activating germline determinants. *Developmental Cell, 27*(5), 516-529. doi:10.1016/j.devcel.2013.11.001

Baker, T. G., & Franchi, L. L. (1972). The fine structure of oogonia and oocytes in the rhesus monkey (Macaca mulatta). *Zeitschrift für Zellforschung und Mikroskopische Anatomie, 126*(1), 53-74. doi:10.1007/BF00306780

Baltus, A. E., Menke, D. B., Hu, Y. C., Goodheart, M. L., Carpenter, A. E., Rooij, D. G., & Page, D. C. (2006). In germ cells of mouse embryonic ovaries, the decision to enter meiosis precedes premeiotic DNA replication. *Nat Genet, 38*. doi:10.1038/ng1919

Beck-Peccoz, P., & Persani, L. (2006). Premature ovarian failure. *Orphanet Journal of Rare Diseases, 1*(1), 1-5. doi:10.1186/1750-1172-1-9

Bendel-Stenzel, M. R., Gomperts, M., Anderson, R., Heasman, J., & Wylie, C. (2000). The role of cadherins during primordial germ cell migration and early gonad

formation in the mouse. *Mechanisms of Development, 91*(1-2), 143-152. doi:10.1016/S0925-4773(99)00287-7

Benedict, J. C., Lin, T. M., Loeffler, I. K., Peterson, R. E., & Flaws, J. A. (2000). Physiological role of the aryl hydrocarbon receptor in mouse ovary development. *Toxicological Sciences, 56*(2), 382-388.

Bhartiya, D., Sriraman, K., Gunjal, P., & Modak, H. (2012). Gonadotropin treatment augments postnatal oogenesis and primordial follicle assembly in adult mouse ovaries? *Journal of Ovarian Research, 5*, 32-32. doi:10.1186/1757-2215-5-32

Bhartiya, D., Unni, S., Parte, S., & Anand, S. (2013). Very small embryonic-like stem cells: Implications in reproductive biology. *BioMed Research International, 2013*. doi:10.1155/2013/682326

Birk, O. S., Caslano, D. E., Wassif, C. A., Cogilatl, T., Zhaos, L., Zhao, Y., . . . Parker, K. L. (2000). The LIM homeobox gene Lhx9 is essential for mouse gonad formation. *Nature, 403*. doi:10.1038/35002622

Blumenfeld, Z. (2012). Chemotherapy and fertility. *Best Practice and Research: Clinical Obstetrics and Gynaecology, 26*(3), 379-390. doi:10.1016/j.bpobgyn.2011.11.008

Boas, S. E. M., & Merks, R. M. H. (2014). Synergy of cell-cell repulsion and vacuolation in a computational model of lumen formation. *Journal of the Royal Society Interface, 11*(92). doi:10.1098/rsif.2013.1049

Bowles, J., Knight, D., Smith, C., Wilhelm, D., Richman, J., Mamiya, S., . . . Rossant, J. (2006). Retinoid signaling determines germ cell fate in mice. *Science, 312*. doi:10.1126/science.1125691

Brewer, M., Baze, W., Hill, L., Utzinger, U., Wharton, J. T., Follen, M., . . . Satterfield, W. (2001). Rhesus macaque model for ovarian cancer chemoprevention. *Comparative Medicine, 51*(5), 424-429.

Brodland, G. W. (2015). How computational models can help unlock biological systems. *Seminars in Cell & Developmental Biology, 47–48*, 62-73. doi:http://dx.doi.org/10.1016/j.semcdb.2015.07.001

Bukovsky, A. (2011). Ovarian Stem Cell Niche and Follicular Renewal in Mammals. *The anatomical record : advances in integrative anatomy and evolutionary biology., 294*(8), 1284-1306. doi:10.1002/ar.21422

Cannistra, S. A. (2004). Cancer of the ovary. *New England Journal of Medicine, 351*(24). doi:10.1056/NEJMra041842

Castrillon, D. H., Miao, L., Kollipara, R., Horner, J. W., & DePinho, R. A. (2003). Suppression of ovarian follicle activation in mice by the transcription factor Foxo3a. *Science, 301*(5630), 215-218. doi:10.1126/science.1086336

Chassot, A. A., Ranc, F., Gregoire, E. P., Roepers-Gajadien, H. L., Taketo, M. M., Camerino, G., . . . Chaboissier, M. C. (2008). Activation of β-catenin signaling by Rspo1 controls differentiation of the mammalian ovary. *Human Molecular Genetics, 17*(9), 1264-1277. doi:10.1093/hmg/ddn016

Chen, Y., Jefferson, W. N., Newbold, R. R., Padilla-Banks, E., & Pepling, M. E. (2007). Estradiol, progesterone, and genistein inhibit oocyte nest breakdown and primordial follicle assembly in the neonatal mouse ovary in vitro and in vivo. *Endocrinology, 148*(8), 3580-3590. doi:10.1210/en.2007-0088

Choi, Y., Yuan, D., & Rajkovic, A. (2008). Germ cell-specific transcriptional regulator Sohlh2 is essential for early mouse folliculogenesis and oocyte-specific gene expression. *Biology of Reproduction, 79*(6), 1176-1182. doi:10.1095/biolreprod.108.071217

Cĺement, F., Michel, P., Monniaux, D., & Stiehl, T. (2013). Coupled somatic cell kinetics and germ cell growth: Multiscale model-based insight on ovarian follicular development. *Multiscale Modeling and Simulation, 11*(3), 719-746. doi:10.1137/120897249

Cook, M. S., Coveney, D., Batchvarov, I., Nadeau, J. H., & Capel, B. (2009). BAX-mediated cell death affects early germ cell loss and incidence of testicular teratomas in Dnd1Ter/Ter mice. *Developmental Biology, 328*(2), 377-383. doi:10.1016/j.ydbio.2009.01.041

Crisponi, L., Deiana, M., Loi, A., Chiappe, F., Uda, M., Amati, P., . . . Pilia, G. (2001). The putative forkhead transcription factor FOXL2 is mutated in blepharophimosis/ptosis/epicanthus inversus syndrome. *Nature Genetics, 27*(2), 159-166. doi:10.1038/84781

De Sousa Lopes, S. M. C., Hayashi, K., & Surani, M. A. (2007). Proximal visceral endoderm and extraembryonic ectoderm regulate the formation of primordial germ cell precursors. *BMC Developmental Biology, 7*. doi:10.1186/1471-213X-7-140

De Vos, M., Devroey, P., & Fauser, B. C. J. M. (2010). Primary ovarian insufficiency. *The Lancet, 376*(9744), 911-921. doi:http://dx.doi.org/10.1016/S0140-6736(10)60355-8

Di Carlo, A., & De Felici, M. (2000). A role for E-cadherin in mouse primordial germ cell development. *Developmental Biology, 226*(2), 209-219. doi:10.1006/dbio.2000.9861

Dizerega, G. S., & Hodgen, G. D. (1981). Folliculogenesis in the Primate Ovarian Cycle. *Endocrine Reviews, 2*(1), 27-49. doi:10.1210/edrv-2-1-27

Doitsidou, M., Reichman-Fried, M., Stebler, J., Köprunner, M., Dörries, J., Meyer, D., . . . Raz, E. (2002). Guidance of primordial germ cell migration by the chemokine SDF-1. *Cell, 111*(5), 647-659. doi:10.1016/S0092-8674(02)01135-2

Donnez, J., & Dolmans, M.-M. (2013). Fertility preservation in women. *Nat Rev Endocrinol, 9*(12), 735-749. doi:10.1038/nrendo.2013.205

Dunlop, C. E., & Anderson, R. A. (2014). The regulation and assessment of follicular growth. *Scandinavian Journal of Clinical and Laboratory Investigation, 74*(SUPPL. 244), 13-17. doi:10.3109/00365513.2014.936674

Edson, M. A., Nagaraja, A. K., & Matzuk, M. M. (2009). The mammalian ovary from genesis to revelation. *Endocrine Reviews, 30*(6), 624-712. doi:10.1210/er.2009-0012

Eliceiri, K. W., Berthold, M. R., Goldberg, I. G., Ibanez, L., Manjunath, B. S., Martone, M. E., . . . Carpenter, A. E. (2012). Biological imaging software tools. *Nat Meth, 9*(7), 697-710.

Elliman, S. J., Wu, I., & Kemp, D. M. (2006). Adult tissue-specific expression of a Dppa3-derived retrogene represents a postnatal transcript of pluripotent cell origin. *Journal of Biological Chemistry, 281*(1), 16-19. doi:10.1074/jbc.C500415200

Erickson, G. F. (1995). The ovary: Basic principles and concepts. *Endocrinology and Metabolism. New York: McGraw-Hill*, 973-1048.

Francis, R. J. B., & Lo, C. W. (2006). Primordial germ cell deficiency in the connexin 43 knockout mouse arises from apoptosis associated with abnormal p53 activation. *Development, 133*(17), 3451-3460. doi:10.1242/dev.02506

Gao, X., Tangney, M., & Tabirca, S. (2011). *A multiscale model for hypoxia-induced avascular tumor growth.* Paper presented at the Proceedings of the International Conference on Bioscience, Biochemistry and Bioinformatics (IPCBEE): 26–28 February 2011; Singapore. Volume.

Ginsburg, M., Snow, M. H. L., & McLaren, A. (1990). Primordial germ cells in the mouse embryo during gastrulation. *Development, 110*(2), 521-528.

Gosden, R., & Lee, B. (2010). Portrait of an oocyte: our obscure origin. *The Journal of Clinical Investigation, 120*(4), 973-983. doi:10.1172/JCI41294

Gougeon, A. (1986). Dynamics of follicular growth in the human: A model from preliminary results. *Human Reproduction, 1*(2), 81-87.

Graner, F., & Glazier, J. A. (1992). Simulation of biological cell sorting using a two-dimensional extended Potts model. *Physical review letters, 69*(13), 2013.

Griffin, J., Emery, B. R., Huang, I., Peterson, C. M., & Carrell, D. T. (2006). Comparative analysis of follicle morphology and oocyte diameter in four mammalian species (mouse, hamster, pig, and human). *Journal of Experimental and Clinical Assisted Reproduction, 3*. doi:10.1186/1743-1050-3-2

Gu, Y., Runyan, C., Shoemaker, A., Surani, A., & Wylie, C. (2009). Steel factor controls primordial germ cell survival and motility from the time of their specification in the allantois, and provides a continuous niche throughout their migration. *Development, 136*(8), 1295-1303. doi:10.1242/dev.030619

Guo, K., Li, C.-h., Wang, X.-y., He, D.-j., & Zheng, P. (2016). Germ stem cells are active in postnatal mouse ovary under physiological conditions. *Molecular Human Reproduction, 22*(5), 316-328. doi:10.1093/molehr/gaw015

Haglund, K., Nezis, I. P., & Stenmark, H. (2011). Structure and functions of stable intercellular bridges formed by incomplete cytokinesis during development. *Communicative and Integrative Biology, 4*(1), 1-9. doi:10.4161/cib.4.1.13550

Hamilton, M. (2012). Infertility *Dewhurst's Textbook of Obstetrics & Gynaecology: Eighth Edition* (pp. 565-579).

Heaney, J. D., Anderson, E. L., Michelson, M. V., Zechel, J. L., Conrad, P. A., Page, D. C., & Nadeau, J. H. (2012). Germ cell pluripotency, premature differentiation and susceptibility to testicular teratomas in mice. *Development, 139*(9), 1577-1586. doi:10.1242/dev.076851

Homburg, R. (2008). Polycystic ovary syndrome. *Best Practice & Research Clinical Obstetrics & Gynaecology, 22*(2), 261-274. doi:http://dx.doi.org/10.1016/j.bpobgyn.2007.07.009

Iber, D., & Geyter, C. D. (2013). Computational modelling of bovine ovarian follicle development. *BMC Systems Biology, 7*. doi:10.1186/1752-0509-7-60

Imudia, A. N., Wang, N., Tanaka, Y., White, Y. A. R., Woods, D. C., & Tilly, J. L. (2013). Comparative gene expression profiling of adult mouse ovary-derived oogonial stem cells supports a distinct cellular identity. *Fertility and sterility, 100*(5), 1451-1458. doi:10.1016/j.fertnstert.2013.06.036

Johnson, J., Canning, J., Kaneko, T., Pru, J. K., & Tilly, J. L. (2004). Germline stem cells and follicular renewal in the postnatal mammalian ovary. *Nature, 428*(6979), 145-150. doi:http://www.nature.com/nature/journal/v428/n6979/suppinfo/nature02316_S1.html

Jose-Miller, A. B., Boyden, J. W., & Frey, K. A. (2007). Infertility. *American Family Physician, 75*(6).

Kaipia, A., & Hsueh, A. J. W. (1997) Regulation of ovarian follicle atresia. *Vol. 59. Annual Review of Physiology* (pp. 349-363).

Kleinstreuer, N., Dix, D., Rountree, M., Baker, N., Sipes, N., Reif, D., . . . Knudsen, T. (2013). A Computational Model Predicting Disruption of Blood Vessel Development. *PLoS Comput Biol, 9*(4), e1002996. doi:10.1371/journal.pcbi.1002996

Knaut, H., Werz, C., Geisler, R., Busch-Nentwich, E., Dahm, R., Frohnhöfer, H. G., . . . Hooge, J. (2003). A zebrafish homologue of the chemokine receptor Cxcr4 is a germ-cell guidance receptor. *Nature, 421*. doi:10.1038/nature01338

Koering, M. J., Danforth, D. R., & Hodgen, G. D. (1994). Early follicle growth in the juvenile Macaca monkey ovary: The effects of estrogen priming and follicle-stimulating hormone. *Biology of Reproduction, 50*(3), 686-694.

Kouznetsova, A., Benavente, R., Pastink, A., & Höög, C. (2011). Meiosis in mice without a synaptonemal complex. *PLoS ONE, 6*(12). doi:10.1371/journal.pone.0028255

Kozlovsky, P., & Gefen, A. (2013). Sperm penetration to the zona pellucida of an oocyte: a computational model incorporating acrosome reaction. *Computer Methods in Biomechanics and Biomedical Engineering, 16*(10), 1106-1111. doi:10.1080/10255842.2013.768618

Krewski, D., Acosta, D., Andersen, M., Anderson, H., Bailar, J. C., Boekelheide, K., . . . Zeise, L. (2010). Toxicity testing in the 21st century: A vision and a strategy. *Journal of Toxicology and Environmental Health - Part B: Critical Reviews, 13*(2-4), 51-138. doi:10.1080/10937404.2010.483176

Kurimoto, K., Yabuta, Y., Ohinata, Y., Shigeta, M., Yamanaka, K., & Saitou, M. (2008). Complex genome-wide transcription dynamics orchestrated by Blimp1 for the specification of the germ cell lineage in mice. *Genes and Development, 22*(12), 1617-1635. doi:10.1101/gad.1649908

Lanner, F. (2014). Lineage specification in the early mouse embryo. *Experimental Cell Research, 321*(1), 32-39. doi:10.1016/j.yexcr.2013.12.004

Lawson, K. A., Dunn, N. R., Roelen, B. A. J., Zeinstra, L. M., Davis, A. M., Wright, C. V. E., . . . Hogan, B. L. M. (1999). Bmp4 is required for the generation of primordial germ cells in the mouse embryo. *Genes and Development, 13*(4), 424-436.

Lei, L., Jin, S., Mayo, K. E., & Woodruff, T. K. (2010). The interactions between the stimulatory effect of follicle-stimulating hormone and the inhibitory effect of estrogen on mouse primordial folliculogenesis. *Biology of Reproduction, 82*(1), 13-22. doi:10.1095/biolreprod.109.077404

Lei, L., & Spradling, A. C. (2013a). Female mice lack adult germ-line stem cells but sustain oogenesis using stable primordial follicles. *Proceedings of the National Academy of Sciences of the United States of America, 110*(21), 8585-8590. doi:10.1073/pnas.1306189110

Lei, L., & Spradling, A. C. (2013b). Mouse primordial germ cells produce cysts that partially fragment prior to meiosis. *Development (Cambridge), 140*(10), 2075-2081. doi:10.1242/dev.093864

Li, Z., Kroll, K. J., Jensen, K. M., Villeneuve, D. L., Ankley, G. T., Brian, J. V., . . . Watanabe, K. H. (2011). A computational model of the hypothalamic - pituitary - gonadal axis in female fathead minnows (Pimephales promelas) exposed to 17α-ethynylestradiol and 17β-trenbolone. *BMC Systems Biology, 5*. doi:10.1186/1752-0509-5-63

Liang, L. F., Soyal, S. M., & Dean, J. (1997). FIGα, a germ cell specific transcription factor involved in the coordinate expression of the zona pellucida genes. *Development, 124*(24), 4939-4947.

Liu, C. F., Bingham, N., Parker, K., & Yao, H. H. C. (2009). Sex-specific roles of β-catenin in mouse gonadal development. *Hum Mol Genet, 18*. doi:10.1093/hmg/ddn362

Lu, Z., Wu, M., Zhang, J., Xiong, J., Cheng, J., Shen, W., . . . Wang, S. (2016). Improvement in isolation and identification of mouse oogonial stem cells. *Stem Cells International, 2016*. doi:10.1155/2016/2749461

MacGregor, G. R., Zambrowicz, B. P., & Soriano, P. (1995). Tissue non-specific alkaline phosphatase is expressed in both embryonic and extraembryonic lineages during

mouse embryogenesis but is not required for migration of primordial germ cells. *Development, 121*(5), 1487-1496.

Manuylov, N. L., Smagulova, F. O., Leach, L., & Tevosian, S. G. (2008). Ovarian development in mice requires the GATA4-FOG2 transcription complex. *Development, 135*(22), 3731-3743. doi:10.1242/dev.024653

Marr-Belvin, A. K., Bailey, C. C., Knight, H. L., Klumpp, S. A., Westmoreland, S. V., & Miller, A. D. (2010). Ovarian pathology in rhesus macaques: A 12-year retrospective. *Journal of Medical Primatology, 39*(3), 170-176. doi:10.1111/j.1600-0684.2010.00409.x

McCoshen, J. A., & McCallion, D. J. (1975). A study of the primordial germ cells during their migratory phase in steel mutant mice. *Experientia, 31*(5), 589-590. doi:10.1007/BF01932475

McGee, E. A., & Hsueh, A. J. W. (2000). Initial and cyclic recruitment of ovarian follicles. *Endocrine Reviews, 21*(2), 200-214. doi:10.1210/er.21.2.200

McLaren, A., & Chuva de Sousa Lopes, S. M. (2009). Primordial Germ Cells in Mouse and Human *Essentials of Stem Cell Biology* (pp. 131-136).

McLaughlin, M., Kelsey, T. W., Wallace, W. H. B., Anderson, R. A., & Telfer, E. E. (2015). An externally validated age-related model of mean follicle density in the cortex of the human ovary. *Journal of Assisted Reproduction and Genetics, 32*(7), 1089-1095. doi:10.1007/s10815-015-0501-7

Merks, R. M. H., & Glazier, J. A. (2005). A cell-centered approach to developmental biology. *Physica A: Statistical Mechanics and its Applications, 352*(1), 113-130. doi:10.1016/j.physa.2004.12.028

Miyamoto, N., Yoshida, M., Kuratani, S., Matsuo, I., & Aizawa, S. (1997). Defects of urogenital development in mice lacking Emx2. *Development, 124*(9), 1653-1664.

Mizusaki, H., Kawabe, K., Mukai, T., Ariyoshi, E., Kasahara, M., Yoshioka, H., . . . Morohashi, K. I. (2003). Dax-1 (dosage-sensitive sex reversal-adrenal hypoplasia congenita critical region on the X chromosome, gene 1) gene transcription is regulated by Wnt4 in the female developing gonad. *Molecular Endocrinology, 17*(4), 507-519. doi:10.1210/me.2002-0362

Molyneaux, K., & Wylie, C. (2004). Primordial germ cell migration. *International Journal of Developmental Biology, 48*(5-6), 537-544. doi:10.1387/ijdb.041833km

Molyneaux, K. A., Zinszner, H., Kunwar, P. S., Schaible, K., Stebler, J., Sunshine, M. J., . . . Wylie, C. (2003). The chemokine SDF1/CXCL12 and its receptor CXCR4 regulate mouse germ cell migration and survival. *Development, 130*. doi:10.1242/dev.00640

Mortazavi, V., D'Souza, R. M., & Nosonovsky, M. (2013). Study of contact angle hysteresis using the Cellular Potts Model. *Physical Chemistry Chemical Physics, 15*(8), 2749-2756.

Nelson, L. M. (2009). Primary Ovarian Insufficiency. *New England Journal of Medicine, 360*(6), 606-614. doi:10.1056/NEJMcp0808697

Nichols, S. M., Bavister, B. D., Brenner, C. A., Didier, P. J., Harrison, R. M., & Kubisch, H. M. (2005). Ovarian senescence in the rhesus monkey (Macaca mulatta). *Human reproduction (Oxford, England), 20*(1), 79-83. doi:10.1093/humrep/deh576

Niikura, Y., Niikura, T., & Tilly, J. L. (2009). Aged mouse ovaries possess rare premeiotic germ cells that can generate oocytes following transplantation into a young host environment. *Aging (Albany NY), 1*(12), 971-978.

Ohinata, Y., Ohta, H., Shigeta, M., Yamanaka, K., Wakayama, T., & Saitou, M. (2009). A Signaling Principle for the Specification of the Germ Cell Lineage in Mice. *Cell, 137*(3), 571-584. doi:10.1016/j.cell.2009.03.014

Ohinata, Y., Payer, B., O'Carroll, D., Ancelin, K., Ono, Y., Sano, M., . . . Surani, M. A. (2005). Blimp1 is a critical determinant of the germ cell lineage in mice. *Nature, 436*(7048), 207-213. doi:10.1038/nature03813

Oktem, O., & Urman, B. (2010). Understanding follicle growth in vivo. *Human Reproduction, 25*(12), 2944-2954. doi:10.1093/humrep/deq275

Pacchiarotti, J., Maki, C., Ramos, T., Marh, J., Howerton, K., Wong, J., . . . Izadyar, F. (2010). Differentiation potential of germ line stem cells derived from the postnatal mouse ovary. *Differentiation, 79*(3), 159-170. doi:http://dx.doi.org/10.1016/j.diff.2010.01.001

Pangas, S. A., Choi, Y., Ballow, D. J., Zhao, Y., Westphal, H., Matzuk, M. M., & Rajkovic, A. (2006). Oogenesis requires germ cell-specific transcriptional regulators Sohlh1 and Lhx8. *Proceedings of the National Academy of Sciences of the United States of America, 103*(21), 8090-8095. doi:10.1073/pnas.0601083103

Parte, S., Bhartiya, D., Patel, H., Daithankar, V., Chauhan, A., Zaveri, K., & Hinduja, I. (2014). Dynamics associated with spontaneous differentiation of ovarian stem cells in vitro. *Journal of Ovarian Research, 7*(1). doi:10.1186/1757-2215-7-25

Peters, H. (1969). The development of the mouse ovary from birth to maturity. *Acta Endocrinologica, 62*(1), 98-116.

Quignot, N., & Bois, F. Y. (2013). A Computational Model to Predict Rat Ovarian Steroid Secretion from In Vitro Experiments with Endocrine Disruptors. *PLoS ONE, 8*(1). doi:10.1371/journal.pone.0053891

Raies, A. B., & Bajic, V. B. (2016). In silico toxicology: Computational methods for the prediction of chemical toxicity. *Wiley Interdisciplinary Reviews: Computational Molecular Science*. doi:10.1002/wcms.1240

Rajkovic, A., Pangas, S. A., Ballow, D., Suzumori, N., & Matzuk, M. M. (2004). NOBOX deficiency disrupts early folliculogenesis and oocyte-specific gene expression. *Science, 305*(5687), 1157-1159. doi:10.1126/science.1099755

Richards, J. S., & Pangas, S. A. (2010). The ovary: basic biology and clinical implications. *The Journal of Clinical Investigation, 120*(4), 963-972. doi:10.1172/JCI41350

Richardson, B. E., & Lehmann, R. (2010). Mechanisms guiding primordial germ cell migration: Strategies from different organisms. *Nature Reviews Molecular Cell Biology, 11*(1), 37-49. doi:10.1038/nrm2815

Rizzino, A. (2009). Sox2 and Oct-3/4: A versatile pair of master regulators that orchestrate the self-renewal and pluripotency of embryonic stem cells. *Wiley Interdisciplinary Reviews: Systems Biology and Medicine, 1*(2), 228-236. doi:10.1002/wsbm.12

Rodrigues, J. K., Navarro, P. A., Zelinski, M. B., Stouffer, R. L., & Xu, J. (2015). Direct actions of androgens on the survival, growth and secretion of steroids and anti-Mü llerian hormone by individual macaque follicles during three-dimensional culture. *Human Reproduction, 30*(3), 664-674. doi:10.1093/humrep/deu335

Runyan, C., Schaible, K., Molyneaux, K., Wang, Z., Levin, L., & Wylie, C. (2006). Steel factor controls midline cell death of primordial germ cells and is essential for their normal proliferation and migration. *Development, 133*(24), 4861-4869. doi:10.1242/dev.02688

Saba, R., Wu, Q., & Saga, Y. (2014). CYP26B1 promotes male germ cell differentiation by suppressing STRA8-dependent meiotic and STRA8-independent mitotic pathways. *Developmental Biology, 389*(2), 173-181. doi:http://dx.doi.org/10.1016/j.ydbio.2014.02.013

Saitou, M. (2009). Germ cell specification in mice. *Current Opinion in Genetics and Development, 19*(4), 386-395. doi:10.1016/j.gde.2009.06.003

Sarraj, M. A., & Drummond, A. E. (2012). Mammalian foetal ovarian development: Consequences for health and disease. *Reproduction, 143*(2), 151-163. doi:10.1530/REP-11-0247

Scianna, M., & Preziosi, L. (2012). Hybrid Cellular Potts Model for Solid Tumor Growth *New Challenges for Cancer Systems Biomedicine* (pp. 205-224): Springer.

Sekl, Y., Yamaji, M., Yabuta, Y., Sano, M., Shigeta, M., Matsui, Y., . . . Saitou, M. (2007). Cellular dynamics associated with the genome-wide epigenetic reprogramming in migrating primordial germ cells in mice. *Development, 134*(14), 2627-2638. doi:10.1242/dev.005611

Shirinifard, A., Gens, J. S., Zaitlen, B. L., Popławski, N. J., Swat, M., & Glazier, J. A. (2009). 3D Multi-Cell Simulation of Tumor Growth and Angiogenesis. *PLoS ONE, 4*(10), e7190. doi:10.1371/journal.pone.0007190

Shively, C. A., & Clarkson, T. B. (2009). The unique value of primate models in translational research. *American Journal of Primatology, 71*(9), 715-721. doi:10.1002/ajp.20720

Silva-Santos, K., Marinho, L., Santos, G., Machado, F., Gonzalez, S., Lisboa, L., & Seneda, M. (2013). Ovarian follicle reserve: emerging concepts and applications. *Animal Reproduction, 10*, 180-186.

Simpson, M. E., & Van Wagenen, G. (1973). *Postnatal development of the ovary in Homo sapiens and Macaca mulatta, and induction of ovulation in the macaque*. New Haven: New Haven, Yale University Press.

Soyal, S. M., Amleh, A., & Dean, J. (2000). FIGα, a germ cell-specific transcription factor required for ovarian follicle formation. *Development, 127*(21), 4645-4654.

Swat, M. H., Thomas, G. L., Belmonte, J. M., Shirinifard, A., Hmeljak, D., & Glazier, J. A. (2012) Multi-Scale Modeling of Tissues Using CompuCell3D. *Vol. 110. Methods in Cell Biology* (pp. 325-366).

Swat, M. H., Thomas, G. L., Shirinifard, A., Clendenon, S. G., & Glazier, J. A. (2015). Emergent Stratification in Solid Tumors Selects for Reduced Cohesion of Tumor Cells: A Multi-Cell, Virtual-Tissue Model of Tumor Evolution Using CompuCell3D. *PLoS ONE, 10*(6), e0127972. doi:10.1371/journal.pone.0127972

Szotek, P. P., Chang, H. L., Brennand, K., Fujino, A., Pieretti-Vanmarcke, R., Lo Celso, C., . . . Teixeira, J. (2008). Normal ovarian surface epithelial label-retaining cells exhibit stem/progenitor cell characteristics. *Proc Natl Acad Sci U S A, 105*. doi:10.1073/pnas.0805012105

Ting, A. Y., Xu, J., & Stouffer, R. L. (2015). Differential effects of estrogen and progesterone on development of primate secondary follicles in a steroid-depleted milieu in vitro. *Human Reproduction, 30*(8), 1907-1917. doi:10.1093/humrep/dev119

Ting, A. Y., Yeoman, R. R., Campos, J. R., Lawson, M. S., Mullen, S. F., Fahy, G. M., & Zelinski, M. B. (2013). Morphological and functional preservation of pre-antral follicles after vitrification of macaque ovarian tissue in a closed system. *Human Reproduction, 28*(5), 1267-1279.

Ting, A. Y., Yeoman, R. R., Lawson, M. S., & Zelinski, M. B. (2011). In vitro development of secondary follicles from cryopreserved rhesus macaque ovarian tissue after slow-rate freeze or vitrification. *Human reproduction (Oxford, England), 26*(9), 2461-2472. doi:10.1093/humrep/der196

Tingen, C., Kim, A., & Woodruff, T. K. (2009). The primordial pool of follicles and nest breakdown in mammalian ovaries. *Molecular Human Reproduction, 15*(12), 795-803. doi:10.1093/molehr/gap073

Trombly, D. J., Woodruff, T. K., & Mayo, K. E. (2009). Suppression of notch signaling in the neonatal mouse ovary decreases primordial follicle formation. *Endocrinology, 150*(2), 1014-1024. doi:10.1210/en.2008-0213

Trounson, A., Gosden, R., & Eichenlaub-Ritter, U. (2013). *Biology and Pathology of the Oocyte: Role in Fertility, Medicine and Nuclear Reprograming*: Cambridge University Press.

Tsuda, M., Sasaoka, Y., Kiso, M., Abe, K., Haraguchi, S., Kobayashi, S., & Saga, Y. (2003). Conserved role of nanos proteins in germ cell development. *Science, 301*(5637), 1239-1241. doi:10.1126/science.1085222

Tu, Y. K., & Gilthorpe, M. S. (2008). Univariate and Multivariate Data Analysis *Molecular Epidemiology of Chronic Diseases* (pp. 181-197).

Uda, M., Ottolenghi, C., Crisponi, L., Garcia, J. E., Deiana, M., Kimber, W., . . . Pilia, G. (2004). Foxl2 disruption causes mouse ovarian failure by pervasive blockage of follicle development. *Human Molecular Genetics, 13*(11), 1171-1181. doi:10.1093/hmg/ddh124

van den Hurk, R., & Zhao, J. (2005). Formation of mammalian oocytes and their growth, differentiation and maturation within ovarian follicles. *Theriogenology, 63*(6), 1717-1751. doi:http://dx.doi.org/10.1016/j.theriogenology.2004.08.005

Vendola, K., Zhou, J., Wang, J., Famuyiwa, O. A., Bievre, M., & Bondy, C. A. (1999). Androgens promote oocyte insulin-like growth factor I expression and initiation of follicle development in the primate ovary. *Biology of Reproduction, 61*(2), 353-357. doi:10.1095/biolreprod61.2.353

Visser, J. A., Schipper, I., Laven, J. S. E., & Themmen, A. P. N. (2012). Anti-Mullerian hormone: an ovarian reserve marker in primary ovarian insufficiency. *Nat Rev Endocrinol, 8*(6), 331-341.

Viswanathan, S. R., Daley, G. Q., & Gregory, R. I. (2008). Selective blockade of microRNA processing by Lin28. *Science, 320*(5872), 97-100. doi:10.1126/science.1154040

Wallace, W. H. B., & Kelsey, T. W. (2010). Human ovarian reserve from conception to the menopause. *PLoS ONE, 5*(1). doi:10.1371/journal.pone.0008772

Watanabe, K. H., Mayo, M., Jensen, K. M., Villeneuve, D. L., Ankley, G. T., & Perkins, E. J. (2016). Predicting fecundity of fathead minnows (Pimephales promelas) exposed to endocrine-disrupting chemicals using a MATLAB®-based model of oocyte growth dynamics. *PLoS ONE, 11*(1). doi:10.1371/journal.pone.0146594

Wear, H. M., McPike, M. J., & Watanabe, K. H. (2016). From primordial germ cells to primordial follicles: a review and visual representation of early ovarian development in mice. *Journal of Ovarian Research, 9*(1), 1-11. doi:10.1186/s13048-016-0246-7

Wei, M. C., Zong, W. X., Cheng, E. H. Y., Lindsten, T., Panoutsakopoulou, V., Ross, A. J., . . . Korsmeyer, S. J. (2001). Proapoptotic BAX and BAK: A requisite gateway to mitochondrial dysfunction and death. *Science, 292*(5517), 727-730. doi:10.1126/science.1059108

Wilhelm, D., Palmer, S., & Koopman, P. (2007). Sex determination and gonadal development in mammals. *Physiological Reviews, 87*(1), 1-28. doi:10.1152/physrev.00009.2006

Wilkosz, P., Greggains, G. D., Tanbo, T. G., & Fedorcsak, P. (2014). Female Reproductive Decline Is Determined by Remaining Ovarian Reserve and Age. *PLoS ONE, 9*(10), e108343. doi:10.1371/journal.pone.0108343

Xu, J., & Gridley, T. (2013). Notch2 is required in somatic cells for breakdown of ovarian germ-cell nests and formation of primordial follicles. *BMC Biology, 11*. doi:10.1186/1741-7007-11-13

Xu, J., Lawson, M. S., Yeoman, R. R., Molskness, T. A., Ting, A. Y., Stouffer, R. L., & Zelinski, M. B. (2013). Fibrin promotes development and function of macaque primary follicles during encapsulated three-dimensional culture. *Human Reproduction, 28*(8), 2187-2200. doi:10.1093/humrep/det093

Yeom, Y. I. I., Fuhrmann, G., Ovitt, C. E., Brehm, A., Ohbo, K., Gross, M., . . . Schöler, H. R. (1996). Germline regulatory element of Oct-4 specific for the totipotent cycle of embryonal cells. *Development, 122*(3), 881-894.

Ying, Y., Qi, X., & Zhao, G. Q. (2002). Induction of primordial germ cells from pluripotent epiblast. *TheScientificWorldJournal [electronic resource], 2*, 801-810.

Ying, Y., & Zhao, G. Q. (2001). Cooperation of endoderm-derived BMP2 and extraembryonic ectoderm-derived BMP4 in primordial germ cell generation in the mouse. *Developmental Biology, 232*(2), 484-492. doi:10.1006/dbio.2001.0173

Zhang, H., Liu, L., Li, X., Busayavalasa, K., Shen, Y., Hovatta, O., . . . Liu, K. (2014). Life-long in vivo cell-lineage tracing shows that no oogenesis originates from putative germline stem cells in adult mice. *Proceedings of the National Academy of Sciences of the United States of America, 111*(50), 17983-17988. doi:10.1073/pnas.1421047111

Zhang, H., Zheng, W., Shen, Y., Adhikari, D., Ueno, H., & Liu, K. (2012). Experimental evidence showing that no mitotically active female germline progenitors exist in postnatal mouse ovaries. *Proceedings of the National Academy of Sciences of the United States of America, 109*(31), 12580-12585. doi:10.1073/pnas.1206600109

Zheng, W., Zhang, H., Gorre, N., Risal, R., Shen, Y., & Liu, K. (2014). Two classes of ovarian primordial follicles exhibit distinct developmental dynamics and physiological functions. *Human Molecular Genetics, 23*(4), 920-928. doi:10.1093/hmg/ddt486

# APPENDICES

## Appendix A. CompuCell3D (CC3D) pre-set functions

The following are descriptions of CC3D pre-set functions used in the model of ovarian development in mice. For more information please refer to Swat et al. (M. H. Swat et al., 2012) or compucell3d.org. See chapter 3 for descriptions of customized functions (i.e. Cell Activation Steppable and Cell Abundance Tracking Steppable).

*Volume Steppable*

The volume Steppable (Equation 1) is part of the overall energy calculation in the model, contributing to the probability of pixel-copy attempts (see Equation C). Parameters defined in the volume Steppable include target volume, lambda volume, and growth; the initial volume is set in initial image file construction.

$$H_{Vol} = \sum_{\sigma} \lambda_{Vol}(\sigma)(v(\sigma) - V_t(\sigma))^2 \tag{1}$$

$H_{Vol}$ represents the volume constraint, $(\sigma)$ the cell, $\lambda_{Vol}(\sigma)$ the inverse compressibility of the cell or the density which describes the fluctuation of a cell's surface area given it's target volume, $v(\sigma)$ number of pixels in the cell, and $V_t(\sigma)$ the cell's target volume.

*Initial Contact Energy Plugin*

Contact energy (Equation 2) and cell volume are part of an overall energy calculation in the model (see Equation 3). Higher contact energy values between cell types represent a lower adhesion between those cell types and vice versa. The contact energy value must be within the same range of the volume values to prevent fragmentation and irregularities of cells in the model. Changes in contact energies throughout the simulation are controlled by the Contact Steering Steppable.

$$H_{\text{boundary}} = \sum_{\substack{\vec{i},\vec{j} \\ \text{neighbors}}} J(\tau(\sigma(\vec{i})), \tau(\sigma(\vec{j})))(1 - \delta(\sigma(\vec{i}), \sigma(\vec{j}))) \tag{2}$$

$H_{\text{boundary}}$ denotes the variation in energy due to adhesion between cell types, $J$ the boundary energy, $\tau(\sigma)$, $\tau(\sigma')$ the different cell types, and $\vec{i}, \vec{j}$ the neighboring pixels of the two cell types.

$$H_{\text{GGH}} = \sum_{\substack{\vec{i},\vec{j} \\ \text{neighbors}}} J(\tau(\sigma(\vec{i})), \tau(\sigma(\vec{j})))(1 - \delta(\sigma(\vec{i}), \sigma(\vec{j}))) + \sum_{\sigma} \lambda_{Vol}(\sigma)(v(\sigma) - V_t(\sigma))^2 \tag{3}$$

$H_{\mathrm{GGH}}$ is the Glazier-Graner-Hogeweg effective energy, which combines Equation A and B.

*Contact Steering Steppable*

The contact steering Steppable is a customized Steppable that changes contact energy values during the simulation.

*Chemotaxis Plugin*

The chemotaxis Plugin simulates the chemotaxis of cells, defining which chemical gradient is involved, which cells respond to the chemotactic field, and the lambda chemotaxis (λ). The λ is an equation coefficient that influences the energy calculation (Equation D). A higher λ will cause a greater chemotactic response.

$$\Delta E = \lambda(c(\vec{x}_{neighbor}) - c(\vec{x})) \quad (4)$$

$\Delta E$ is the energy change, $c(\vec{x})$is the current pixel chemical concentration and $c(\vec{x}_{neighbor})$ is the chemical concentration at the pixel-copy attempt location.

*Secretion Steppable*

The secretion Steppable controls the rate of secretion of a chemical field and the source of the chemical (e.g. a specific cell type, individual cell, x,y location in the simulation domain).

*Diffusion Solver Steppable*

The Diffusion Solver Steppable defines the rate constant of chemical diffusion and decay.

*Mitosis Steppable*

The Mitosis Steppable defines which cells or cell types undergo proliferation. Within the Steppable, constraints on minimum cell volumes and mitotic rates can be defined. Mitotic rates for the model were set by a random number generator, where the Mitosis Steppable would run if the random number (0-1) was less than or equal to the mitotic rate value reported in the literature.

*Cellular Death Steppable*

The Cellular Death Steppable was customized in Phase I and Phase II to control the death of PGCs and oocytes, respectively. The stoppable causes cells to "die" by increasing the lambda volume and changing the target volume to zero. Cell death in the model occurs when a cell's volume goes to zero.

## Appendix B: Code for model of early ovarian development in mice

### Phase I: python directory file

```
import sys
from os import environ
from os import getcwd
import string

sys.path.append(environ["PYTHON_MODULE_PATH"])


import CompuCellSetup
sim,simthread = CompuCellSetup.getCoreSimulationObjects()

import CompuCell

CompuCellSetup.initializeSimulationObjects(sim,simthread)

from PySteppablesExamples import SteppableRegistry
steppableRegistry=SteppableRegistry()

from MODSteppables import fileoutputSteppable
fileoutputSteppable=fileoutputSteppable(_simulator=sim,_frequency=10)
steppableRegistry.registerSteppable(fileoutputSteppable)

from MODSteppables import cellsortingSteppable
cellsortingSteppable=cellsortingSteppable(_simulator=sim,_frequency=1)
steppableRegistry.registerSteppable(cellsortingSteppable)

from MODSteppables import MitosisSteppable
mitosisSteppable=MitosisSteppable(_simulator=sim,_frequency=1)
steppableRegistry.registerSteppable(mitosisSteppable)

from MODSteppables import ContactSteeringAndTemperature
ContactSteeringAndTemperatureInstance=ContactSteeringAndTemperature(sim,_fre
steppableRegistry.registerSteppable(ContactSteeringAndTemperatureInstance)

from MODSteppables import secretionSteppable
secretionSteppable=secretionSteppable(_simulator=sim,_frequency=1)
steppableRegistry.registerSteppable(secretionSteppable)

from MODSteppables import cascadeSteppable
cascadeSteppable=cascadeSteppable(_simulator=sim,_frequency=1)
steppableRegistry.registerSteppable(cascadeSteppable)

from MODSteppables import VolumeParamSteppable
VolumeParamSteppable=VolumeParamSteppable(_simulator=sim,_frequency=1)
steppableRegistry.registerSteppable(VolumeParamSteppable)
```

## Phase I: python directory file

```
46
47 CompuCellSetup.mainLoop(sim,simthread,steppableRegistry)
```

## Phase I: python steppables file

```
from PySteppables import *
from PySteppablesExamples import MitosisSteppableBase
import CompuCell
import sys
import random
import math


class fileoutputSteppable(SteppableBasePy):
    def __init__(self,_simulator,_frequency):
         SteppableBasePy.__init__(self,_simulator,_frequency)
    def step(self,mcs):
        PGCcount=0
        for cell in self.cellListByType(1):
            PGCcount = PGCcount + 1
        fileName='MODI_SA_output_secretion_sdf1.txt'
        try:
            fileHandle,fullFileName\
            =self.openFileInSimulationOutputDirectory(fileName,"a")
        except IOError:
            print "Could not open file ", fileName," for writing. "
            return
        print >>fileHandle,mcs  ,PGCcount
        fileHandle.close()


class cellsortingSteppable(SteppableBasePy):
    def __init__(self,_simulator,_frequency): SteppableBasePy.__init__(self,
    def start(self):
        pass
    def step(self,mcs):
        PGCcount = 0
        for cell in self.cellListByType(1):
            PGCcount = PGCcount + 1
        ECMcount = 0
        for cell in self.cellListByType(4):
            ECMcount = ECMcount + 1
        signalon_count = 0
        for cell in self.cellListByType(2):
            signalon_count = signalon_count + 1
        print "PGC count =",PGCcount
        print "ECM count =",ECMcount
        print "signalon count =",signalon_count
        print "Monte carlo steps =",mcs

```

## Phase I: python steppables file

```
46
47 class MitosisSteppable(MitosisSteppableBase):
48     def __init__(self,_simulator,_frequency): Need to calculate frequency
49         MitosisSteppableBase.__init__(self,_simulator, _frequency)
50         self.setParentChildPositionFlag(-1)
51     def step(self,mcs):
52         cells_to_divide=[]
53         if 3600 > mcs > 300:
54             for cell in self.cellListByType(1):
55                 if 1800 > mcs > 300:
56                     if cell.volume > 10:
57                         if random.random() < 0.0025:
58                             cells_to_divide.append(cell)
59                 if 3600> mcs >1800:
60                     if cell.volume > 10:
61                         if random.random() < 0.0025:
62                             cells_to_divide.append(cell)
63         for cell in cells_to_divide:
64             self.divideCellRandomOrientation(cell)
65         if mcs > 3600:
66             frequency = 500000
67     def updateAttributes(self):
68         parentCell=self.mitosisSteppable.parentCell
69         childCell=self.mitosisSteppable.childCell
70         childCell.targetVolume=parentCell.targetVolume
71         childCell.lambdaVolume=parentCell.lambdaVolume
72         if parentCell.type==1:
73             childCell.type=1
74
75
76 class ContactSteeringAndTemperature(SteppableBasePy):
77     def __init__(self,_simulator,_frequency):
78         SteppableBasePy.__init__(self,_simulator,_frequency)
79     def step(self,mcs):
80         if mcs == 1800:
81             for cell in self.cellList:
82                 val1=float(self.getXMLElementValue(['Plugin','Name','Contact
83                 self.setXMLElementValue(val1+5,['Plugin','Name','Contact'],[
84                 self.updateXML()
85                 return
86
87
88 class secretionSteppable(SecretionBasePy):
89     def __init__(self,_simulator,_frequency):
90         SecretionBasePy.__init__(self,_simulator,_frequency)
```

## Phase I: python steppables file

```
    def start(self):
        pass
    def step(self,mcs):
        # Get the ckit field
        ckitfield=self.getConcentrationField('ckit')
        SDF1field=self.getConcentrationField('SDF1')
        ckitSecretor=self.getFieldSecretor('ckit')
        SDF1Secretor=self.getFieldSecretor('SDF1')
        if mcs > 1500:
            for cell in self.cellListByType(2):
                ckitSecretor.secreteOutsideCellAtBoundary(cell,0.5)
            for cell in self.cellListByType(6):
                SDF1Secretor.secreteOutsideCellAtBoundary(cell,2.0)
            else:
                ckitSecretor.secreteOutsideCellAtBoundary(cell,0)
                SDF1Secretor.secreteOutsideCellAtBoundary(cell,0)


class cascadeSteppable(SteppableBasePy):
     def __init__(self,_simulator,_frequency):
         SteppableBasePy.__init__(self,_simulator,_frequency)
     def step(self,mcs):
        ckitfield=self.getConcentrationField('ckit')
        ckitSecretor=self.getFieldSecretor('ckit')
        if mcs > 1500:
            for cell in self.cellListByType(7):
                if ckitfield[int(cell.xCOM),int(cell.yCOM),int(cell.zCOM)]>0
                    cell.type = 2
                    ckitfield[int(cell.xCOM),int(cell.yCOM),int(cell.zCOM)]=


class VolumeParamSteppable(SteppableBasePy):
    def __init__(self,_simulator,_frequency):
        SteppableBasePy.__init__(self,_simulator,_frequency)
    def start(self):
        for cell in self.cellList:
            #Medium Volume
            if cell.type==0:
                cell.targetVolume=16
                cell.lambdaVolume=5
            #PGC Volume
            if cell.type==1:
                cell.targetVolume=16.5
                cell.lambdaVolume=5
            # Signalon Volume
```

## Phase I: python steppables file

```
            elif (cell.type==2):
                cell.targetVolume=16
                cell.lambdaVolume=5
            #Hindgut Volume
            elif (cell.type==3):
                cell.targetVolume=16
                cell.lambdaVolume=5
            #ECM Volume
            elif (cell.type==4):
                cell.targetVolume=16
                cell.lambdaVolume=5
            #Yolk Volume
            elif (cell.type==5):
                cell.targetVolume=16
                cell.lambdaVolume=5
            #GR Volume
            elif (cell.type==6):
                cell.targetVolume=16
                cell.lambdaVolume=5
            #Signaloff Volume
            elif (cell.type==7):
                cell.targetVolume=16
                cell.lambdaVolume=5
    def step(self,mcs):
        if 1800 > mcs > 300:
            for cell in self.cellListByType(1):
                if cell.volume < 16.5:
                    cell.targetVolume+=0.012
            else:
                cell.targetVolume+=0.001


class DeathSteppable(SteppableBasePy):
    def __init__(self,_simulator,_frequency):
        SteppableBasePy.__init__(self,_simulator,_frequency)
    def start(self):
        self.initialNumberOfCells = len(self.cellList)
    def step(self,mcs):
        SDF1field=self.getConcentrationField('SDF1')
        if mcs > 3600:
            for cell in self.cellListByType(1):
                if SDF1field[int(cell.xCOM),int(cell.yCOM),int(cell.zCOM)] <
                    cell.targetVolume=0
                    cell.lambdaVolume=20
```

## Phase I: XML file

```
<CompuCell3D Revision="20140926" Version="3.7.3">

   <Potts>
     <Dimensions x="320" y="320" z="1"/>
      <Steps>4201</Steps>
      <FluctuationAmplitude>25.0</FluctuationAmplitude>
      <Flip2DimRatio>1.0</Flip2DimRatio>
      <NeighborOrder>2</NeighborOrder>
   </Potts>

   <Plugin Name="PlayerSettings">
      <VisualControl ScreenshotFrequency="150"  ClosePlayerAfterSimulationDo
   </Plugin>

   <Plugin Name="CellType">
      <CellType TypeId="0" TypeName="Medium"/>
      <CellType TypeId="1" TypeName="PGC"/>
      <CellType Freeze="" TypeId="2" TypeName="signalon"/>
      <CellType Freeze="" TypeId="3" TypeName="hindgut"/>
      <CellType TypeId="4" TypeName="ECM"/>
      <CellType Freeze="" TypeId="5" TypeName="yolk"/>
      <CellType TypeId="6" TypeName="GR"/>
      <CellType Freeze="" TypeId="7" TypeName="signaloff"/>
   </Plugin>

   <Plugin Name="Volume">
   </Plugin>

   <Plugin Name="CenterOfMass"></Plugin>
   <Plugin Name="NeighborTracker"></Plugin>
   <Plugin Name="PixelTracker"></Plugin>
   <Plugin Name="BoundaryPixelTracker"><NeighborOrder>1</NeighborOrder></Plu

   <Plugin Name="Contact">
      <Energy Type1="Medium" Type2="Medium">24.0</Energy>
      <Energy Type1="Medium" Type2="PGC">27.0</Energy>
      <Energy Type1="Medium" Type2="ECM">24.0</Energy>
      <Energy Type1="Medium" Type2="hindgut">27.00</Energy>
      <Energy Type1="Medium" Type2="signalon">27.00</Energy>
      <Energy Type1="Medium" Type2="signaloff">27.00</Energy>
      <Energy Type1="Medium" Type2="yolk">24.00</Energy>
      <Energy Type1="Medium" Type2="GR">27.00</Energy>
      <Energy Type1="PGC" Type2="PGC">16.0</Energy>
      <Energy Type1="PGC" Type2="ECM">27.00</Energy>
      <Energy Type1="PGC" Type2="hindgut">20.0</Energy>
```

## Phase I: XML file

```
46      <Energy Type1="PGC" Type2="signalon">27.00</Energy>
47      <Energy Type1="PGC" Type2="signaloff">27.00</Energy>
48      <Energy Type1="PGC" Type2="yolk">28.0</Energy>
49      <Energy Type1="PGC" Type2="GR">33.00</Energy>
50      <Energy Type1="ECM" Type2="ECM">24.00</Energy>
51      <Energy Type1="ECM" Type2="hindgut">27.00</Energy>
52      <Energy Type1="ECM" Type2="signalon">27.00</Energy>
53      <Energy Type1="ECM" Type2="signaloff">27.00</Energy>
54      <Energy Type1="ECM" Type2="GR">27.00</Energy>
55      <Energy Type1="ECM" Type2="yolk">24.00</Energy>
56      <Energy Type1="hindgut" Type2="hindgut">16.0</Energy>
57      <Energy Type1="hindgut" Type2="signalon">16.0</Energy>
58      <Energy Type1="hindgut" Type2="signaloff">16.0</Energy>
59      <Energy Type1="hindgut" Type2="yolk">16.00</Energy>
60      <Energy Type1="hindgut" Type2="GR">24.00</Energy>
61      <Energy Type1="signalon" Type2="signalon">16.00</Energy>
62      <Energy Type1="signalon" Type2="signaloff">16.00</Energy>
63      <Energy Type1="signalon" Type2="yolk">24.00</Energy>
64      <Energy Type1="signalon" Type2="GR">36.00</Energy>
65      <Energy Type1="yolk" Type2="yolk">24.00</Energy>
66      <Energy Type1="yolk" Type2="signaloff">24.00</Energy>
67      <Energy Type1="yolk" Type2="GR">24.00</Energy>
68      <Energy Type1="GR" Type2="GR">8.00</Energy>
69      <Energy Type1="GR" Type2="signaloff">36.00</Energy>
70      <Energy Type1="signaloff" Type2="signaloff">18.00</Energy>
71      <NeighborOrder>2</NeighborOrder>
72   </Plugin>
73
74
75   <Plugin Name="Chemotaxis">
76      <ChemicalField Name="ckit" Source="DiffusionSolverFE">
77         <ChemotaxisByType Lambda="10" Type="PGC"/>
78      </ChemicalField>
79      <ChemicalField Name="SDF1" Source="DiffusionSolverFE">
80         <ChemotaxisByType Lambda="30" Type="PGC"/>
81      </ChemicalField>
82   </Plugin>
83
84    <Plugin Name="Secretion">
85        <Field Name="ckit"></Field>
86        <Field Name="SDF1"></Field>
87    </Plugin>
88
89   <Steppable Type="DiffusionSolverFE">
90      <DiffusionField Name="ckit">
```

## Phase I: XML file

```
91          <DiffusionData>
92             <FieldName>ckit</FieldName>
93             <GlobalDiffusionConstant>0.3</GlobalDiffusionConstant>
94             <GlobalDecayConstant>.001</GlobalDecayConstant>
95          </DiffusionData>
96       </DiffusionField>
97        <DiffusionField Name="SDF1">
98          <DiffusionData>
99             <FieldName>SDF1</FieldName>
100            <GlobalDiffusionConstant>0.99</GlobalDiffusionConstant>
101            <GlobalDecayConstant>0.00001</GlobalDecayConstant>
102         </DiffusionData>
103      </DiffusionField>
104   </Steppable>
105
106
107   <Steppable Type="PIFInitializer">
108      <PIFName>Simulation/MODI_Feb24.piff</PIFName>
109   </Steppable>
110</CompuCell3D>
111
```

## Phase II: python steppables file

```
from PySteppables import *
import CompuCell
import sys
import random
from array import *
from PySteppablesExamples import MitosisSteppableBase

class fileoutputSteppable(SteppableBasePy):
    def __init__(self,_simulator,_frequency):
         SteppableBasePy.__init__(self,_simulator,_frequency)
    def step(self,mcs):
        PGCcount=0
        for cell in self.cellListByType(1):
            PGCcount = PGCcount + 1
        fileName='MODII_SA_output.csv'
        try:
            fileHandle,fullFileName\
            =self.openFileInSimulationOutputDirectory(fileName,"a")
        except IOError:
            print "Could not open file ", fileName," for writing. "
            return
        print >>fileHandle,mcs  ,PGCcount
        fileHandle.close()


class cellsortingSteppable(SteppableBasePy):
    def __init__(self,_simulator,_frequency=1): SteppableBasePy.__init__(sel
    def start(self):
        pass
    def step(self,mcs):
        OocyteCount = 0
        for cell in self.cellListByType(1):
            OocyteCount = OocyteCount + 1
        print "oocyte count =",OocyteCount
        print "Monte carlo steps =",mcs


class VolumeParamSteppable(SteppableBasePy):
    def __init__(self,_simulator,_frequency):
        SteppableBasePy.__init__(self,_simulator,_frequency)
    def start(self):
        for cell in self.cellList:
            #Oocyte Volume
            if cell.type==1:
                cell.targetVolume=22
```

## Phase II: python directory file

```
                cell.lambdaVolume=4.0
            # Granulosa Volume
            elif (cell.type==2):
                cell.targetVolume=21
                cell.lambdaVolume=3.0
            #Stromal Volume
            elif (cell.type==3):
                cell.targetVolume=21
                cell.lambdaVolume=3.0
            #Epithelial Volume
            elif (cell.type==4):
                cell.targetVolume=15
                cell.lambdaVolume=3.0
            #Mesonephros Volume
            elif (cell.type==5):
                cell.targetVolume=16
                cell.lambdaVolume=3.0
    def step(self,mcs):
        if 4800 > mcs > 3600:
            for cell in self.cellListByType(1):
                cell.targetVolume+=0.001


class ContactSteeringAndTemperature(SteppableBasePy): #set current value opp
    def __init__(self,_simulator,_frequency):
        SteppableBasePy.__init__(self,_simulator,_frequency)
    def step(self,mcs):
        field=self.getConcentrationField('estrogen')
        if mcs == 3600:
            for cell in self.cellListByType(5):
                if field[int(cell.xCOM),int(cell.yCOM),int(cell.zCOM)]<0.1:
                    val1=float(self.getXMLElementValue(['Plugin','Name','Con
                    self.setXMLElementValue(val1-4,['Plugin','Name','Contact
                    val2=float(self.getXMLElementValue(['Plugin','Name','Con
                    self.setXMLElementValue(val2+15,['Plugin','Name','Contac
                    self.updateXML()
                    return


class secretionSteppable(SecretionBasePy):
    def __init__(self,_simulator,_frequency):
        SecretionBasePy.__init__(self,_simulator,_frequency)
    def start(self):
        field=self.getConcentrationField('estrogen')
        for cell in self.cellList:
```

## Phase II: python steppables file

```
from PySteppables import *
import CompuCell
import sys
import random
from array import *
from PySteppablesExamples import MitosisSteppableBase

class fileoutputSteppable(SteppableBasePy):
    def __init__(self,_simulator,_frequency):
         SteppableBasePy.__init__(self,_simulator,_frequency)
    def step(self,mcs):
        PGCcount=0
        for cell in self.cellListByType(1):
            PGCcount = PGCcount + 1
        fileName='MODII_SA_output.csv'
        try:
            fileHandle,fullFileName\
            =self.openFileInSimulationOutputDirectory(fileName,"a")
        except IOError:
            print "Could not open file ", fileName," for writing. "
            return
        print >>fileHandle,mcs  ,PGCcount
        fileHandle.close()


class cellsortingSteppable(SteppableBasePy):
    def __init__(self,_simulator,_frequency=1): SteppableBasePy.__init__(sel
    def start(self):
        pass
    def step(self,mcs):
        OocyteCount = 0
        for cell in self.cellListByType(1):
            OocyteCount = OocyteCount + 1
        print "oocyte count =",OocyteCount
        print "Monte carlo steps =",mcs


class VolumeParamSteppable(SteppableBasePy):
    def __init__(self,_simulator,_frequency):
        SteppableBasePy.__init__(self,_simulator,_frequency)
    def start(self):
        for cell in self.cellList:
            #Oocyte Volume
            if cell.type==1:
                cell.targetVolume=22
```

## Phase II: python directory file

```
                cell.lambdaVolume=4.0
            # Granulosa Volume
            elif (cell.type==2):
                cell.targetVolume=21
                cell.lambdaVolume=3.0
            #Stromal Volume
            elif (cell.type==3):
                cell.targetVolume=21
                cell.lambdaVolume=3.0
            #Epithelial Volume
            elif (cell.type==4):
                cell.targetVolume=15
                cell.lambdaVolume=3.0
            #Mesonephros Volume
            elif (cell.type==5):
                cell.targetVolume=16
                cell.lambdaVolume=3.0
    def step(self,mcs):
        if 4800 > mcs > 3600:
            for cell in self.cellListByType(1):
                cell.targetVolume+=0.001


class ContactSteeringAndTemperature(SteppableBasePy): #set current value opp
    def __init__(self,_simulator,_frequency):
        SteppableBasePy.__init__(self,_simulator,_frequency)
    def step(self,mcs):
        field=self.getConcentrationField('estrogen')
        if mcs == 3600:
            for cell in self.cellListByType(5):
                if field[int(cell.xCOM),int(cell.yCOM),int(cell.zCOM)]<0.1:
                    val1=float(self.getXMLElementValue(['Plugin','Name','Con
                    self.setXMLElementValue(val1-4,['Plugin','Name','Contact
                    val2=float(self.getXMLElementValue(['Plugin','Name','Con
                    self.setXMLElementValue(val2+15,['Plugin','Name','Contac
                    self.updateXML()
                    return


class secretionSteppable(SecretionBasePy):
    def __init__(self,_simulator,_frequency):
        SecretionBasePy.__init__(self,_simulator,_frequency)
    def start(self):
        field=self.getConcentrationField('estrogen')
        for cell in self.cellList:
```

## Phase II: python directory file

```
            field[int(cell.xCOM),int(cell.yCOM),int(cell.zCOM)] = 1
            for x,y,z in self. everyPixel():
                field[x,y,z]=1
                return
    def step(self,mcs):
        field=self.getConcentrationField('estrogen')
        signalSecretor=self.getFieldSecretor('estrogen')
        if 3600 > mcs > 0:
            for cell in self.cellList:
                if cell.type == 5:
                    signalSecretor.secreteOutsideCellAtBoundary(cell,0.1)
        if mcs > 3600:
            for cell in self.cellList:
                if cell.type == 5:
                    signalSecretor.secreteOutsideCellAtBoundary(cell,0)
            for cell in self.cellList:
                if field[int(cell.xCOM),int(cell.yCOM),int(cell.zCOM)]>0:
                    field[int(cell.xCOM),int(cell.yCOM),int(cell.zCOM)]=0
                    for x,y,z in self.everyPixel():
                        field[x,y,z]=0


class MitosisSteppable(MitosisSteppableBase):
    def __init__(self,_simulator,_frequency):
        MitosisSteppableBase.__init__(self,_simulator,_frequency)
    def step(self,mcs):
        cells_to_divide_oocytes=[]
        cells_to_divide_granulosa=[]
        cells_to_divide_stromal=[]
        cells_to_divide_epithelial=[]
        for cell in self.cellList:
            if cell.type == 1: #Oocytes
                cells_to_divide_oocytes.append(cell)
            if cell.type == 2: #pre-granulosa (somatic) cells
                cells_to_divide_granulosa.append(cell)
            if cell.type == 3: #pre-stromal (somatic) cells
                cells_to_divide_stromal.append(cell)
            if cell.type == 4: #epithelial (somatic) cells
                cells_to_divide_epithelial.append(cell)
        #Granulosa cells
        if random.random() < 0.0001:
            for cell in cells_to_divide_granulosa:
                self.divideCellRandomOrientation(cell)
        #Stromal cells
        if random.random() < 0.00005:
```

## Phase II: python directory file

```
            for cell in cells_to_divide_stromal:
                self.divideCellRandomOrientation(cell)
        #Epithelial cells
        if random.random() < 0.000005:
            for cell in cells_to_divide_epithelial:
                self.divideCellRandomOrientation(cell)
        #Oocytes
        for cell in self.cellListByType(1):
            if mcs < 1300:
            if cell.volume > 15:
                    if random.random() < 0.0018333:
                        self.divideCellRandomOrientation(cell)
    def updateAttributes(self):
        parentCell=self.mitosisSteppable.parentCell
        childCell=self.mitosisSteppable.childCell
        childCell.targetVolume=parentCell.targetVolume
        childCell.lambdaVolume=parentCell.lambdaVolume
        if parentCell.type==1:
            childCell.type=1
        if parentCell.type==2:
            childCell.type=2
        if parentCell.type==3:
            childCell.type=3
        if parentCell.type==4:
            childCell.type=4


class DeathSteppable(SteppableBasePy):
    def __init__(self,_simulator,_frequency):
        SteppableBasePy.__init__(self,_simulator,_frequency)
    def start(self):
        self.initialNumberOfCells = len(self.cellList)
        print "\n\nNumber of cells: %s\n\n" % self.initialNumberOfCells
    def step(self,mcs):
        rv=random.random()
        if 4800 > mcs > 1300:
            for cell in self.cellListByType(1):
                cluster=[]
                for neighbor , commonSurfaceArea in self.getCellNeighborData
                    NT = cell.type
                    cluster.append(NT)
                for NT in cluster:
                    if all(NT != 1 for NT in cluster):
                        if rv < 0.8:
                            if cell.volume > 0:
```

## Phase II: python directory file

```
181                                 cell.targetVolume=0
182                                 cell.lambdaVolume=1
183
```

## Phase II: XML file

```
<CompuCell3D Revision="20140926" Version="3.7.3">

   <Potts>
      <Dimensions x="320" y="335" z="1"/>
      <Steps>4801</Steps>
      <Temperature>25.0</Temperature>
      <NeighborOrder>2</NeighborOrder>
   </Potts>

   <Plugin Name="PlayerSettings">
      <VisualControl ScreenshotFrequency="150"/>
   </Plugin>

   <Plugin Name="CellType">
      <CellType TypeId="0" TypeName="Medium"/>
      <CellType TypeId="1" TypeName="oocyte"/>
      <CellType TypeId="2" TypeName="granulosa"/>
      <CellType TypeId="3" TypeName="stromal"/>
      <CellType TypeId="4" TypeName="epithelial"/>
      <CellType TypeId="5" TypeName="mesonephros"/>
   </Plugin>

   <Plugin Name="Surface"></Plugin>

   <Plugin Name="Volume"></Plugin>

   <Plugin Name="CenterOfMass"></Plugin>

    <Plugin Name="NeighborTracker"></Plugin>

      <Plugin Name="Contact">
      <Energy Type1="Medium" Type2="Medium">37.5</Energy>
      <Energy Type1="Medium" Type2="oocyte">37.5</Energy>
      <Energy Type1="Medium" Type2="granulosa">37.5</Energy>
      <Energy Type1="Medium" Type2="stromal">37.5</Energy>
      <Energy Type1="Medium" Type2="epithelial">17.5</Energy>
      <Energy Type1="Medium" Type2="mesonephros">19.5</Energy>
      <Energy Type1="oocyte" Type2="oocyte">16.0</Energy>
      <Energy Type1="oocyte" Type2="granulosa">19.5</Energy>
      <Energy Type1="oocyte" Type2="stromal">21.0</Energy>
      <Energy Type1="oocyte" Type2="epithelial">42.0</Energy>
      <Energy Type1="oocyte" Type2="mesonephros">52.5</Energy>
      <Energy Type1="granulosa" Type2="granulosa">19.5</Energy>
      <Energy Type1="granulosa" Type2="stromal">19.5</Energy>
      <Energy Type1="granulosa" Type2="epithelial">27.0</Energy>
```

## Phase II: XML file

```
      <Energy Type1="granulosa" Type2="mesonephros">52.5</Energy>
      <Energy Type1="stromal" Type2="stromal">19.5</Energy>
      <Energy Type1="stromal" Type2="epithelial">27.0</Energy>
      <Energy Type1="stromal" Type2="mesonephros">52.5</Energy>
      <Energy Type1="epithelial" Type2="epithelial">13.5</Energy>
      <Energy Type1="epithelial" Type2="mesonephros">22.5</Energy>
      <Energy Type1="mesonephros" Type2="mesonephros">19.5</Energy>
      <NeighborOrder>2</NeighborOrder>
   </Plugin>

   <Plugin Name="Secretion">
       <Field Name="estrogen"></Field>
   </Plugin>


   <Steppable Type="FlexibleDiffusionSolverFE">
      <DiffusionField Name="estrogen">
         <DiffusionData>
            <FieldName>estrogen</FieldName>
            <DiffusionConstant>0.2</DiffusionConstant>
            <DecayConstant>0.01</DecayConstant>
         </DiffusionData>
      </DiffusionField>
   </Steppable>


   <Steppable Type="PIFInitializer">
      <PIFName>Simulation/MODII_Apr20.piff</PIFName>
   </Steppable>
</CompuCell3D>

```

## TABLES

**Table 3.1.** Cell types important to ovarian development in Phase I and Phase II of the model. Symbols and roles of cell types in early ovarian development are noted.

| Cell type symbol | Cell type name | Role in early ovarian development |
|---|---|---|
| ***Phase I*** | | |
| $\tau_1$ | Primordial germ cell (PGC) | Origin to oocytes |
| $\tau_2$ | Gonadal ridge | Develops into the gonad, becoming the ovary or testis; secrete chemoattractant ligand SDF1; migration destination |
| $\tau_3$ | KIT signaling cells | Surface hindgut cells that secrete chemoattractant ligand, KIT |
| $\tau_4$ | Hindgut | Tissue that PGCs move along when migrating to the gonadal ridge |
| $\tau_5$ | Embryonic tissue | All other tissues of the embryo (not included extraembryonic) |
| $\tau_6$ | Extraembryonic tissue | Extraembryonic tissue in the mouse embryo; for visual representation of embryo structure |
| ***Phase II*** | | |
| $\tau'_1$ | Oocyte | Female germ cell |
| $\tau'_2$ | Granulosa | Supporting follicular cell to oocyte maturation |
| $\tau'_3$ | Stromal | Internal cell in ovary |
| $\tau'_4$ | Epithelial | Outer cell layer of ovary |
| $\tau'_5$ | Mesonephros | Tissue supplying nutrients to the gonad during development |

**Table 3.2.** Symbol, descriptions, values, and references for model parameters in Phase I, organized by biological category.

| Biological category | CC3D Function | Parameter Symbol | Parameter Description | Value | Reference |
|---|---|---|---|---|---|
| Cell Size | Volume Steppable | $V_{\tau 1}$ | PGC target volume | 16.5 pixels | Ginsburg et al 1990 |
| | | $\lambda_{V\tau 1}$ | PGC lambda volume | 5.0 | Fitted |
| | | $V_{\tau 2}$ | Gonadal ridge target volume | 16.0 pixels | Ginsburg et al 1990 |
| | | $\lambda_{V\tau 2}$ | Gonadal ridge lambda volume | 5,0 | Fitted |
| | | $V_{\tau 3}$ | KIT signaling cell target volume | 16.0 pixels | Ginsburg et al 1990 |
| | | $\lambda_{V\tau 3}$ | KIT signaling cell lambda volume | 5.0 | Fitted |
| | | $V_{\tau 4}$ | Hindgut target volume | 16.0 pixels | Ginsburg et al 1990 |
| | | $\lambda_{V4}$ | Hindgut lambda Volume | 5.0 | Fitted |
| | | $V_{\tau 5}$ | Embryonic tissue target volume | 16.0 pixels | Ginsburg et al 1990 |
| | | $\lambda_{V\tau 5}$ | Embryonic tissue lambda volume | 5.0 | Fitted |
| | | $V_{\tau 6}$ | Yolk target volume | 16.0 pixels | Ginsburg et al 1990 |
| | | $\lambda_{V6}$ | Yolk lambda volume | 5.0 | Fitted |
| | | $g_{\tau 1}$ | PGC growth | 0.012 pixels $MCS^{-1}$ | Fitted |
| | | $g_{cell}$ | Cellular growth (not including PGC type) | 0.001 pixels $MCS^{-1}$ | Fitted |
| Cell Abundance | Mitosis Steppable | $m_{\tau 1}$ | Mitosis of PGCs (300-1200 MCS) | 0.0025 $MCS^{-1}$ | De Sousa Lopes et al 2007 |
| | | $m_{\tau 1}$ | Mitosis of PGCs (1200-3600 MCS) | 0.0025 $MCS^{-1}$ | De Sousa Lopes et al 2007 |
| | Cell Death Steppable | $d_{\tau 1}$ | Death of PGCs | All <400 μM SDF1 | Fitted |
| | | $\lambda_{d\tau 1}$ | Lambda death of PGCs | 20 | Fitted |
| Chemotaxis | Chemotaxis Plugin | $\lambda_{KIT(\tau 1)}$ | PGC chemotaxis lambda for c-kit | 10.0 | Fitted |
| | | $\lambda_{SDF1(\tau 1)}$ | PGC chemotaxis lambda for SDF1 | 30.0 | Fitted |

| | | | | | |
|---|---|---|---|---|---|
| | Diffusion Solver Steppable | $D_{KIT}$ | KIT Chemoattractant Diffusion Constant | 0.3 pixels $MCS^{-1}$ | Fitted |
| | | $k_{KIT}$ | KIT chemoattractant decay constant | 0.001 pixels $MCS^{-1}$ | Fitted |
| | | $D_{SDF1}$ | SDF1 chemoattractant diffusion constant | 0.99 pixels $MCS^{-1}$ | Fitted |
| | | $k_{SDF1}$ | SDF1 chemoattractant decay constant | 0.00001 pixels $MCS^{-1}$ | Fitted |
| | Secretion Steppable | $\Theta_{KIT}$ | KIT chemoattractant secretion constant | 0.5 μM $MCS^{-1}$ | Fitted |
| | | $\Theta_{SDF1}$ | SDF1 chemoattractant secretion constant | 2.0 μM $MCS^{-1}$ | Fitted |

**Table 3.3.** Symbol, descriptions, values, and references for model parameters in Phase II, organized by biological category.

| Biological Category | CC3D Functions | Parameter Symbol | Parameter Description | Value | Reference |
|---|---|---|---|---|---|
| Cell size | Volume Steppable | $V_{\tau'1}$ | Oocyte target volume | 22.0 pixels | Manuylov et al 2008 |
| | | $\lambda_{V\tau'1}$ | Oocyte lambda volume | 4.0 | Fitted |
| | | $V_{\tau'2}$ | Granulosa target volume | 21.0 pixels | Manuylov et al 2008 |
| | | $\lambda_{V\tau'2}$ | Granulosa cells on lambda volume | 3.0 | Fitted |
| | | $V_{\tau'3}$ | Stromal target volume | 21.0 pixels | Manuylov et al 2008 |
| | | $\lambda_{V\tau'3}$ | Stromal lambda volume | 3.0 | Fitted |
| | | $V_{\tau'4}$ | Epithelial target volume | 15.0 pixels | Manuylov et al 2008 |
| | | $\lambda_{V\tau'4}$ | Epithelial lambda volume | 3.0 | Fitted |
| | | $V_{\tau'5}$ | Mesonephros target volume | 15.0 pixels | Manuylov et al 2008 |
| | | $\lambda_{V\tau'5}$ | Mesonephros lambda volume | 3.0 | Fitted |
| Cell abundance | Mitosis Steppable | $m_{\tau'1}$ | Mitosis of oocytes | 0.0018333 $MCS^{-1}$ | Lei and Spradling 2013 |
| | | $m_{\tau'2}$ | Mitosis of granulosa cells | 0.0001 $MCS^{-1}$ | Fitted |
| | | $m_{\tau'3}$ | Mitosis of stromal cells | 0.00005 $MCS^{-1}$ | Fitted |
| | | $m_{\tau'4}$ | Mitosis of epithelial cells | 0.000005 $MCS^{-1}$ | Fitted |
| | Cell Death Steppable | $d_{\tau'1}$ | Death (apoptosis) of oocytes | 0.13 oocytes $MCS^{-1}$ | Lei and Spradling 2013 |
| | | $\lambda_{d\tau'1}$ | Lambda death rate of oocytes | 550000000 | Fitted |
| Maternal estrogen | Secretion Steppable | $\Theta_{estrogen}$ | Secretion of estrogen | 0.1 μM $MCS^{-1}$ | Fitted |
| | *Diffusion Solver Steppable* | $D_{estrogen}$ | Estrogen diffusion constant | 0.99 pixels $MCS^{-1}$ | Fitted |
| | | $k_{estrogen}$ | SDF1 chemoattractant decay constant | 0.00001 pixels $MCS^{-1}$ | Fitted |

**Table 3.4.** Contact energy ($J_{\tau\text{-}\tau}$) between cell types in Phase I.

| | $J_{\tau 0}$ | $J_{\tau 1}$ | $J_{\tau 2}$ | $J_{\tau 3}$ | $J_{\tau 4}$ | $J_{\tau 5}$ | $J_{\tau 6}$ | $J_{\tau 7}$ |
|---|---|---|---|---|---|---|---|---|
| $J_{\tau 0}$ | 24.0 | 27.0 | 27.0 | 27.0 | 24.0 | 24.0 | 27.0 | 27.0 |
| $J_{\tau 1}$ | | 16.0 | 27.0 | 20.0 | 27.0 | 28.0 | 33.0 | 27.0 |
| $J_{\tau 2}$ | | | 24.0 | 16.0 | 27.0 | 24.0 | 36.0 | 24.0 |
| $J_{\tau 3}$ | | | | 16.0 | 27.0 | 24.0 | 36.0 | 16.0 |
| $J_{\tau 4}$ | | | | | 24.0 | 24.0 | 27.0 | 27.0 |
| $J_{\tau 5}$ | | | | | | 24.0 | 24.0 | 24.0 |
| $J_{\tau 6}$ | | | | | | | 8.0 | 36.0 |
| $J_{\tau 7}$ | | | | | | | | 18.0 |

**Table 3.5.** Contact energy ($J_{\tau'\text{-}\tau'}$) between cell types in Phase II.

| | $J_{\tau' 0}$ | $J_{\tau' 1}$ | $J_{\tau' 2}$ | $J_{\tau' 3}$ | $J_{\tau' 4}$ | $J_{\tau' 5}$ |
|---|---|---|---|---|---|---|
| $J_{\tau' 0}$ | 37.5 | 37.5 | 37.5 | 37.5 | 17.5 | 19.5 |
| $J_{\tau' 1}$ | | 16.0 | 19.5 | 21.0 | 42.0 | 52.5 |
| $J_{\tau' 2}$ | | | 19.5 | 19.5 | 27.0 | 52.5 |
| $J_{\tau' 3}$ | | | | 19.5 | 27.0 | 52.5 |
| $J_{\tau' 4}$ | | | | | 13.5 | 22.5 |
| $J_{\tau' 5}$ | | | | | | 19.5 |

**Table 4.1.** Assessment of parameters based on developmental process accuracy and cell structure integrity in univariate sensitivity analysis for Phase I. A checkmark (✓ ) indicates the parameter showed sensitivity and a line (--) indicates the parameter did not show sensitivity when adjusted ±10%.

| Parameter | Developmental Process | Cell Structure |
|---|---|---|
| $J_{\tau\text{-}\tau}$ | ✓ | ✓ |
| $m_{\tau 1}$ | ✓ | ✓ |
| $\lambda_{SDF1\ (\tau 1)}$ | ✓ | ✓ |
| $\lambda_{KIT\ (\tau 1)}$ | ✓ | ✓ |
| $D_{KIT}$ | ✓ | ✓ |
| $D_{SDF1}$ | ✓ | ✓ |
| $g_{\tau 1}$ | -- | ✓ |
| $\Theta_{SDF1}$ | ✓ | ✓ |
| $\Theta_{KIT}$ | ✓ | -- |
| $V_{\tau\ all}$ | -- | ✓ |
| $\lambda_{V\ \tau}$ | -- | -- |
| $k_{KIT}$ | -- | -- |
| $k_{SDF1}$ | -- | -- |

**Table 4.2.** Rankings of parameters in Phase I and Phase II of the model, based on evaluation of sensitivity analysis endpoints: developmental process accuracy, cell structure integrity, germ cell abundance, and for Phase I only the number of incomplete trials.

| Parameter | Sensitivity Ranking |
|---|---|
| *Phase I* | |
| $J_{\tau\text{-}\tau}$ | High |
| $m_{\tau 1}$ | High |
| $\lambda_{KIT(\tau 1)}$ | High |
| $D_{SDF1}$ | High |
| $D_{KIT}$ | Medium |
| $\Theta_{SDF1}$ | Medium |
| $\lambda_{SDF1(\tau 1)}$ | Medium |
| $V_{\tau\, all}$ | Medium |
| $\lambda_{V\tau}$ | Medium |
| $k_{KIT}$ | Medium |
| $k_{SDF1}$ | Medium |
| $g_{\tau 1}$ | Low |
| $\Theta_{KIT}$ | Low |
| *Phase II* | |
| $d_{\tau' 1}$ | High |
| $J_{\tau'\text{-}\tau'}$ | Medium |
| $m\tau'$ | Medium |
| $V_{\tau'}$ | Medium |
| $\lambda_{V\tau'}$ | Low |
| $\lambda_{d\tau' 1}$ | Low |

**Table 4.3.** Data for the number of incomplete trials and the number of trials with cell counts outside one standard deviation (SD) of the normal conditions for Phase I. The number of incomplete trials represents the number of simulations that did not run the entire simulation time length. Trials were considered outside of the SD range if the number of primordial germ cells (PGCs) was greater or less than one standard deviation of the cell abundances under normal parameter values. Combined values show results for a parameter adjusted -10% and +10%. (-): parameter value decreased 10%; (+): parameter value increased 10%.

| Parameter | Incomplete Trials | Combined Incomplete | Trials Outside of SD Range | Combined Outside of Range |
|---|---|---|---|---|
| $J_{\tau\text{-}\tau}$ (-) | 6 | 18 | 5 | 8 |
| $J_{\tau\text{-}\tau}$ (+) | 12 | | 3 | |
| $g_{\tau 1}$ (-) | 5 | 9 | 1 | 5 |
| $g_{\tau 1}$ (+) | 4 | | 4 | |
| $\lambda_{KIT\,(\tau 1)}$ (-) | 15 | 18 | 4 | 7 |
| $\lambda_{KIT\,(\tau 1)}$ (+) | 3 | | 3 | |
| $\lambda_{SDF1(\tau 1)}$ (-) | 3 | 12 | 4 | 7 |
| $\lambda_{SDF1(\tau 1)}$ (+) | 9 | | 3 | |
| $\lambda_{V\tau}$ (-) | 7 | 8 | 10 | 19 |
| $\lambda_{V\tau}$ (+) | 1 | | 9 | |
| $m_{\tau 1}$ (-) | 5 | 8 | 9 | 11 |
| $m_{\tau 1}$ (+) | 3 | | 2 | |
| Normal | 2 | 2 | 3 | 3 |
| $V_{\tau}$ (-) | 9 | 9 | 10 | 18 |
| $V_{\tau}$ (+) | 0 | | 8 | |
| $\Theta_{SDF1}$ (-) | 5 | 10 | 8 | 12 |
| $\Theta_{SDF1}$ (+) | 5 | | 4 | |
| $\Theta_{KIT}$ (-) | 2 | 5 | 1 | 5 |
| $\Theta_{KIT}$ (+) | 3 | | 4 | |
| $D_{KIT}$ (-) | 6 | 11 | 3 | 10 |
| $D_{KIT}$ (+) | 5 | | 7 | |
| $D_{SDF1}$ (-) | 8 | 13 | 8 | 9 |
| $D_{SDF1}$ (+) | 5 | | 1 | |
| $k_{KIT}$ (-) | 10 | 16 | 4 | 8 |
| $k_{KIT}$ (+) | 6 | | 4 | |
| $k_{SDF1}$ (-) | 2 | 12 | 5 | 10 |
| $k_{SDF1}$ (+) | 10 | | 5 | |

**Table 4.4.** Assessment of parameters based on developmental process accuracy and cell structure integrity in univariate sensitivity analysis for Phase II. A checkmark (✓ ) indicates the parameter showed sensitivity and a line (--) indicates the parameter did not show sensitivity when adjusted ±10%.

| Parameter | Developmental Process | Cell Structure |
|---|---|---|
| $d_{\tau' l}$ | ✓ | ✓ |
| $J_{\tau'-\tau'}$ | ✓ | -- |
| $\lambda_{V\tau'}$ | -- | -- |
| $m\tau'$ | -- | -- |
| $V_{\tau'}$ | -- | -- |
| $\lambda_{d\tau' l}$ | -- | -- |

**Table 4.5.** Data for the number of incomplete trials and the number of trials with cell counts outside one standard deviation (SD) of the normal conditions for Phase II. The number of incomplete trials represents the number of simulations that did not run the entire simulation time length. Trials were considered outside of the SD range if the number of primordial germ cells (PGCs) was greater or less than one standard deviation of the cell abundances under normal parameter values. Combined values show the total trials outside of the normal range for a parameter adjusted -10% and +10%. (-): parameter value decreased 10%; (+): parameter value increased 10%.

| Parameter | Incomplete Trials | Trials Outside of SD Range | Combined Outside Range |
|---|---|---|---|
| $J_{\tau\text{-}\tau}$ (-) | 0 | 13 | 25 |
| $J_{\tau\text{-}\tau}$ (+) | 0 | 12 | |
| $\lambda_{V\tau}$ (-) | 0 | 9 | 20 |
| $\lambda_{V\tau}$ (+) | 0 | 11 | |
| $m_{\tau'}$ (-) | 0 | 23 | 45 |
| $m_{\tau'}$ (+) | 0 | 22 | |
| Normal | 0 | 11 | 11 |
| $V_{\tau}$ (-) | 0 | 25 | 50 |
| $V_{\tau}$ (+) | 0 | 25 | |
| $d_{\tau'l}$ (-) | 0 | 9 | 23 |
| $d_{\tau'l}$ (+) | 0 | 14 | |
| $\lambda_{d\tau'l}$ (-) | 0 | 4 | 12 |
| $\lambda_{d\tau'l}$ (+) | 0 | 8 | |

**Table 5.1.** CC3D functions and parameters to be used for the development of a model of the preantral stages of folliculogenesis in rhesus macaque. Functions are categorized by the biological process they simulate.

| Biological Process | Function | Parameters |
|---|---|---|
| Oocyte growth | Volume Steppable | Target volume<br>Lambda volume<br>Growth rate |
| Proliferation of follicular cells | Mitosis Steppable | Mitotic rate of cell types |
| Cell adhesion | Contact Energy Plugin | Contact energy between cell types |
| Molecular signaling | Secretion Steppable | Secretion rate |
| | Diffusion Solver Steppable | Diffusion rate of signaling compound<br>Decay rate of signaling compound signal |

**Table 5.2.** Data results from literature searches on folliculogenesis in rhesus macaques and other mammalian species.

| Data Type | Value | Units | Species | Reference |
|---|---|---|---|---|
| *Morphological characterization of ovarian follicles* | | | | |
| Primordial | Single layer of squamous granulosa cells | | Mammals | (Erickson, 1995) |
| Primary | Increased oocyte size; single layer layer of cuboidal granulosa cells; formation of zona pellucida | | Mammals | (Erickson, 1995) |
| Secondary | Increased oocyte size; Two layers of cuboidal granulosa cells; presence of theca cells | | Mammals | (Erickson, 1995) |
| *Follicle diameter* | | | | |
| Primordial | 25-50 | μm | Rhesus macaque | personal communication with M. Zelinski, 2016 |
| Primordial transitional | 51-70 | μm | Rhesus macaque | personal communication with M. Zelinski, 2016 |
| Primary | 71-149 | μm | Rhesus macaque | personal communication with M. Zelinski, 2016 |
| Secondary | 150-225 | μm | Rhesus macaque | personal communication with M. Zelinski, 2016 |
| *Proportion of follicle stages* | | | | |
| Primordial | 49 | % | Baboon (*Papio anubis*) (5-15 years age) | (Amorim et al., 2016) |
| Primordial | 375 | Follicles | Rhesus macaque (< 5 years age) | (Nichols et al., 2005) |
| Primordial | 325 | Follicles | Rhesus macaque (5-10 years age) | (Nichols et al., 2005) |
| Primordial | 235 | Follicles | Rhesus macaque (10-15 years age) | (Nichols et al., 2005) |
| Primordial | 140 | Follicles | Rhesus macaque (15-20 years age) | (Nichols et al., 2005) |
| Primordial | 45 | Follicles | Rhesus macaque (>20 years age) | (Nichols et al., 2005) |
| Primary | 26 | % | Baboon (*Papio anubis*) (5-15 years age) | (Amorim et al., 2016) |

| | | | | |
|---|---|---|---|---|
| Primary | 85 | Follicles | Rhesus macaque (< 5 years age) | (Nichols et al., 2005) |
| Primary | 61 | Follicles | Rhesus macaque (5-10 years age) | (Nichols et al., 2005) |
| Primary | 90 | Follicles | Rhesus macaque (10-15 years age) | (Nichols et al., 2005) |
| Primary | 73 | Follicles | Rhesus macaque (15-20 years age) | (Nichols et al., 2005) |
| Primary | 32 | Follicles | Rhesus macaque (>20 years age) | (Nichols et al., 2005) |
| Secondary | 23 | % | Baboon (*Papio anubis*) (5-15 years age) | (Amorim et al., 2016) |
| *Primordial to primary follicle activation* (*in vitro*) | | | | |
| Androgen (dihydrotestosterone) treatment | 2.5-fold increase | Primary follicle counts | Rhesus macaque | (Vendola et al., 1999) |
| *Primordial follicle activation and growth to primary follicles (in vitro)* | | | | |
| FOXL2 | Up-regulation | | Mouse (*Mus musculus*)<br>Human (*Homo sapiens*) | (Uda et al., 2004)<br>(Crisponi et al., 2001) |
| SOHLH2 | Up-regulation | | Mouse (*Mus musculus*) | (Choi, Yuan, & Rajkovic, 2008) |
| SOHLH2<br>LHX8 | Up-regulation | | Mouse (*Mus musculus*) | (Pangas et al., 2006) |
| FOXO3 | Up-regulation | | Mouse (*Mus musculus*) | (Castrillon, Miao, Kollipara, Horner, & DePinho, 2003) |
| NOBOX | Up-regulation | | Mouse (*Mus musculus*) | (Rajkovic, Pangas, Ballow, Suzumori, & Matzuk, 2004) |
| *Timeline of processes in ovarian development and folliculogenesis* | | | | |
| Primordial stage residence | >300 | Days | Human (Homo sapiens) | (Gougeon, 1986) |
| Primary stage residence | 150 | Days | Human (Homo sapiens) | (Gougeon, 1986) |
| Secondary stage residence | 120 | Days | Human (Homo sapiens) | (Gougeon, 1986) |
| Gestational period | 0 to 164-168 | Days | Rhesus macaque | (Simpson & Van Wagenen, 1973) |

**Table 5.3.** Data on follicle abundances and stages derived from analysis of H&E stained ovarian tissue samples from gestational day 130 rhesus macaques.

| Sample ID (per section) | Primordial Follicle Abundance | Primary Follicle Abundance | Secondary Follicle Abundance |
|---|---|---|---|
| 20478-LT-20A | 4 | 1 | 0 |
| 20478-LT-30A | 23 | 4 | 0 |
| 20478-LT-31A | 0 | 0 | 0 |
| 20478-LT-10A | 10 | 1 | 0 |
| 22724-RT-10C | 369 | 18 | 1 |
| 22724-RT-10B | 334 | 14 | 0 |
| 22724-RT-11A | 159 | 20 | 3 |
| 22724-RT-11B | 432 | 14 | 0 |
| 22724-RT-11C | 337 | 19 | 0 |
| 22724-RT-12A | 376 | 13 | 0 |
| 22724-RT-12C | 421 | 10 | 0 |
| 22724-RT-14A | 416 | 9 | 0 |
| 22724-RT-14B | 347 | 12 | 0 |
| 22724-RT-14C | 359 | 11 | 0 |
| 22724-RT-15A | 363 | 11 | 0 |
| 22724-RT-15B | 304 | 5 | 0 |
| 22724-RT-15C | 415 | 13 | 0 |
| 22724-RT-16A | 233 | 15 | 0 |
| 22724-RT-16B | 377 | 12 | 0 |
| 22724-RT-16B | 377 | 12 | 0 |
| 22724-RT-16C | 360 | 24 | 0 |
| 23316-LT-1A | 117 | 5 | 0 |
| 23316-LT-1B | 158 | 7 | 0 |
| 23316-LT-1C | 197 | 4 | 0 |
| 23316-LT-2A | 297 | 9 | 0 |
| 23316-LT-2C | 82 | 50 | 6 |
| 23316-LT-3B | 121 | 41 | 4 |
| 23316-LT-3A | 142 | 46 | 9 |
| 23316-RT-3C | 64 | 26 | 3 |

| | | | |
|---|---|---|---|
| 23316-RT-1C | 10 | 7 | 0 |
| 23316-LT-7C | 57 | 13 | 0 |
| 23316-LT-7B | 58 | 8 | 0 |
| 23316-LT-5C | 105 | 28 | 3 |
| 23316-LT-5B | 99 | 26 | 2 |
| 23316-RT-2A | 25 | 6 | 0 |
| 23316-LT-7A | 76 | 17 | 1 |
| 22724-RT-7A | 284 | 23 | 2 |
| 22724-RT-8A | 259 | 38 | 5 |
| 22724-RT-9A | 228 | 31 | 1 |
| 22724-RT-9C | 338 | 32 | 4 |
| 22724-RT-10A | 279 | 34 | 1 |
| 23316-RT-3A | 52 | 27 | 2 |
| 22724-RT-12B | 162 | 7 | 1 |
| 22724-RT-8B | 414 | 16 | 1 |
| 23316-LT-3C | 209 | 26 | 3 |
| 23316-LT-5A | 108 | 36 | 0 |
| 23316-LT-4B | 133 | 32 | 3 |
| 23316-RT-1A | 6 | 2 | 1 |
| 23316-RT-7C | 41 | 30 | 6 |
| 23316-LT-2B | 206 | 22 | 2 |

# FIGURES

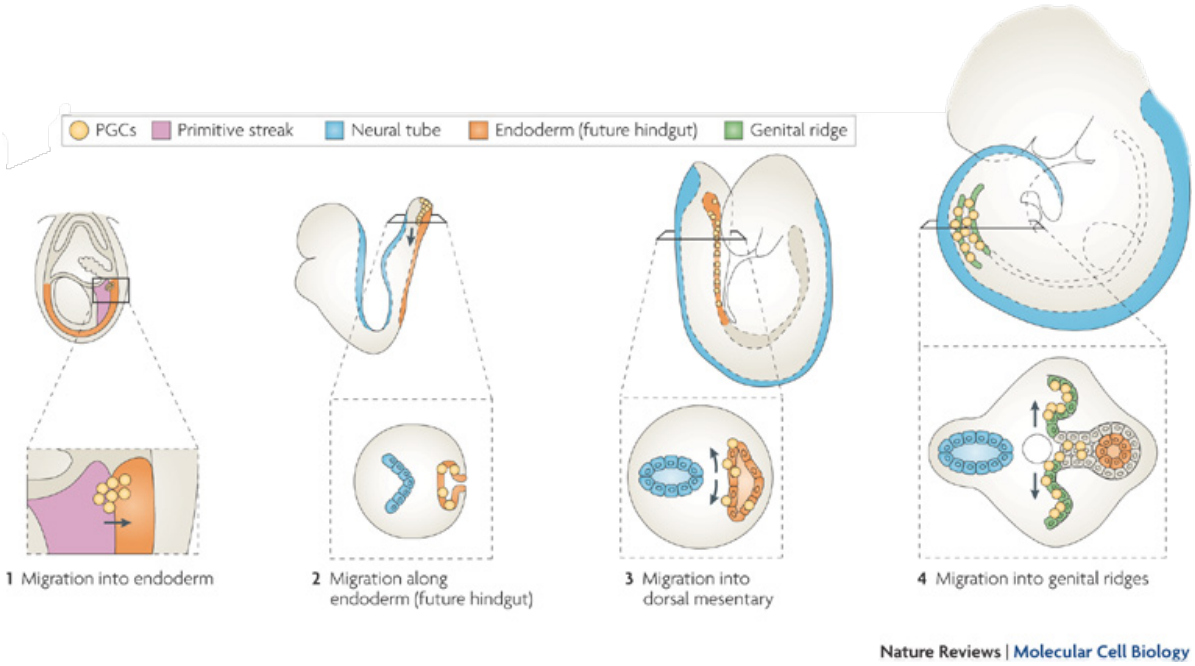


**Fig. 1.1.** The migration stages of primordial germ cells (PGCs) from the posterior region of the mouse embryo to the gonadal ridge (called genital ridges in Fig. 1.1). PGCs migrate into the endoderm and move along the hindgut until reaching the gonadal ridge. With permission, this figure is from (Richardson & Lehmann, 2010).

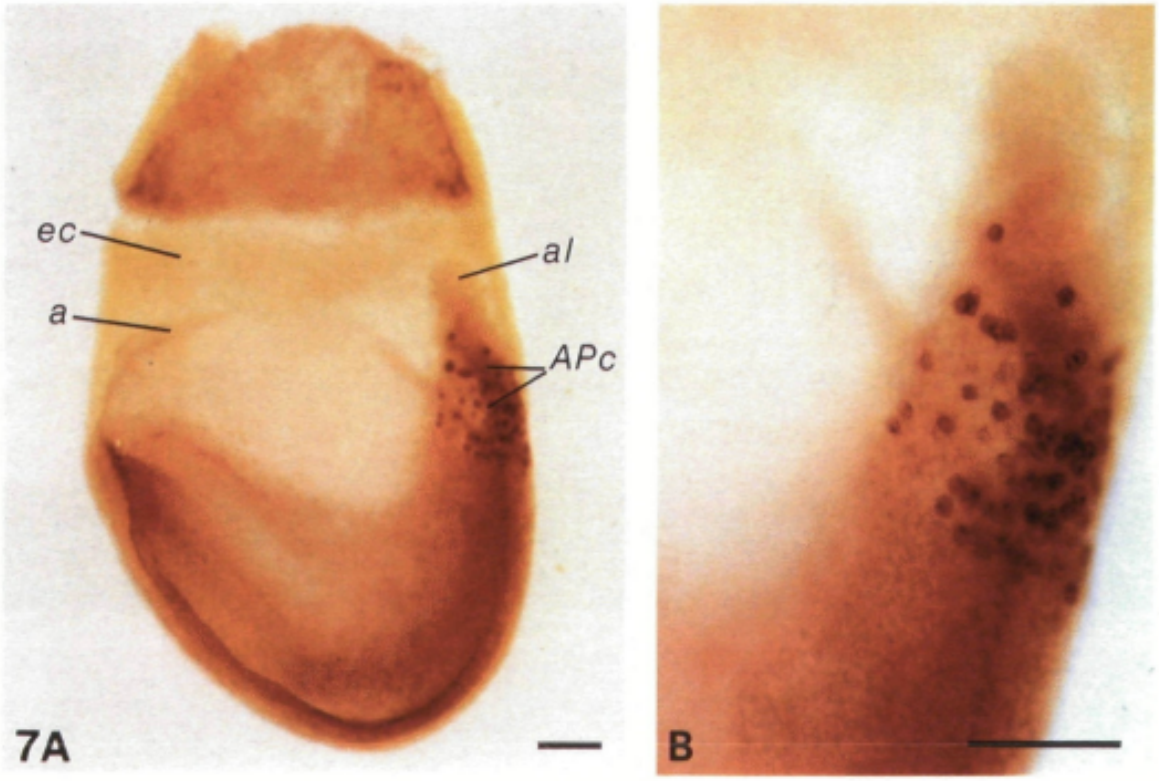


**Fig. 1.2.** On the left, a whole-mount image of a mouse embryo on embryonic day 7 (E7) showing primordial germ cells (PGCs) in the posterior region of the embryo through alkaline phosphatase expression (APc). On the right, a close up of PGCs in the posterior region of the mouse embryo. With permission, this figure is from (Ginsburg et al., 1990). Exocoelom (ec); amnion (a); allantois (al).

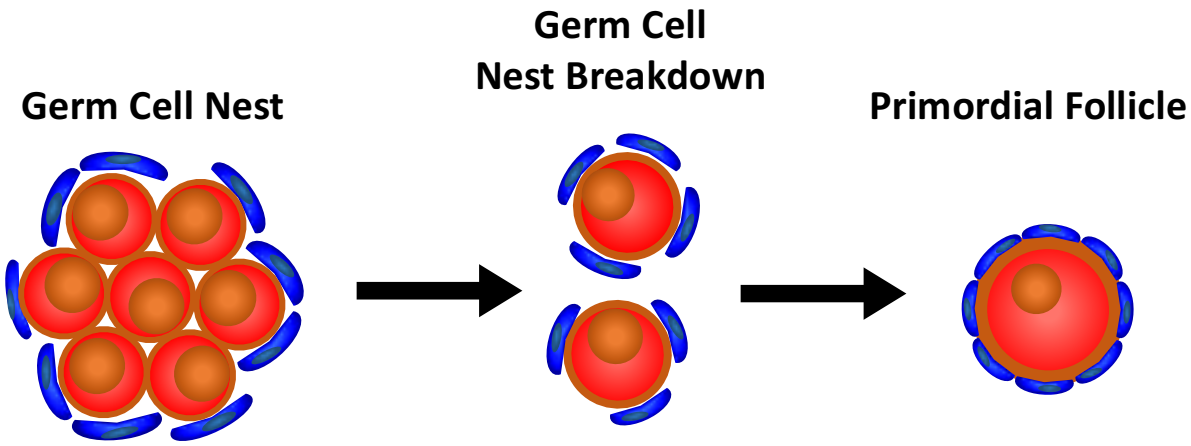


**Fig. 1.3.** In mice, germ cell nests, connected oogonia surrounded by granulosa cells, initiate nest breakdown at birth and begin to form primordial follicles. Oocytes/oogonia (red); granulosa cells (blue).

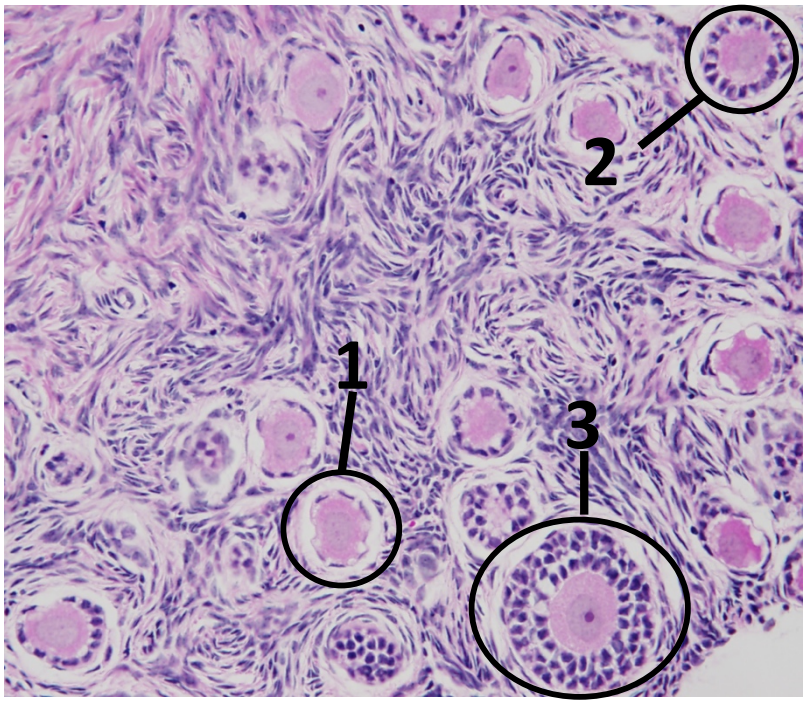


**Fig. 1.4.** Section of rhesus macaque ovarian tissue stained with hematoxylin and eosin showing follicles at different stages of development. 1) primordial follicle; 2) primary follicle; 3) secondary follicle.

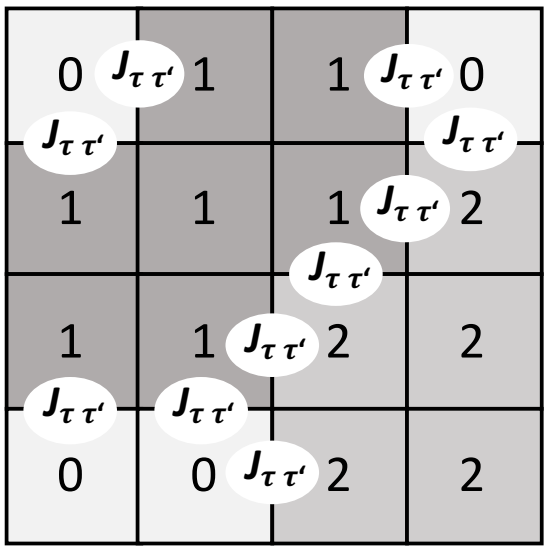


**Fig. 1.5.** Contact energies ($J_{\tau\,\tau'}$) between cells are shown at bordering pixels from different cells. Cell types are denoted by number and pixels are shown as squares in the figure.

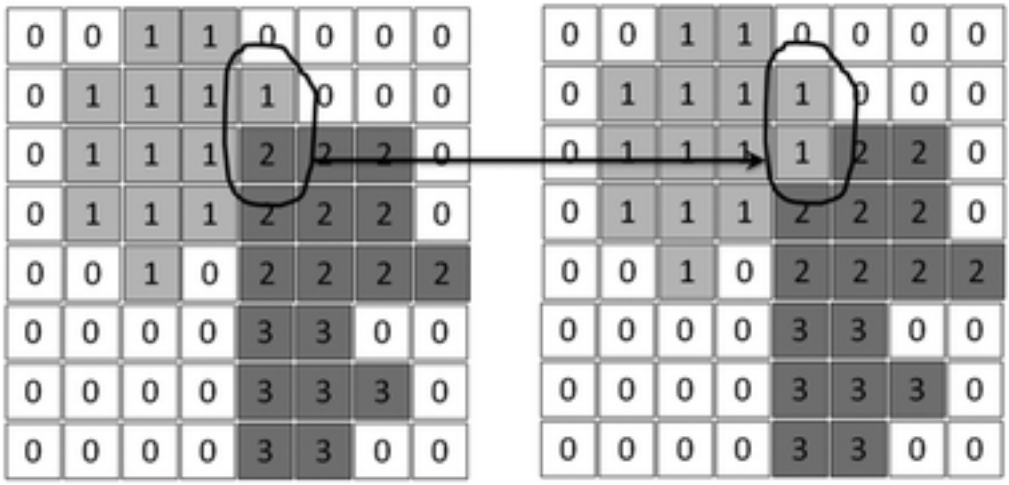


**Fig. 1.6.** A representation of a pixel-copy attempt in a Cellular Potts model. A pixel, chosen at random, of type one cell makes a pixel-copy attempt to a neighboring pixel of a type two cell. The pixel-copy attempt is accepted and the neighboring pixel transitions from type two to type one. Bordering pixels in the figure, shown as squares, that have the same cell type ID (shown by number) make up cells in the model. Fig. 1.2., with permission, is from Mortazavi et al. (Mortazavi, D'Souza, & Nosonovsky).

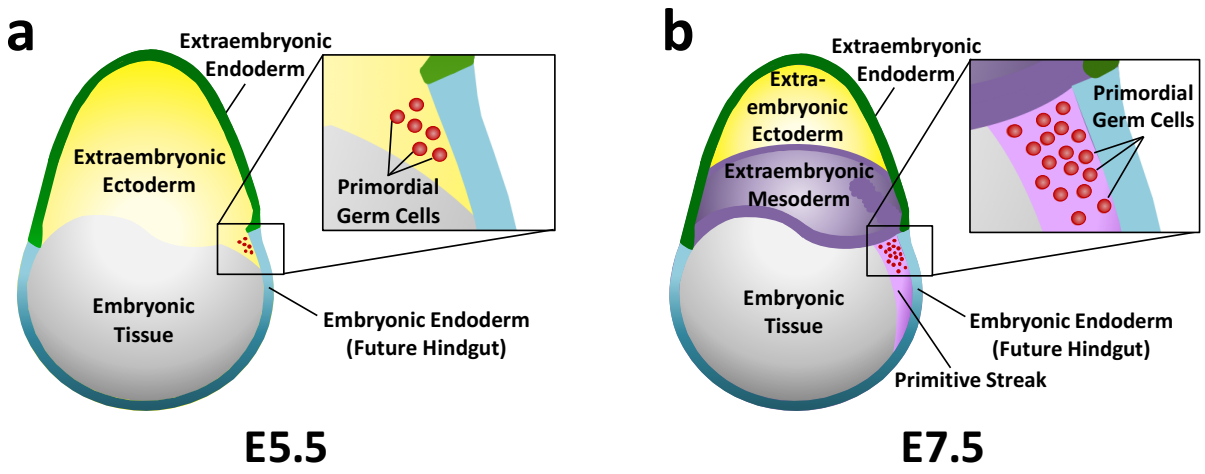


**Fig. 2.1.** Embryonic tissues in early development. **a)** First appearance of six primordial germ cells (red) in the posterior extraembryonic ectoderm (*yellow*) near the embryonic endoderm (*blue*) of a mouse embryo (*grey*) on embryonic day 5.5 (E5.5). **b)** On E7.5, the population of primordial germ cells has increased and is present in the primitive streak (*magenta*) near the extraembryonic mesoderm (*purple*) and embryonic endoderm (*blue*) of the mouse embryo (*grey*). With permission, this figure is from Wear et al. (Wear et al., 2016).

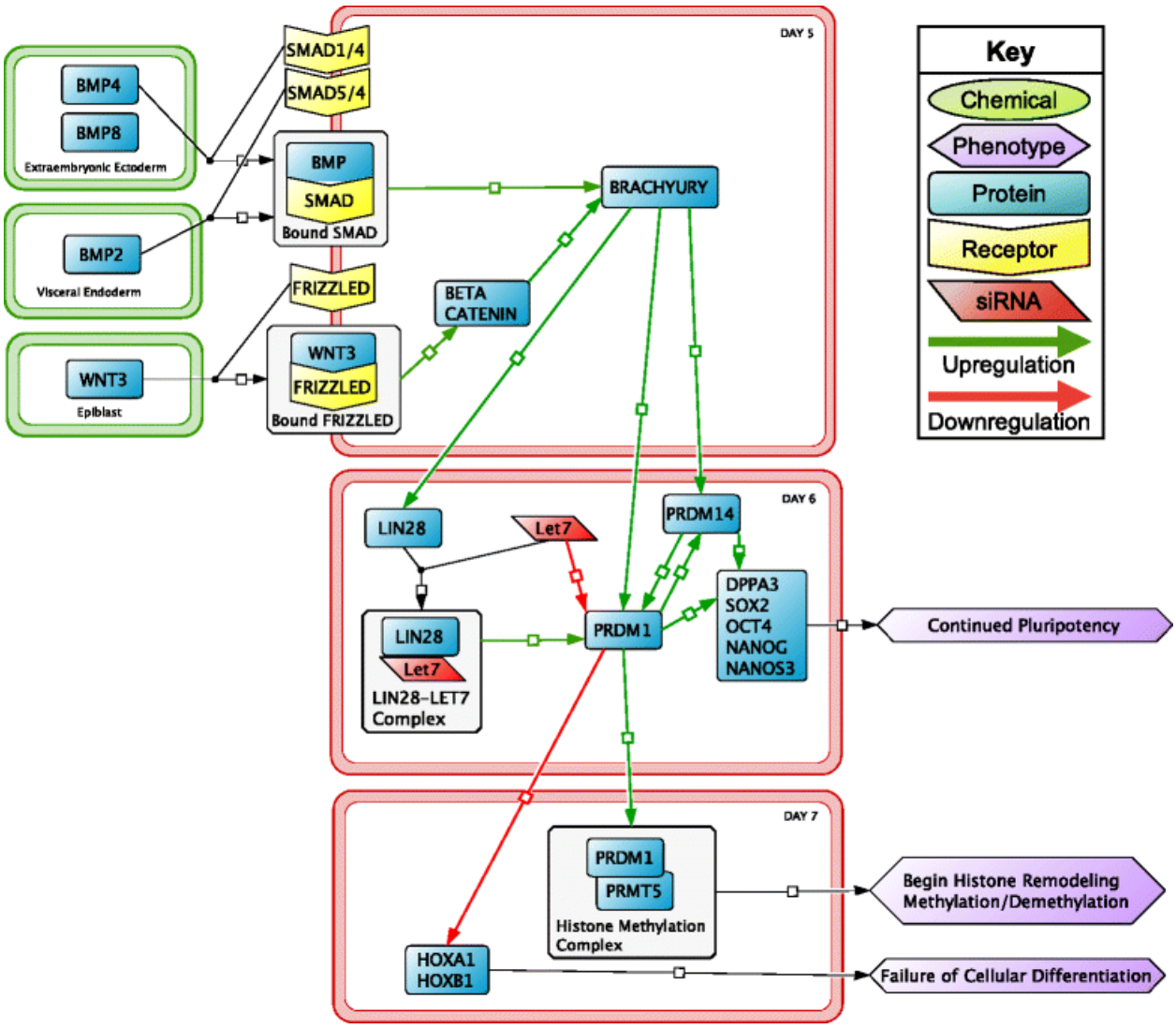


**Fig. 2.2.** The initial signaling interactions in primordial germ cells begin on embryonic day 5 (E5) and are involved in the maintenance of pluripotency factors. Molecular events from E5 to E7 occur between the primordial germ cells (*red outline*) and embryonic tissues (*green outline*). With permission, this figure is from Wear et al. (Wear et al., 2016).

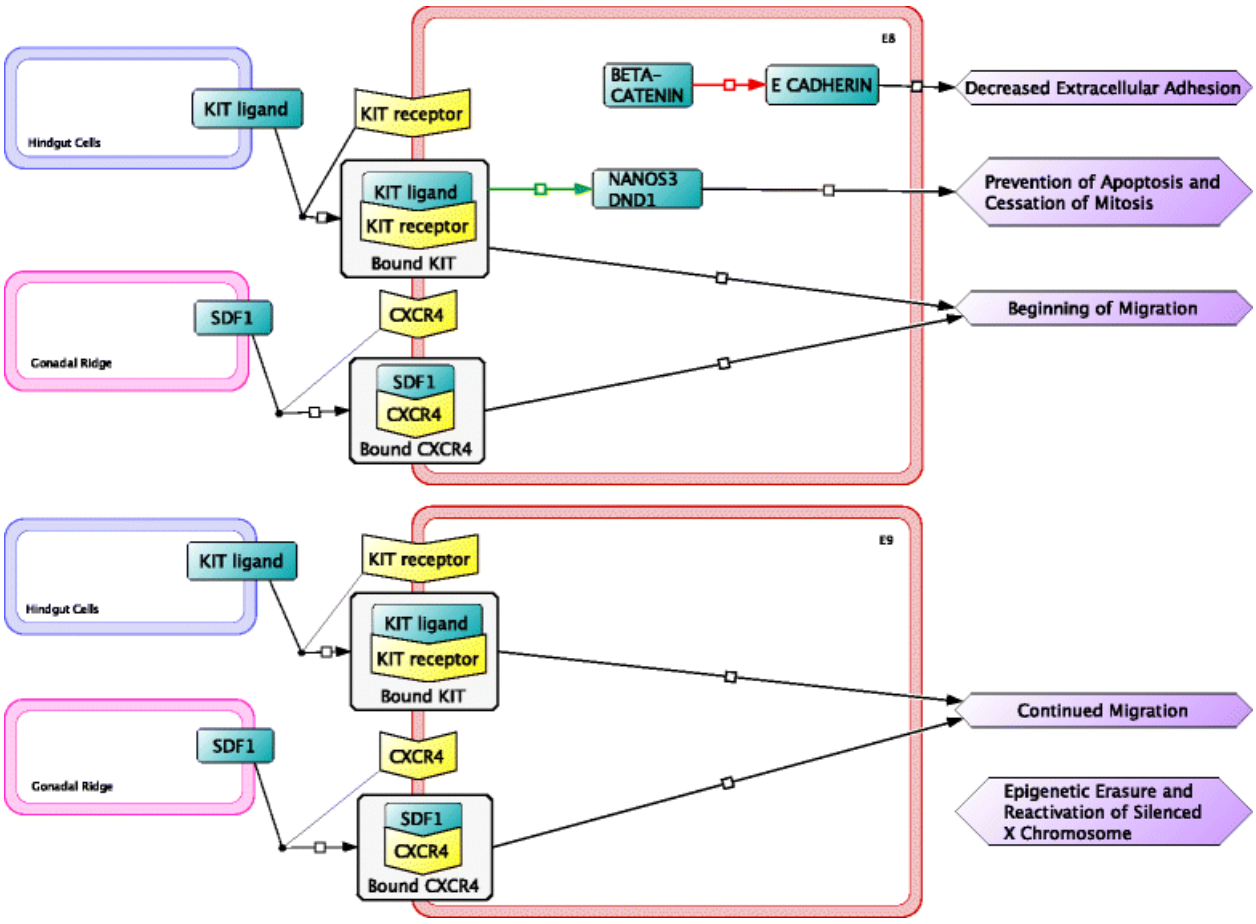


**Fig. 2.3.** During embryonic day 8 (E8) to E9, adhesion between primordial germ cells is downregulated and expression of factors initiating migration signals are upregulated. The gonadal ridge (*pink outline*) and hindgut (*blue outline*) secrete chemoattractant compounds to primordial germ cells (*red outline*) that influence migration. With permission, this figure is from Wear et al. (Wear et al., 2016).

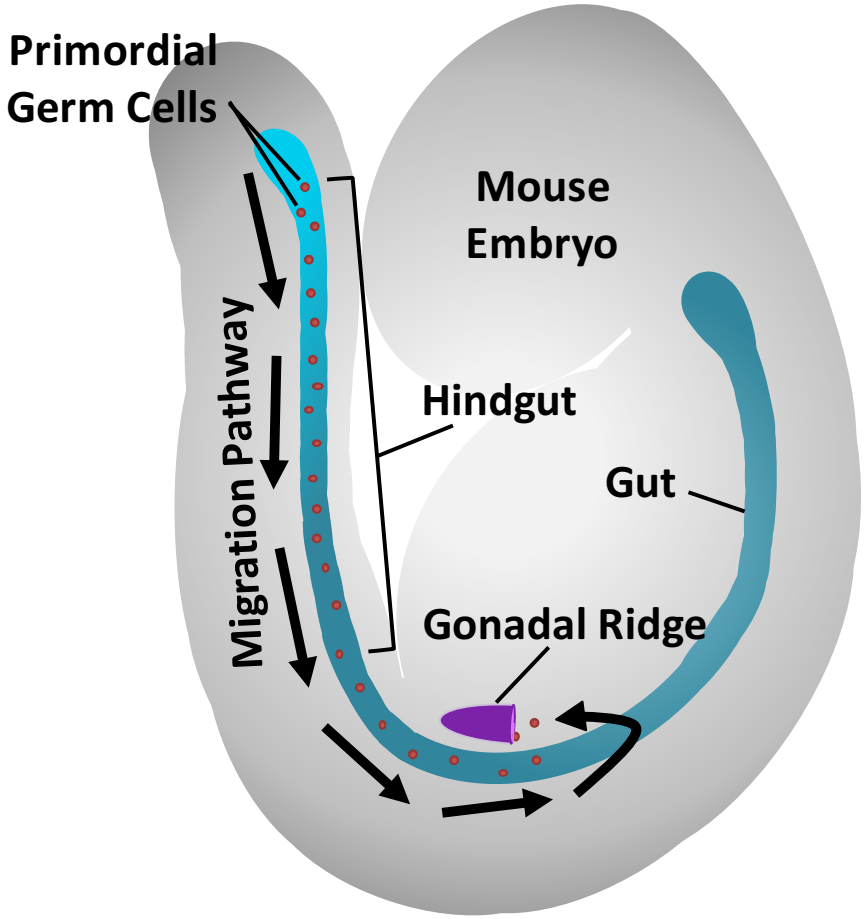


**Fig. 2.4.** Migration of primordial germ cells (*red*) along the hindgut (*blue*) toward the gonadal ridge (*purple*) in the mouse embryo (*grey*) on embryonic day nine (E9). Arrows show the pathway of primordial germ cell migration. With permission, this figure is from Wear et al. (Wear et al., 2016).

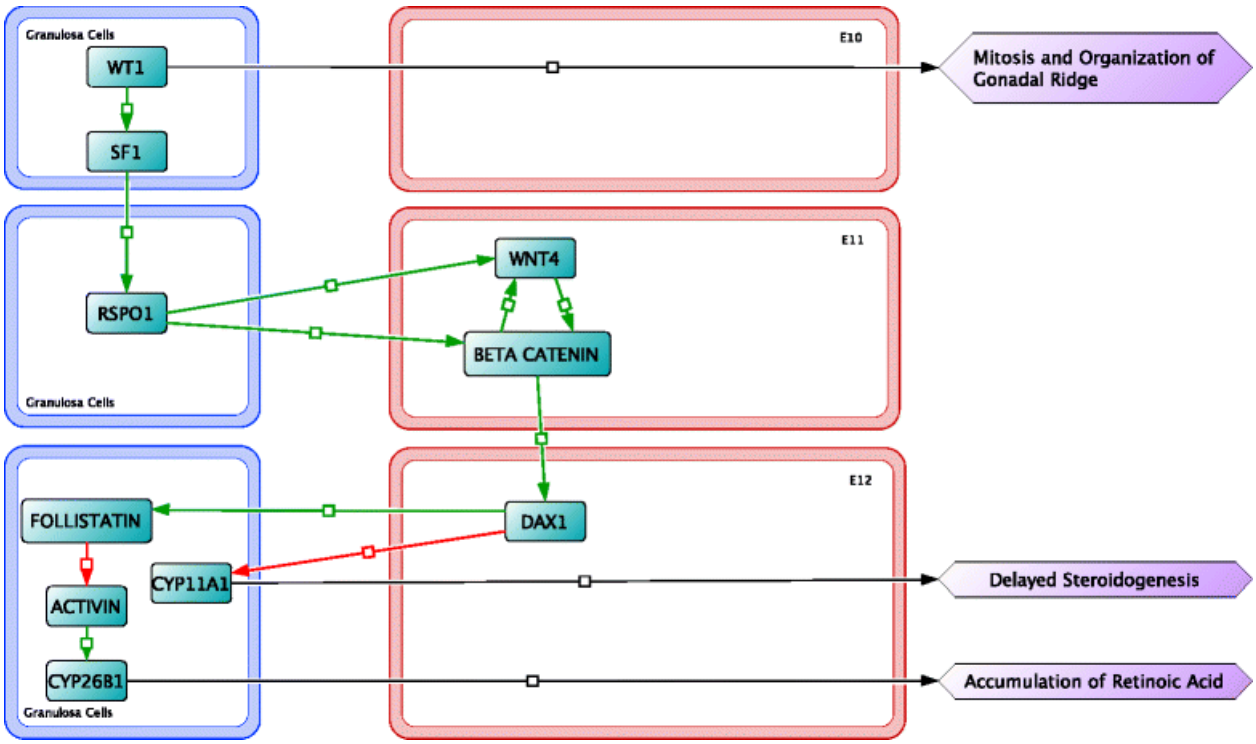


**Fig. 2.5.** Signaling important in female sex differentiation, between somatic (i.e. granulosa) cells (*blue outline*) and oogonia (*red outline*), begins embryonic day 10 (E10) to E12. With permission, this figure is from Wear et al. (Wear et al., 2016).

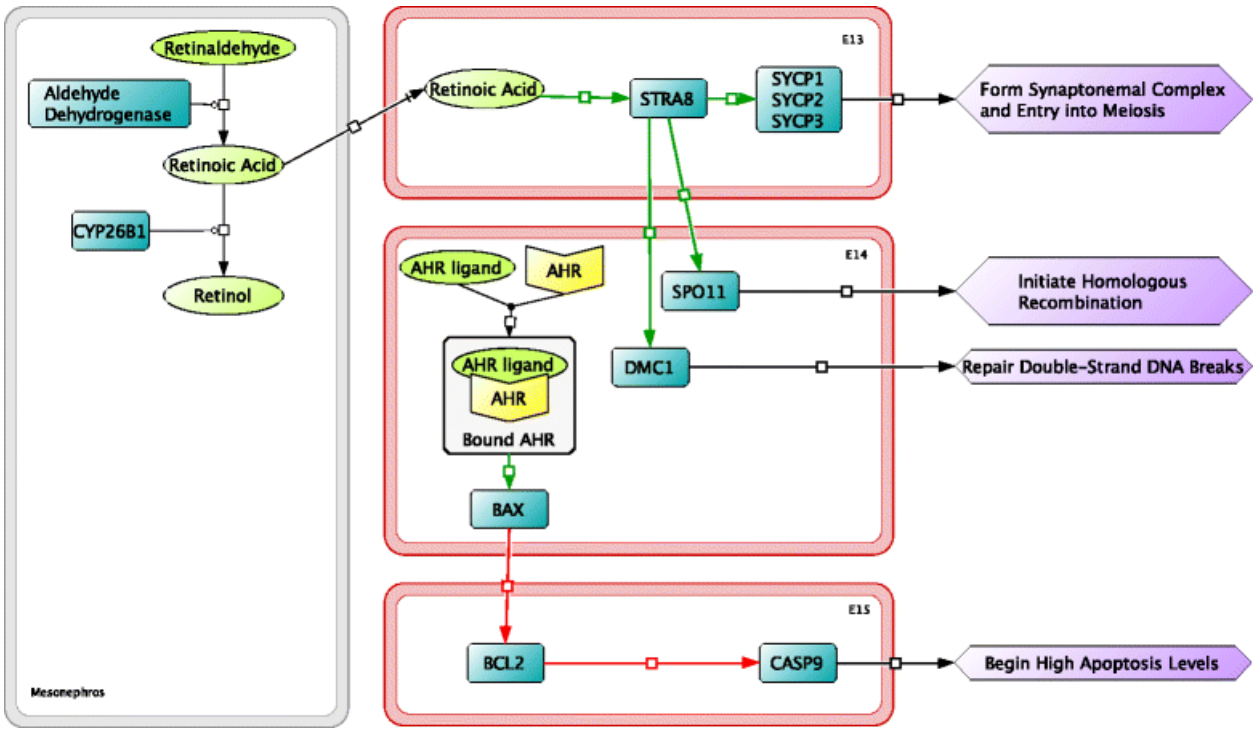


**Fig. 2.6.** From embryonic day 13 (E13) to E15, molecular interactions involved in female sex differentiation in oocytes (*red outline*) and mesonephric cells (*gray outline*) continue. During this time period apoptosis of oocytes is initiated through activation of the aryl hydrocarbon receptor. With permission, this figure is from Wear et al. (Wear et al., 2016).

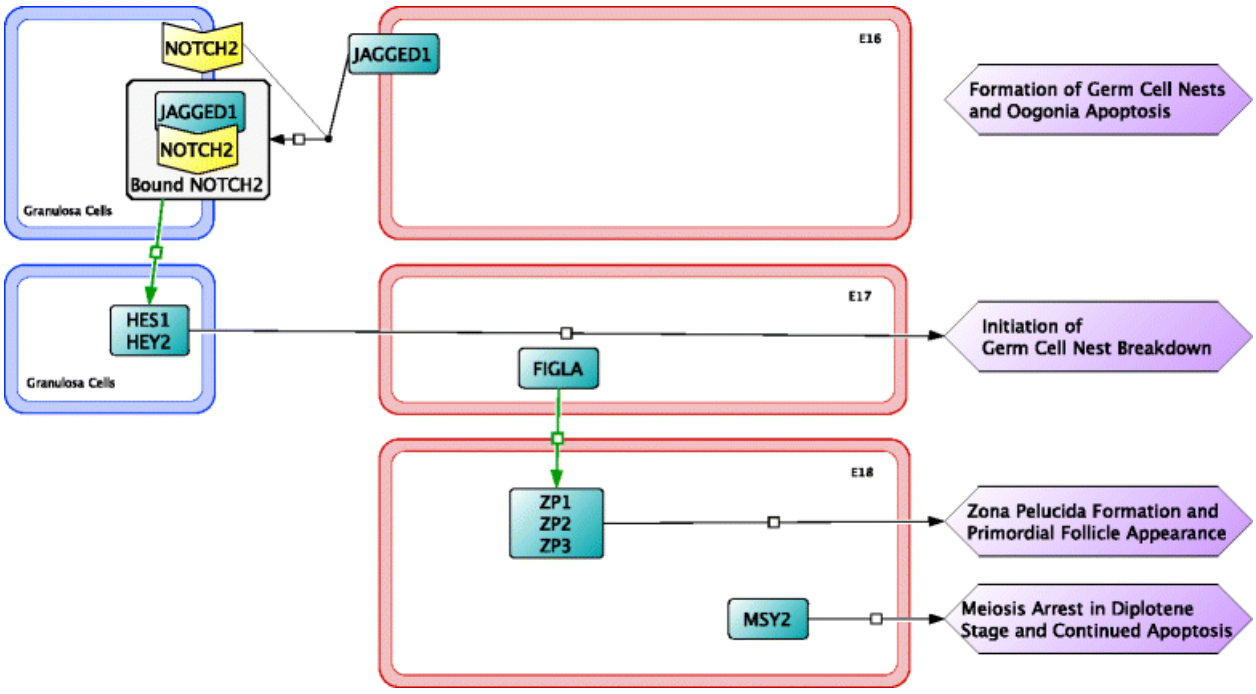


**Fig. 2.7.** Signaling between granulosa cells (*blue outline*) and oocytes (*red outline*) initiating the formation of germ cell nests occurs from embryonic day 16 (E16) to E18. The exact signaling pathways for the formation of germ cell nests is unknown. With permission, this figure is from Wear et al. (Wear et al., 2016).

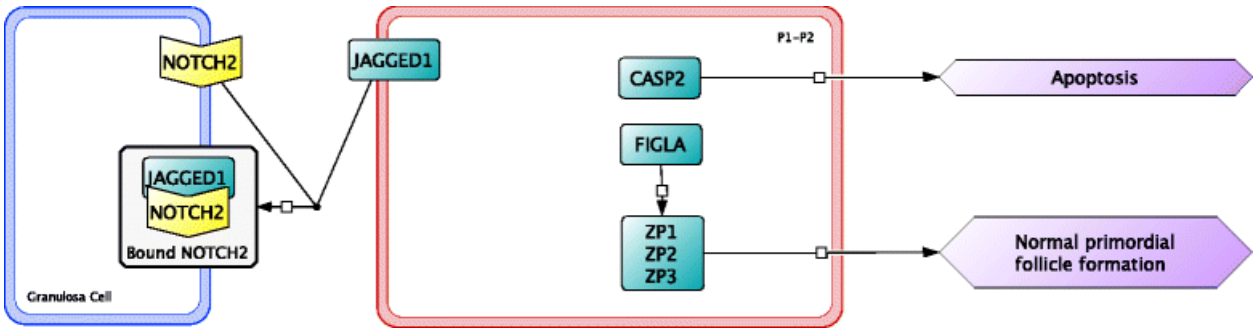


**Fig. 2.8.** The last stage of early ovarian development occurs after birth from postnatal day 0 (P0) to P2 involving the continued breakdown of germ cell nests and formation of primordial follicles in granulosa cells (*blue outline*) and oocytes (*red outline*). The mechanism for these processes is also not well known. With permission, this figure is from Wear et al. (Wear et al., 2016).

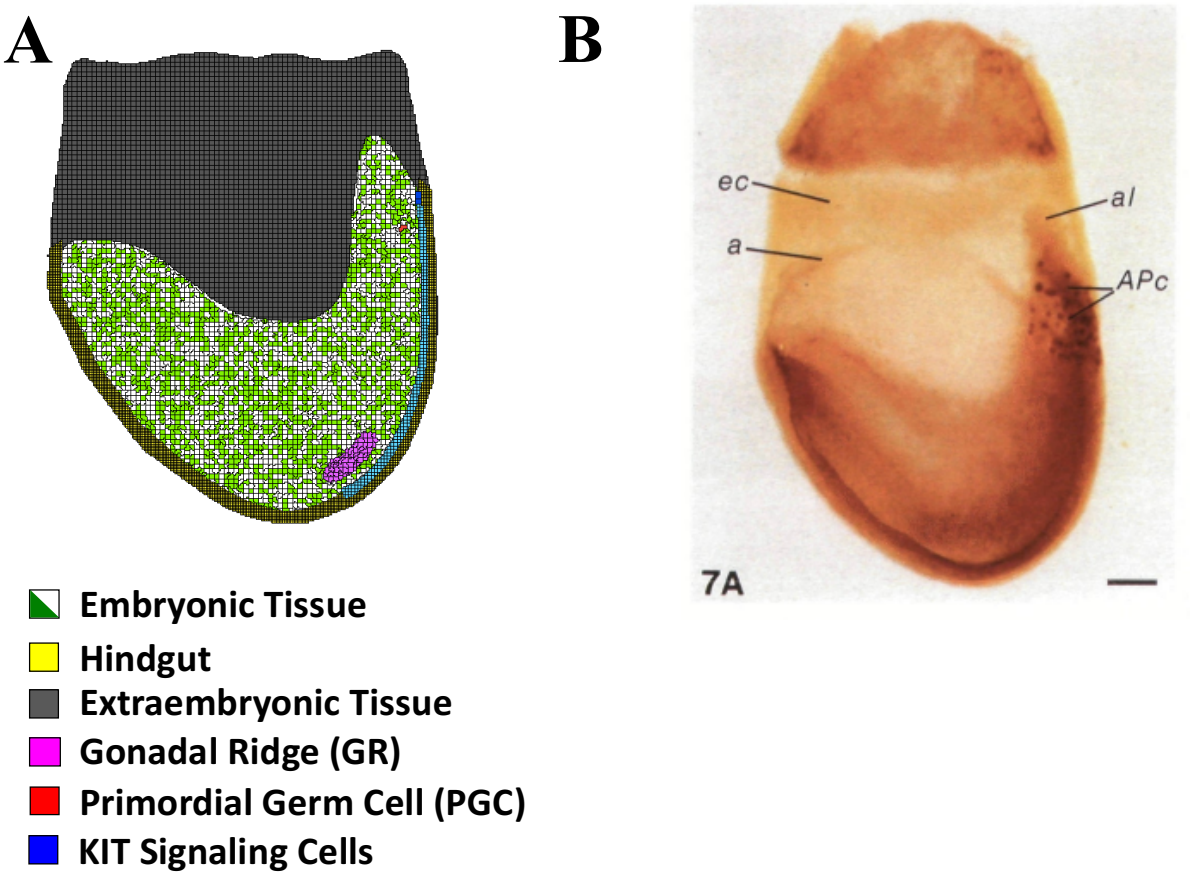


**Fig. 3.1.** The initial layout for Phase I of the model (A) was designed from a whole mount image of a mouse embryo (B) whole mount embryo stained with alkaline phosphatase for PGC identification from (Ginsburg et al., 1990) with permission. Cell types important to ovarian development from E5.5-E12.5 were specified and identified by color, embryonic tissue (green/white), hindgut (yellow), extraembryonic tissue (grey), gonadal ridge (magenta), primordial germ cell (red), and KIT signaling cells (blue).

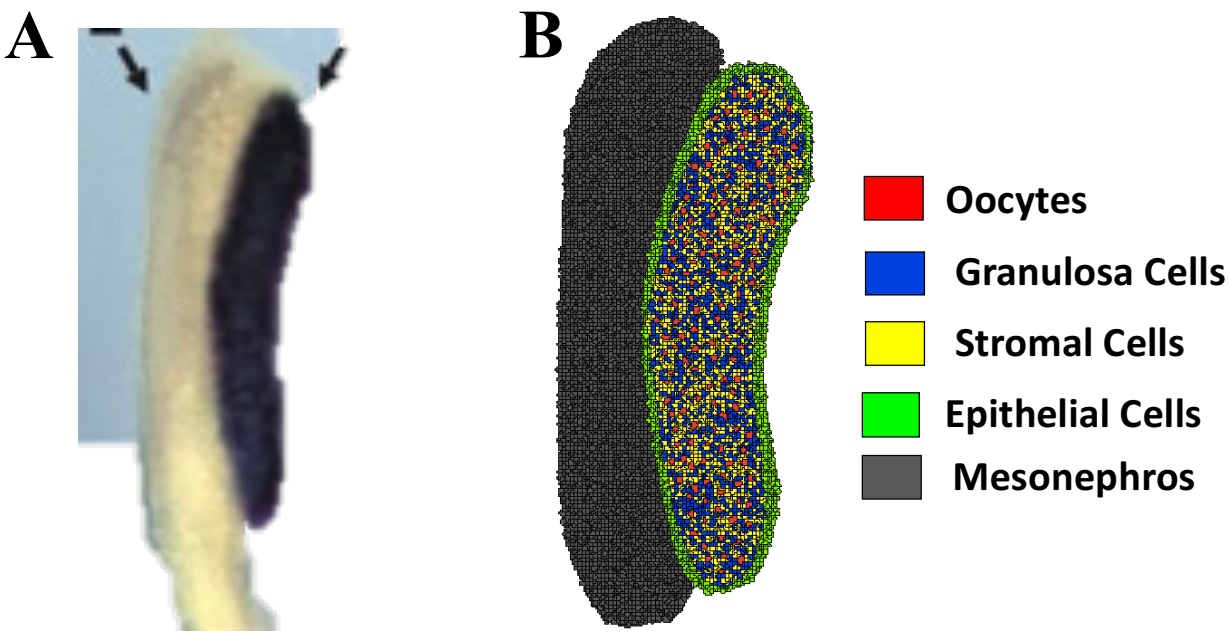


**Fig. 3.2.** The initial layout for Phase II of the model (A) was designed from a whole mount image of an XX mouse gonad (B) whole mount ovary stained for follistatin to identify gonadal cells from (Manuylov et al., 2008) with permission. Cell types important to ovarian development from E12.5-P2 were specified and identified by color, oocytes (red), granulosa cells (blue), somatic cells (yellow), epithelial cells (green), and mesonephros (grey).

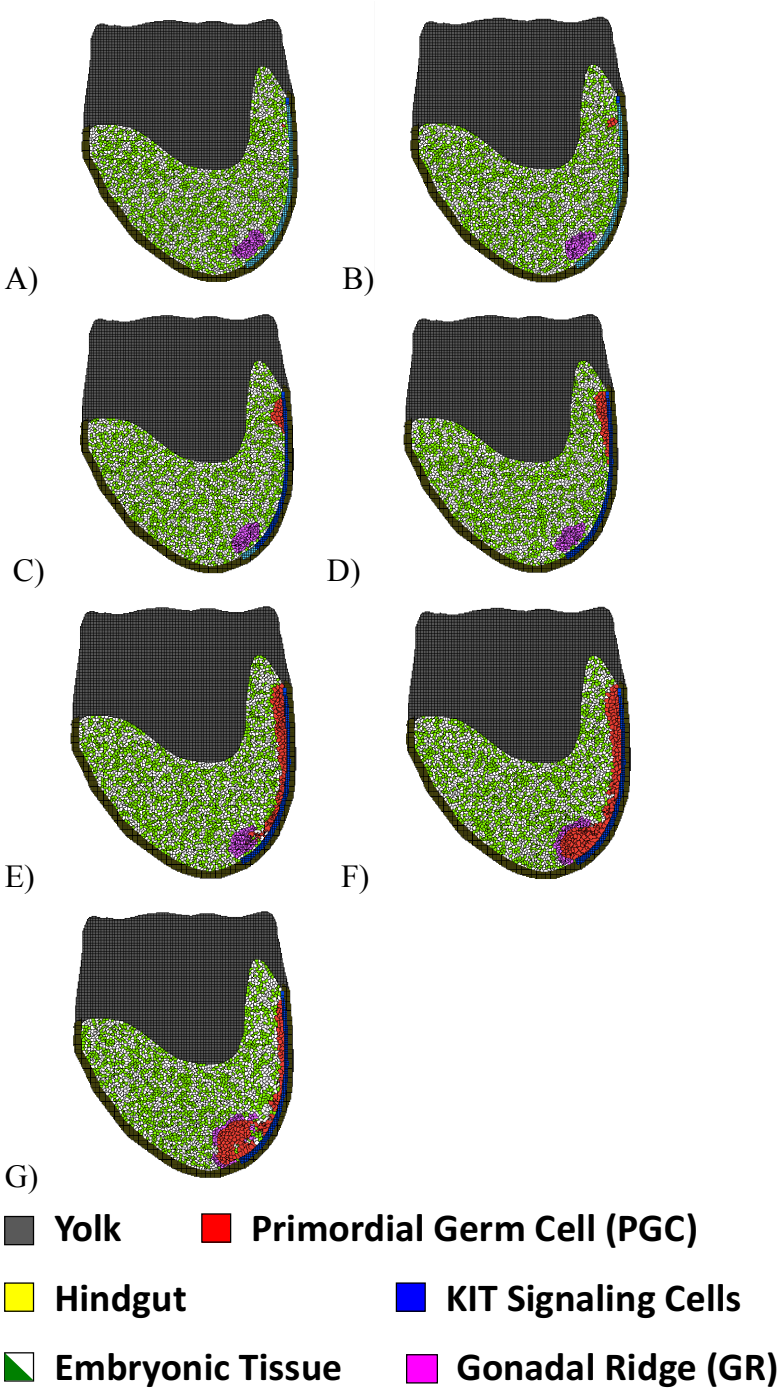


**Fig. 3.3.** Simulation outputs from Phase I at different time points throughout the entire simulation (0-4800 MCS). **A**: 600 MCS (E6.5); **B**: 1200 MCS (E7.5); **C**: 1800 MCS (E8.5); **D**: 2400 MCS (E9.5); **E**: 3000 MCS (E10.5); **F**: 3600 MCS (E11.5); **G**: 4200 MCS (E12.5).

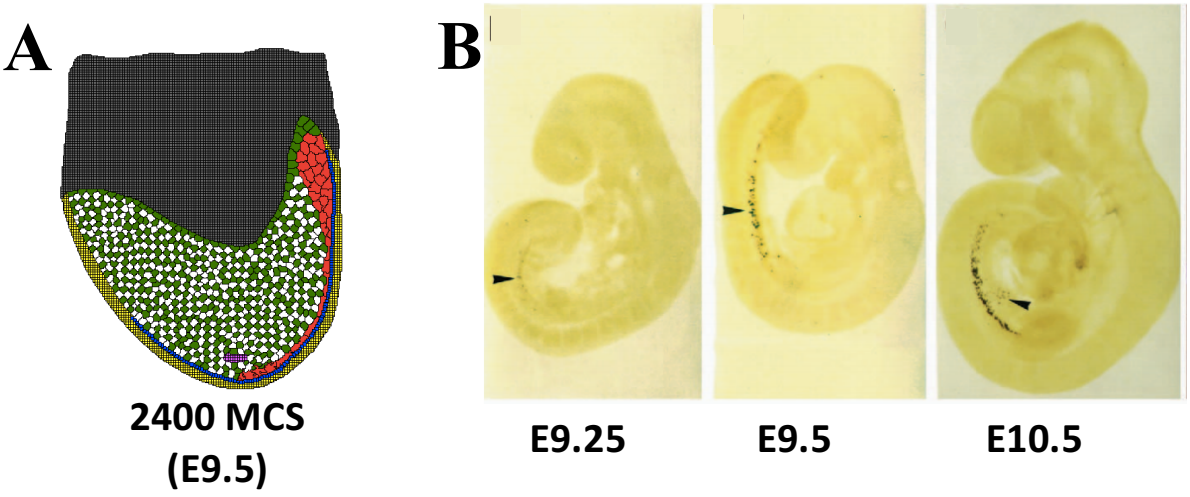


**Fig. 3.4. A)** Phase I simulation output at 2400 MCS (E9.5) showing migration of primordial germ cells (red) to the gonadal ridge (magenta). PGCs move from the posterior region upper region of the embryo to the gonadal ridge in the lower center of the embryo. **B)** Experimental images of mouse embryos show migration of PGCs from E9.25-E10.5 through Oct-4/*lacZ* transgene expression taken from (Yeom et al., 1996) with permission. The experimental images show a horizontally flipped view compared to the simulation output. PGCs in the experimental image migrate from the posterior region (top-left of the embryo (posterior region) to the lower middle (gonadal ridge). Colors of cell types in the model follow those defined in Fig. 3.1.

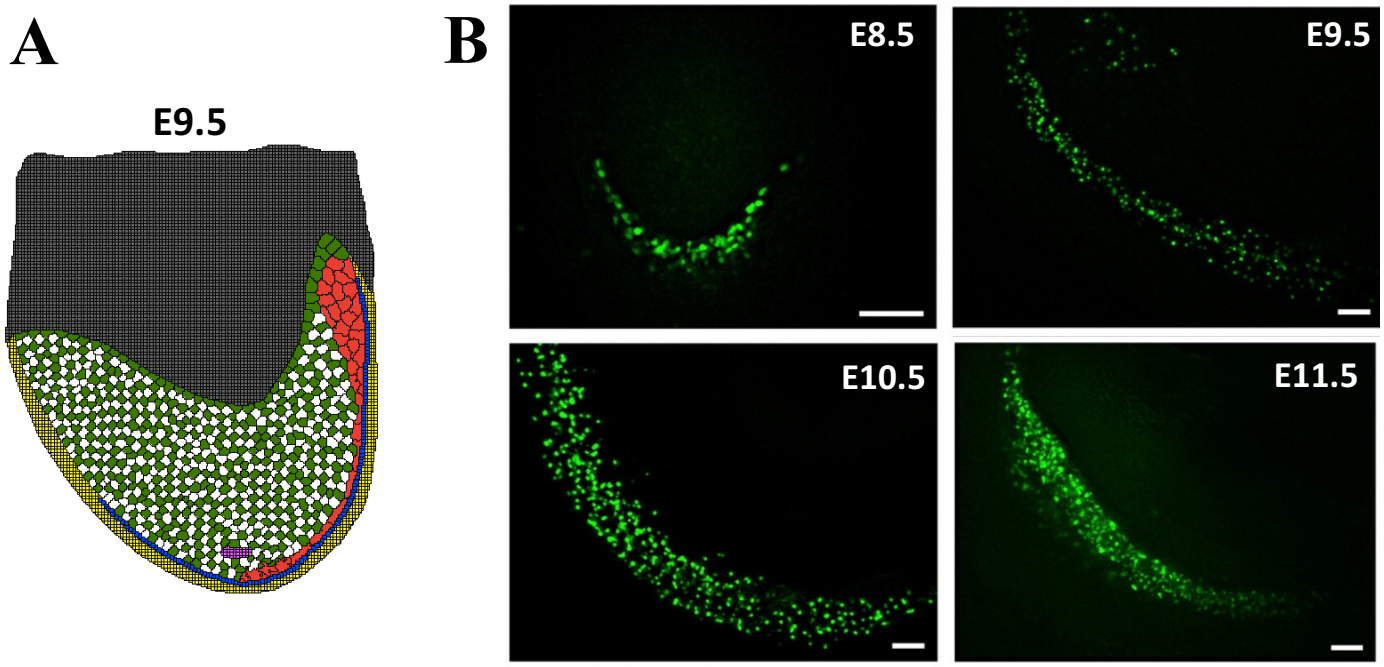


**Fig. 3.5. A)** Phase I simulation output at 2400 MCS (E9.5) showing migration of primordial germ cells (red) to the gonadal ridge (magenta). PGCs move from the posterior region upper region of the embryo to the gonadal ridge in the lower center of the embryo. **B)** Experimental images of mouse embryos show migration of PGCs from E9.25-E10.5 through Oct-4-GFP expression from (Francis & Lo, 2006) with permission. The experimental images show a horizontally flipped view compared to the simulation output. PGCs in the experimental image migrate from the posterior region (top-left of the embryo (posterior region) to the lower-right (gonadal ridge). Experimental images show an increase in Oct-GFP expression, indicating an increase in the abundance of migrating PGCs. Colors of cell types in the model follow those defined in Fig. 3.1.

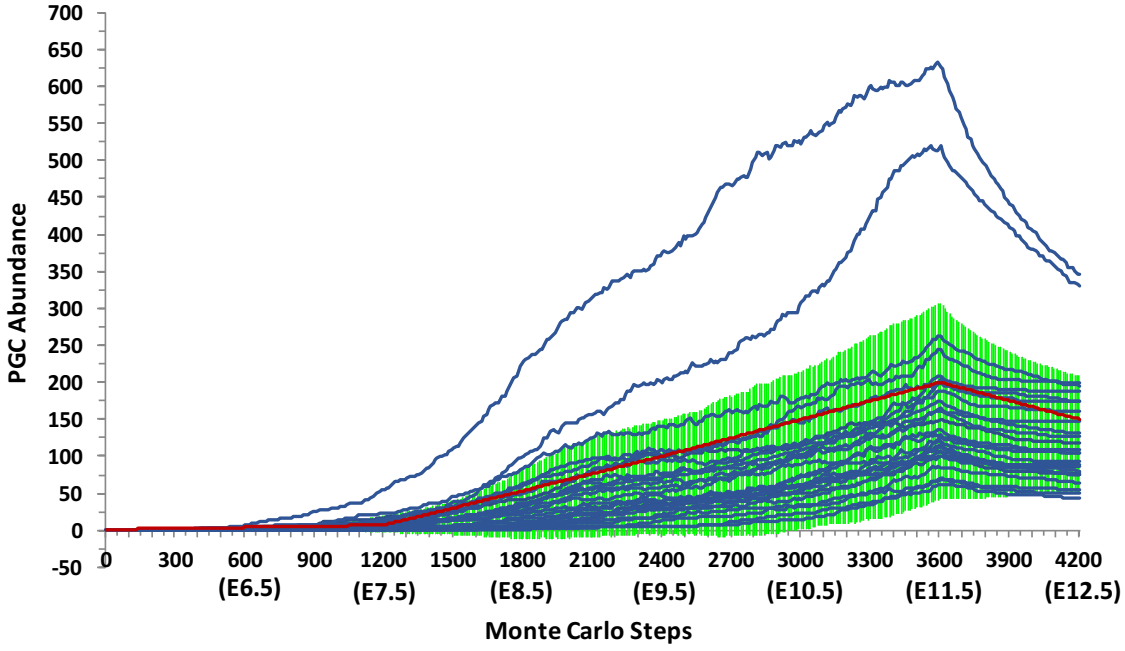


**Fig. 3.6.** The abundance of PGCs in Phase I of the simulation. Each blue line represents one simulation run of 25 total runs. The green area represents one standard deviation from the mean simulation run. Experimental data adjusted to represent one-sixth of the total abundace of PGCs is shown in red.

A) 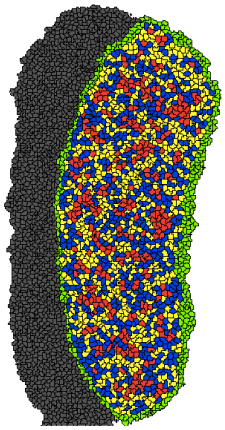

B) 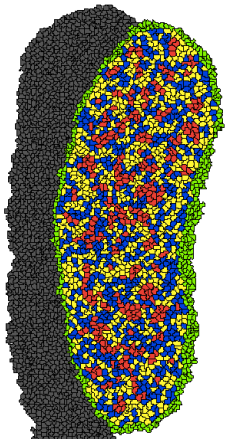

C) 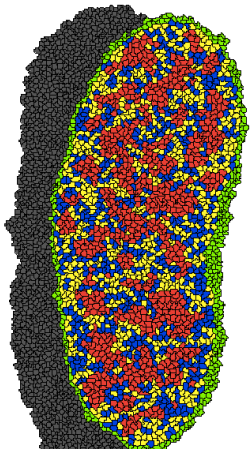

D) 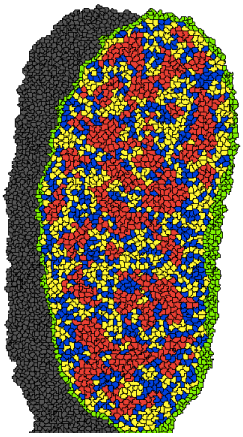

E) 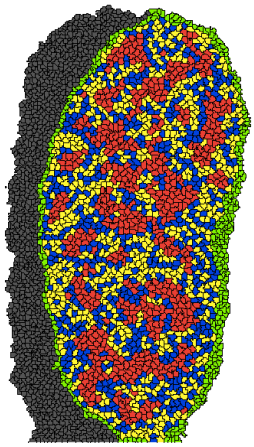

F) 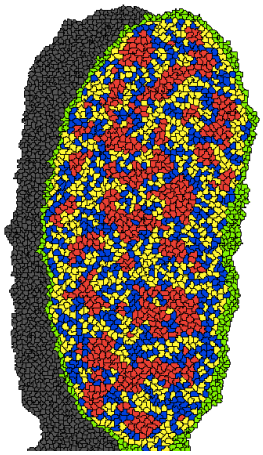

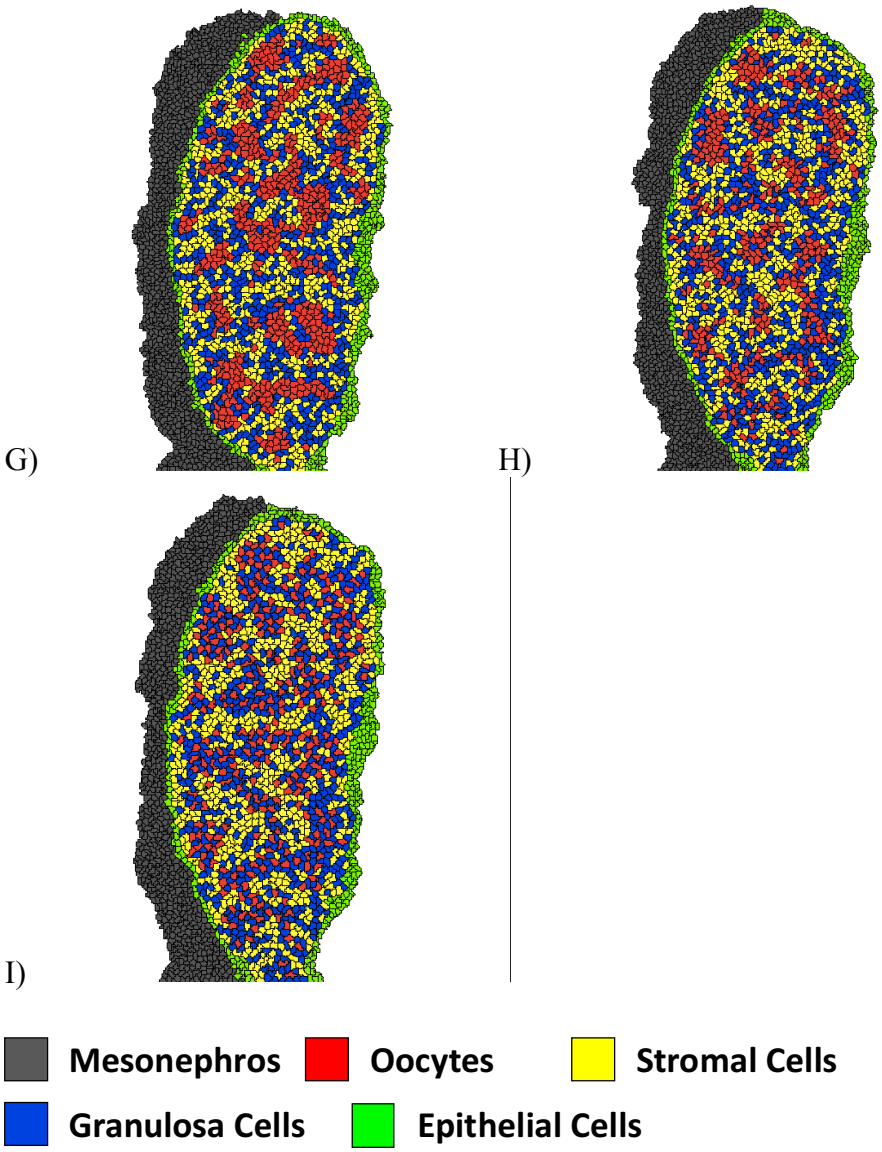


**Fig. 3.7.** Simulation outputs for Phase II at different time points throughout the entire simulation (0-6000 MCS). **A**: 600 MCS (E13.5); **B**: 1200 MCS (E14.5); **C**: 1800 MCS (E15.5); **D**: 2400 MCS (E16.5); **E**: 3000 MCS (E17.5); **F**: 3600 MCS (E18.5); **G**: 4200 MCS (E19.5/P0); **H**: 4800 MCS (P1); **I**: 5400 MCS (P2).

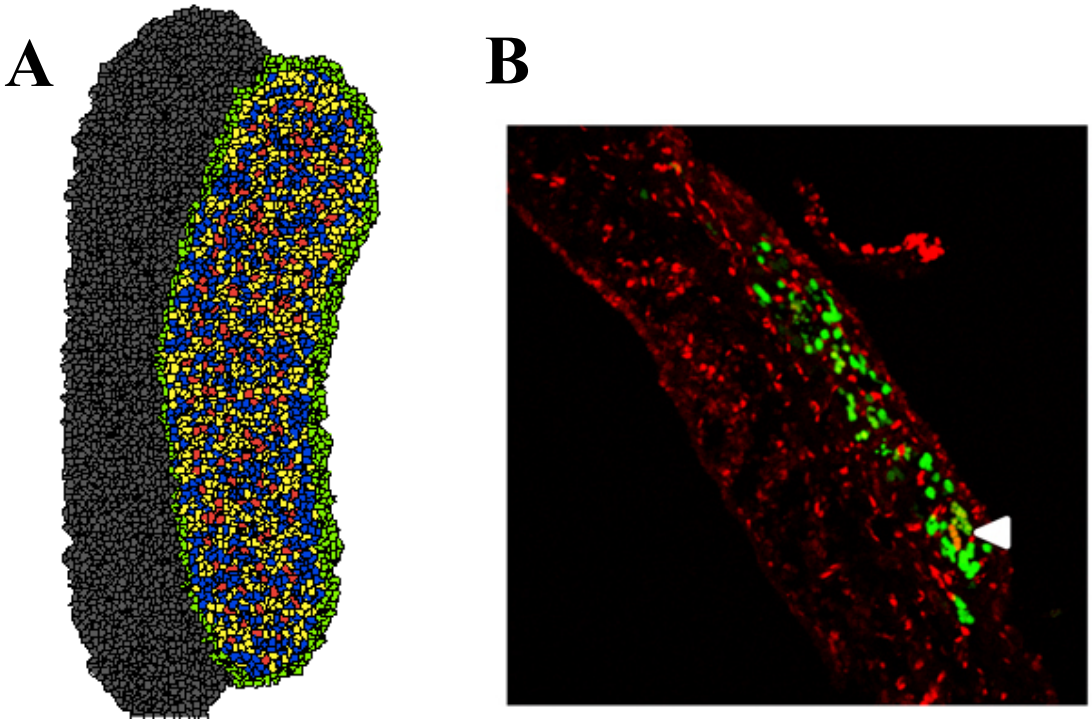


**Fig. 3.8. A)** Phase II simulation output at 0 MCS (E12.5) shows oocytes (red) when they first reach the gonad. Colors of cell types in the model follow those defined in Fig. 3.2**.** **B)** Mouse embryonic ovaries show oocytes through Oct-4-GFP (green) and CCND1 (red) transgene expression from (Heaney et al., 2012) with permission. The mesonephros in the experimental image (section in image showing only cyclin D1 staining) is large compared to the size of the gonad (section with both Oct-4-GFP and cyclin D1 staining).

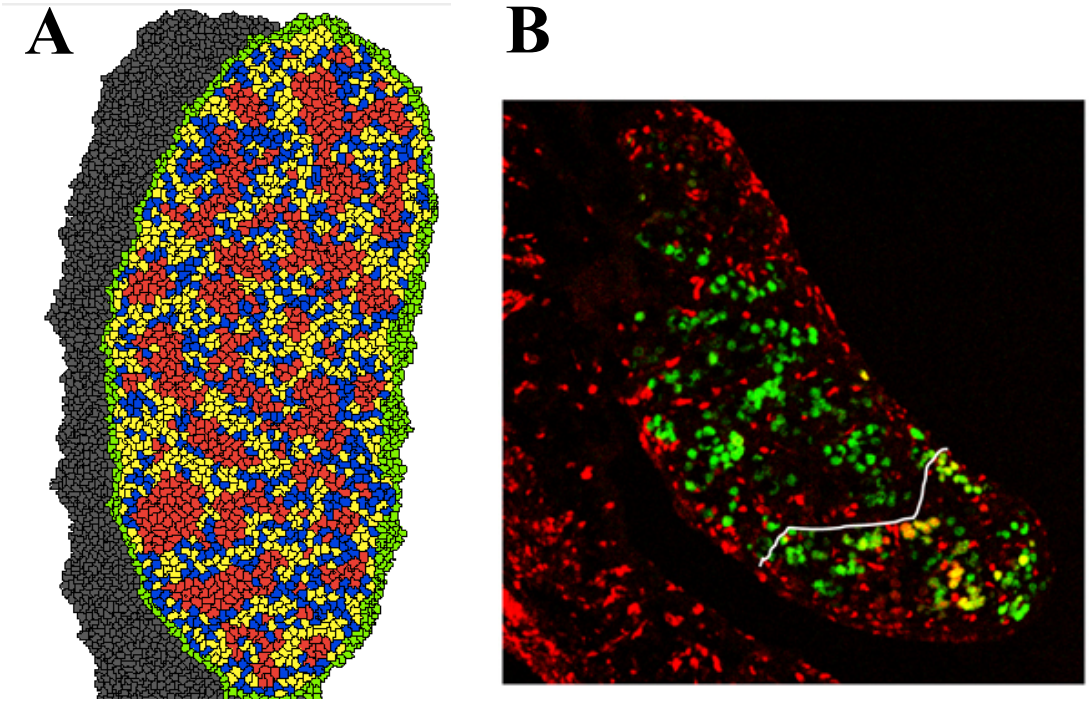


**Fig. 3.9. A)** Phase II simulation output at 4800 MCS (E15.) shows oocytes (red) beginning to from germ cell nests. Colors of cell types in the model follow those defined in Fig. 3.2**. B)** Experimental images of mouse embryos show migration of PGCs from E9.25-E10.5 through Oct-4/*lacZ* transgene expression from (Yeom et al., 1996) with permission.

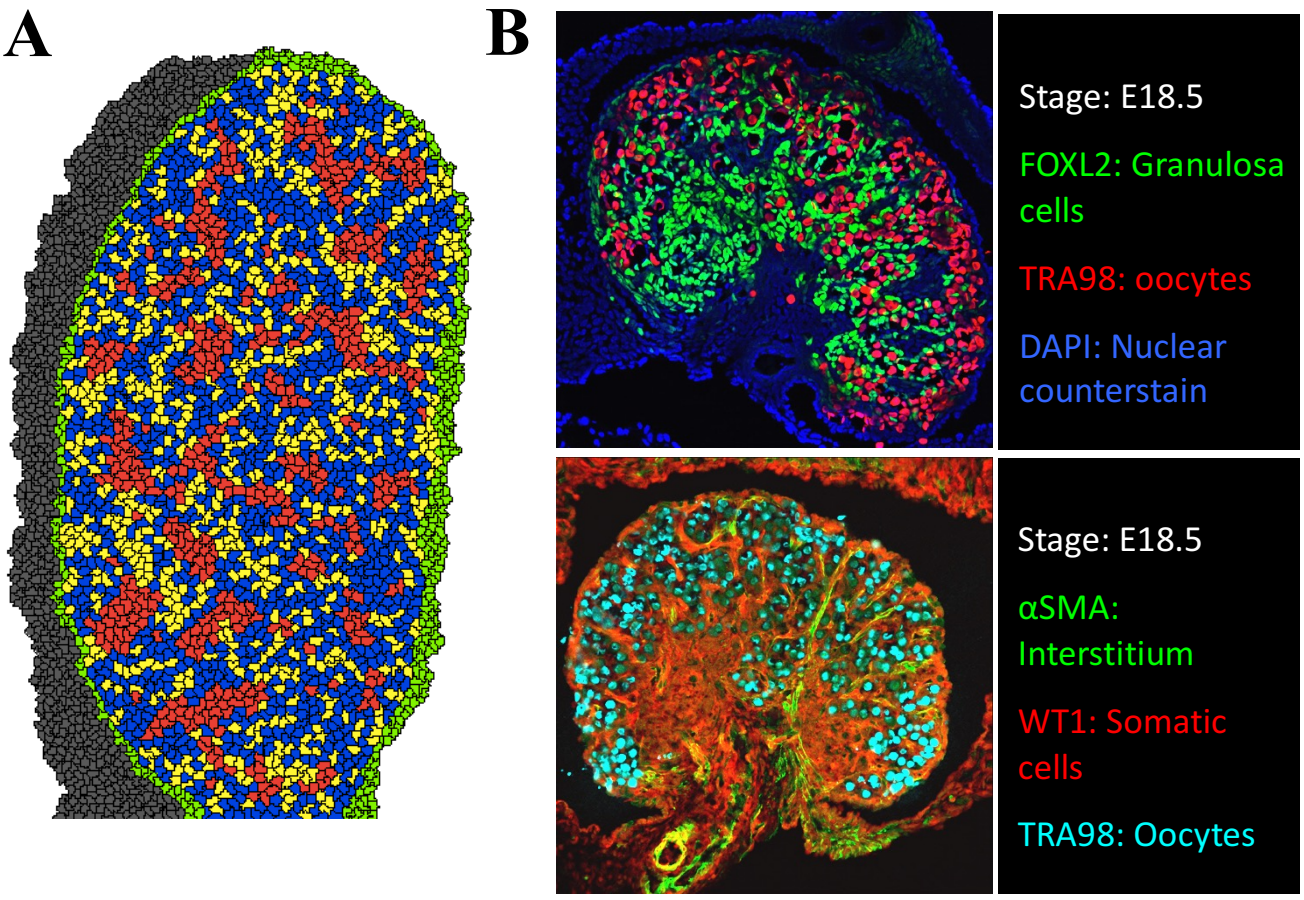


**Fig. 3.10. A)** Phase II simulation output at 3600 MCS (E18.5) shows oocytes (red) in germ cell nest structures. Colors of cell types in the model follow those defined in Fig. 3.2. **B)** Experimental images of a developing mouse ovary show oocytes (red and cyan) in germ cell nests structures (Yao 2015, personal communication). See key for colors of cell types in experimental images.

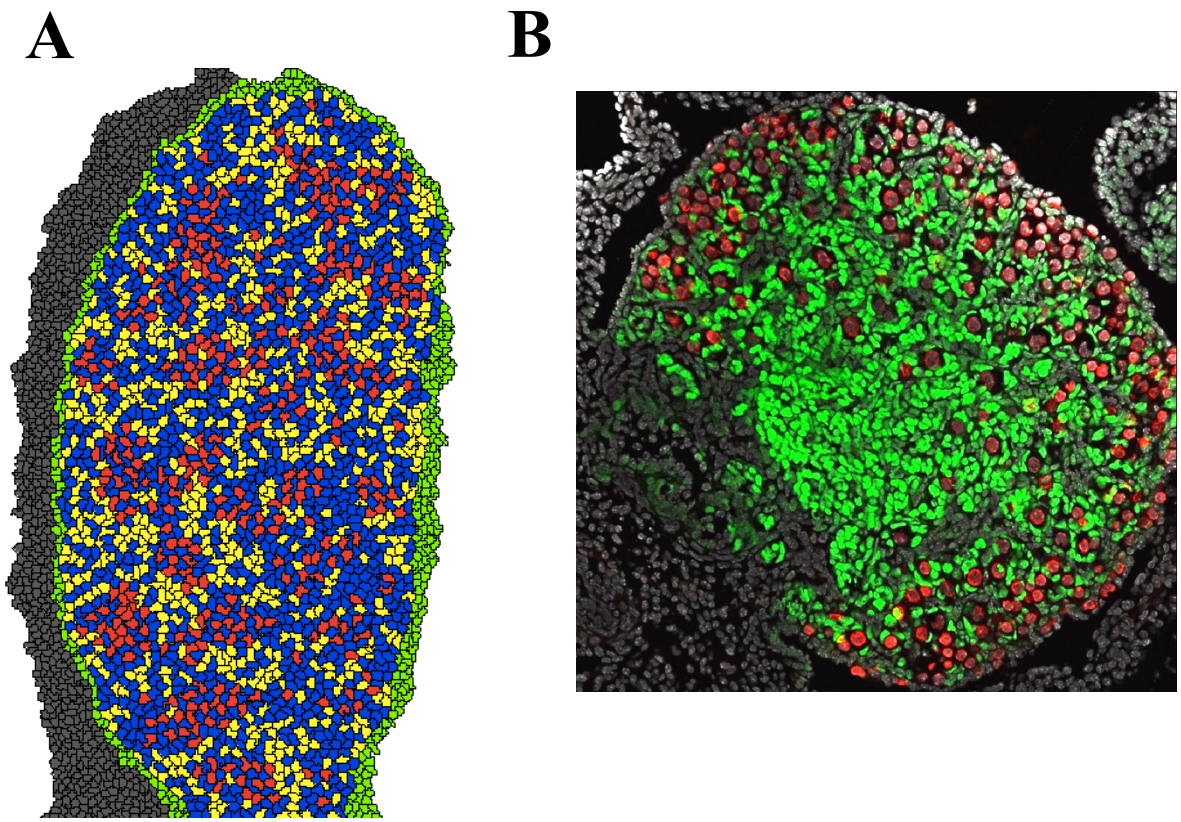


**Fig. 3.11. A)** Phase II simulation output at 4800 MCS (E18.5/P0) shows oocytes (red) beginning to from primordial follicles. Colors of cell types in the model follow those defined in Fig. 3.2. **B)** An experimental image of a developing mouse ovary at birth (P0) show the breakdown of germ cell nests and the formation of primordial follicles (Yao 2015, personal communication). Cellular staining: oocytes (red) through TRA98, granulosa cells (green) through FOXL2, and other cell types (grey) through DAPI.

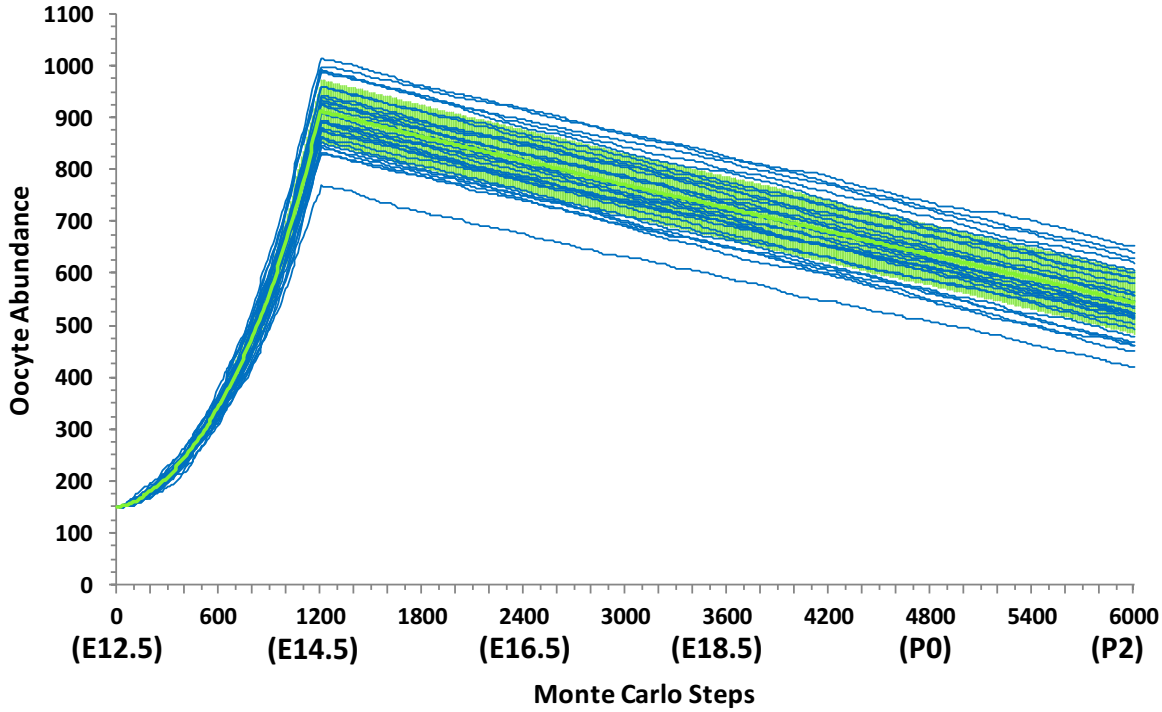


**Fig. 3.12.** The abundance of oocytes in Phase II of the simulation. Each blue line represents one simulation run of 25 total runs. The green area represents one standard deviation from the mean simulation run.

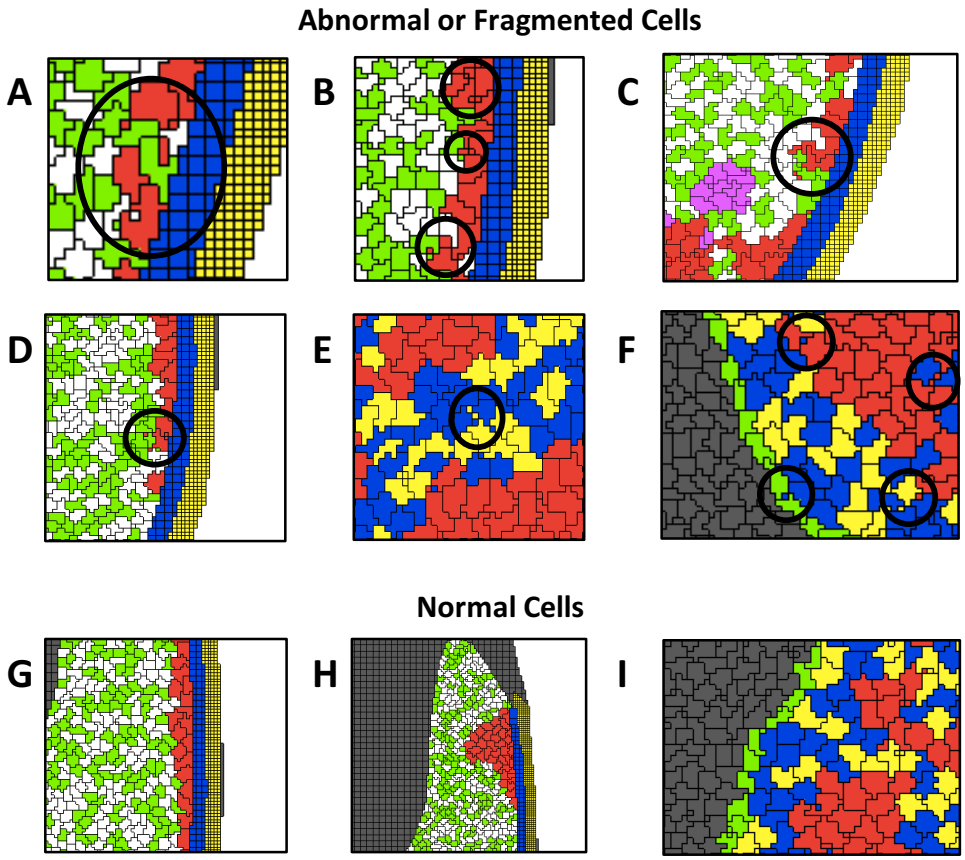


**Fig. 4.1.** Parameter sensitivity in Phase I and Phase II of the model were analyzed based on the appearance and frequency of abnormal cell structures. A-F represent examples of abnormal and/or fragmented cells. Black circles highlight the abnormal cell or cell fragments. G-I show cells in the simulation behaving under normal conditions.

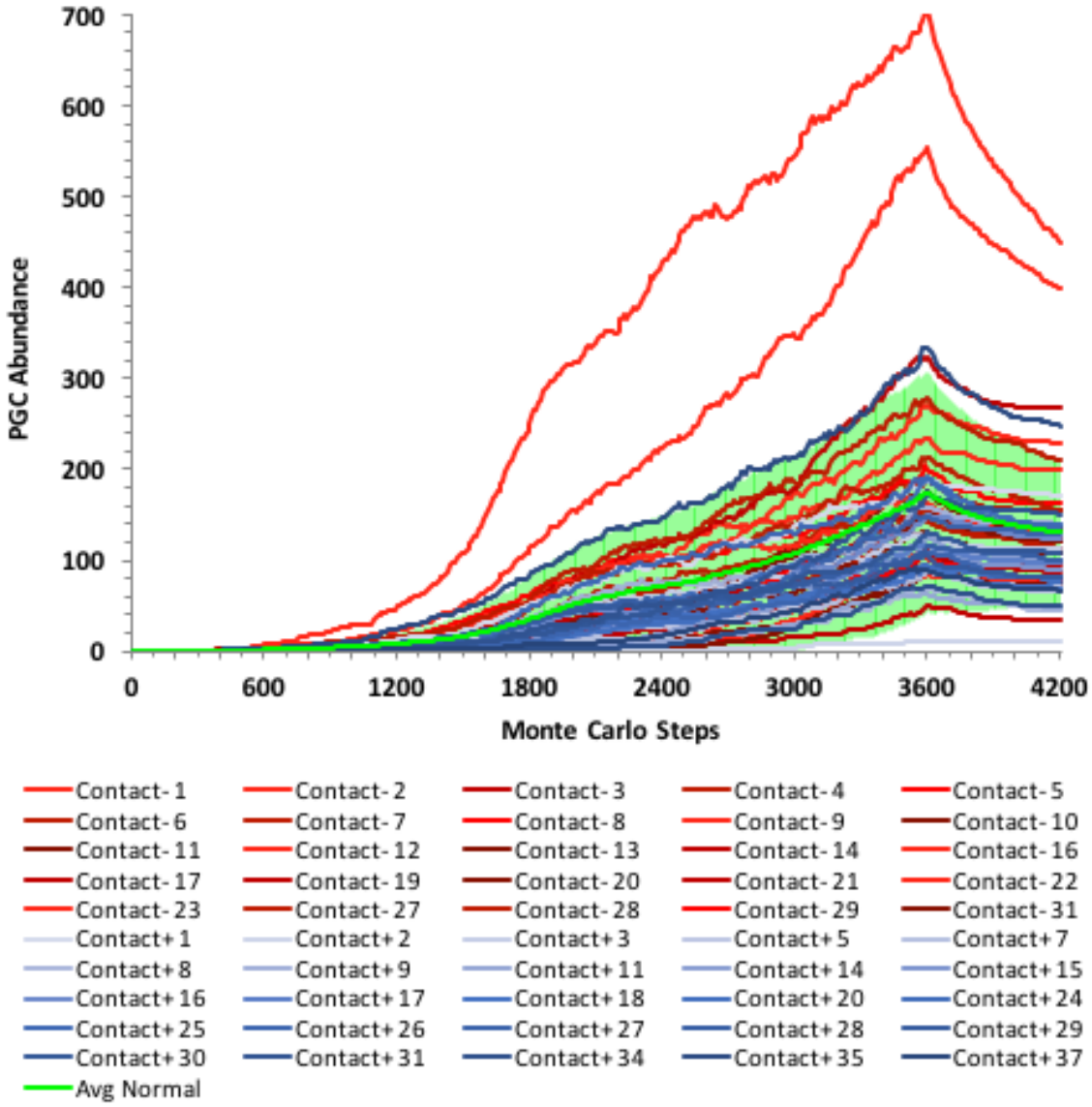


**Fig. 4.2**. Sensitivity analysis for the contact energies ($J_{\tau\text{-}\tau}$), showing the abundance of PGCs in Phase I of the early ovarian development model. Each line represents one trial simulation with a 10% decrease (reds) or a 10% increase (blues) to the original parameter value. The green line shows the average ± one standard deviation of all simulations run under normal conditions.

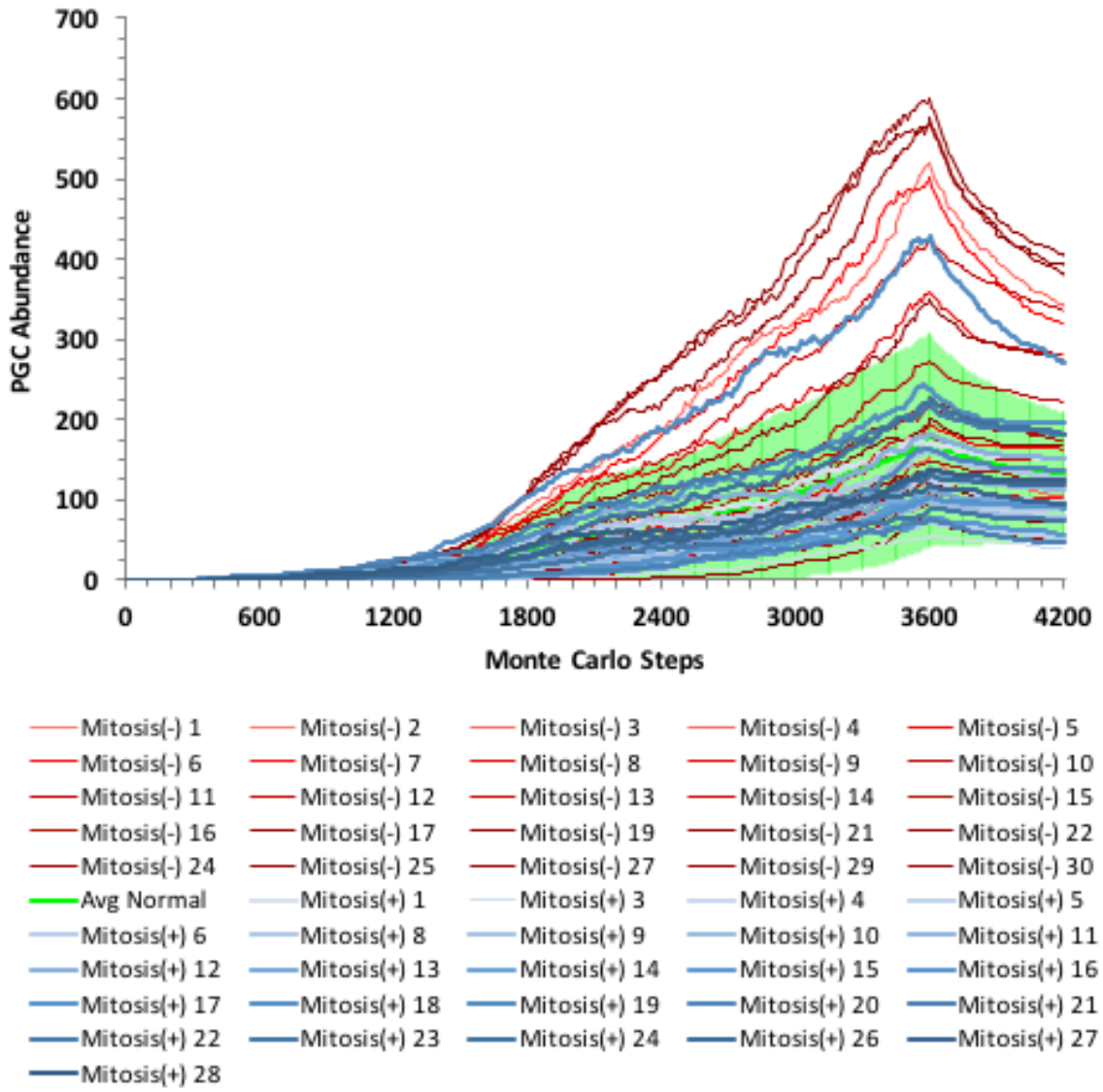


**Fig. 4.3**. Sensitivity analysis for the mitotic rate of PGCs ($m_{\tau 1}$), showing the abundance of PGCs in Phase I of the early ovarian development model. Each line represents one trial simulation with a 10% decrease (reds) or a 10% increase (blues) to the original parameter value. The green line shows the average ± one standard deviation of all simulations run under normal conditions.

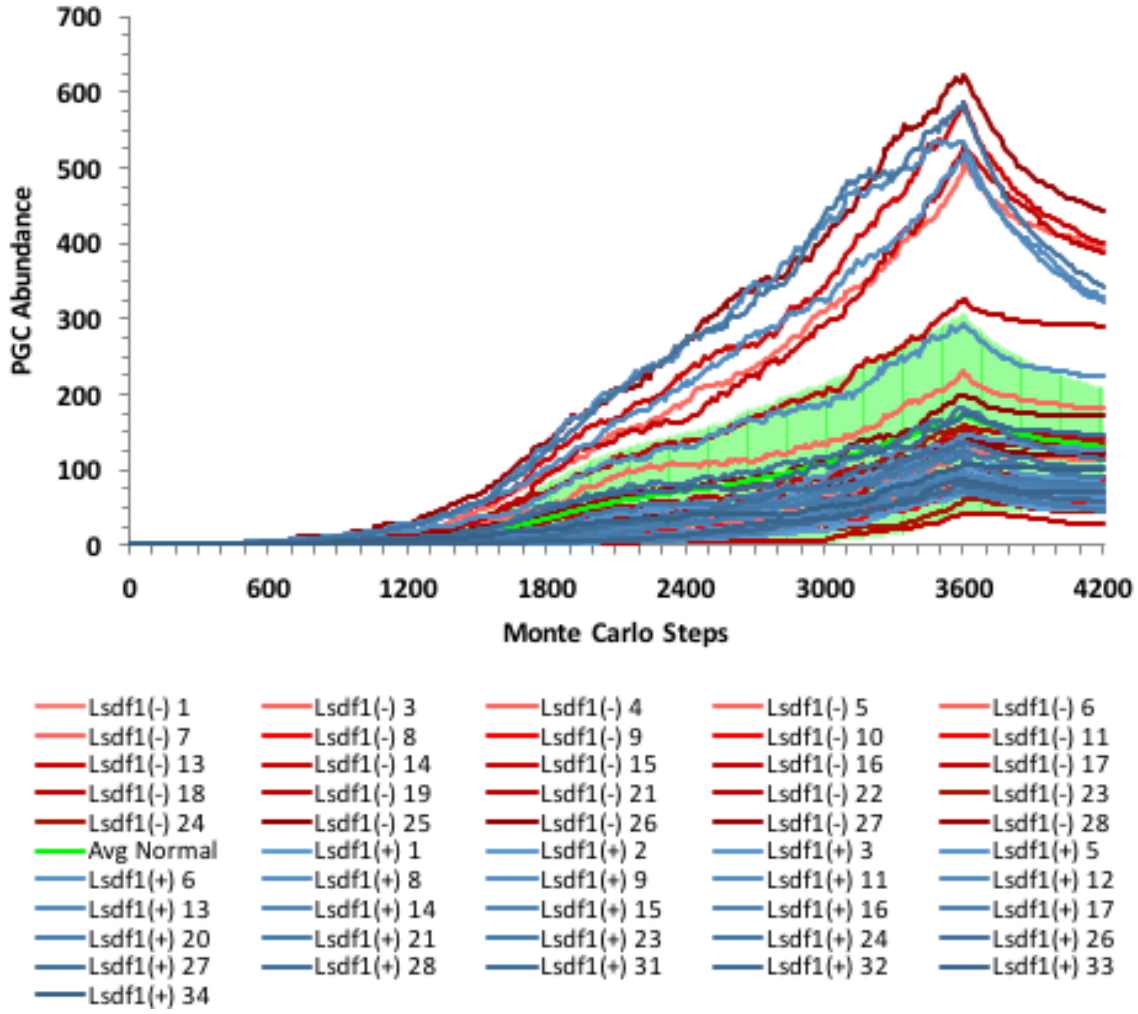


**Fig. 4.4**. Sensitivity analysis for the SDF1 lambda chemotaxis ($\lambda_{SDF1(\tau 1)}$), showing the abundance of PGCs in Phase I of the early ovarian development model. Each line represents one trial simulation with a 10% decrease (reds) or a 10% increase (blues) to the original parameter value. The green line shows the average ± one standard deviation of all simulations run under normal conditions.

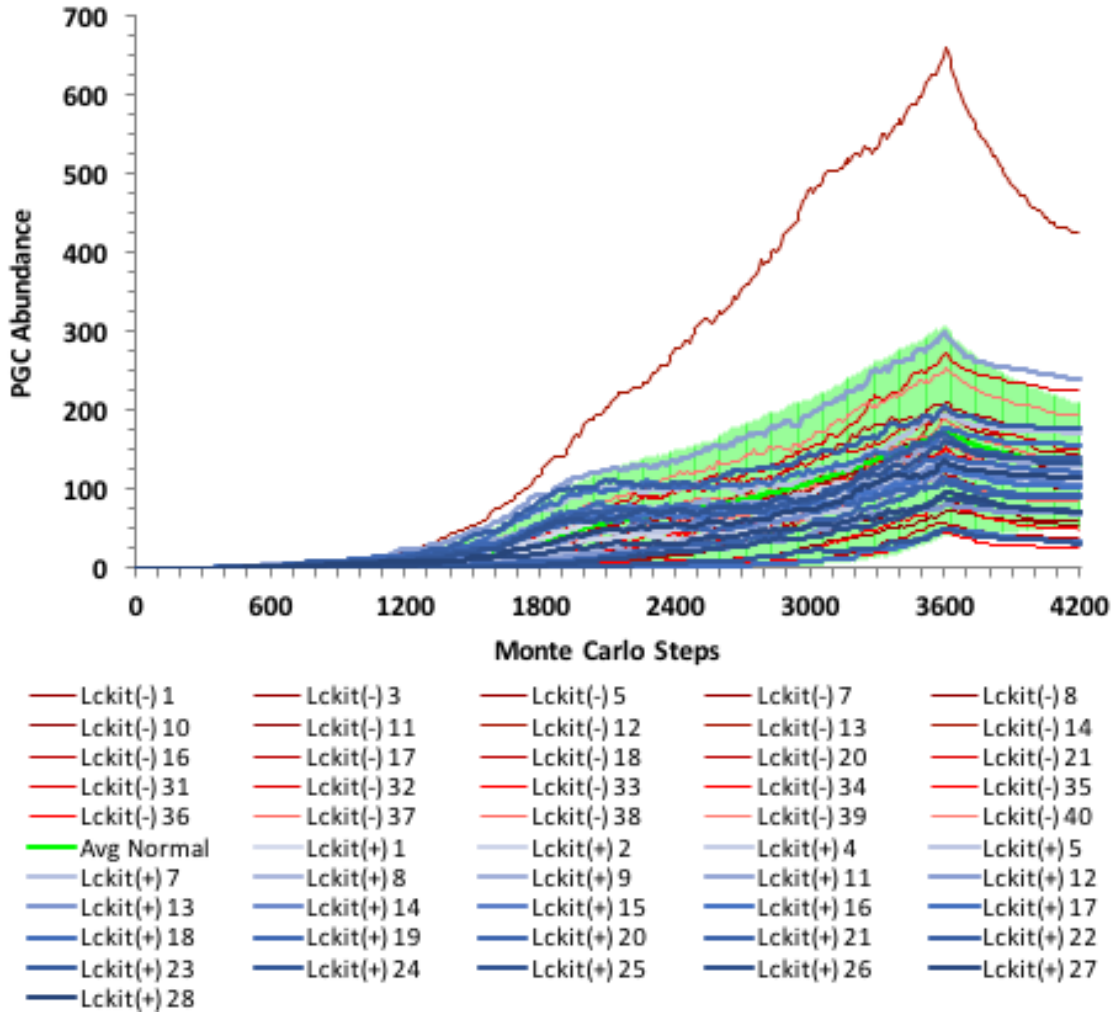


**Fig. 4.5**. Sensitivity analysis for the KIT lambda chemotaxis ($\lambda_{KIT(\tau 1)}$), showing the abundance of PGCs in Phase I of the early ovarian development model. Each line represents one trial simulation with a 10% decrease (reds) or a 10% increase (blues) to the original parameter value. The green line shows the average ± one standard deviation of all simulations run under normal conditions.

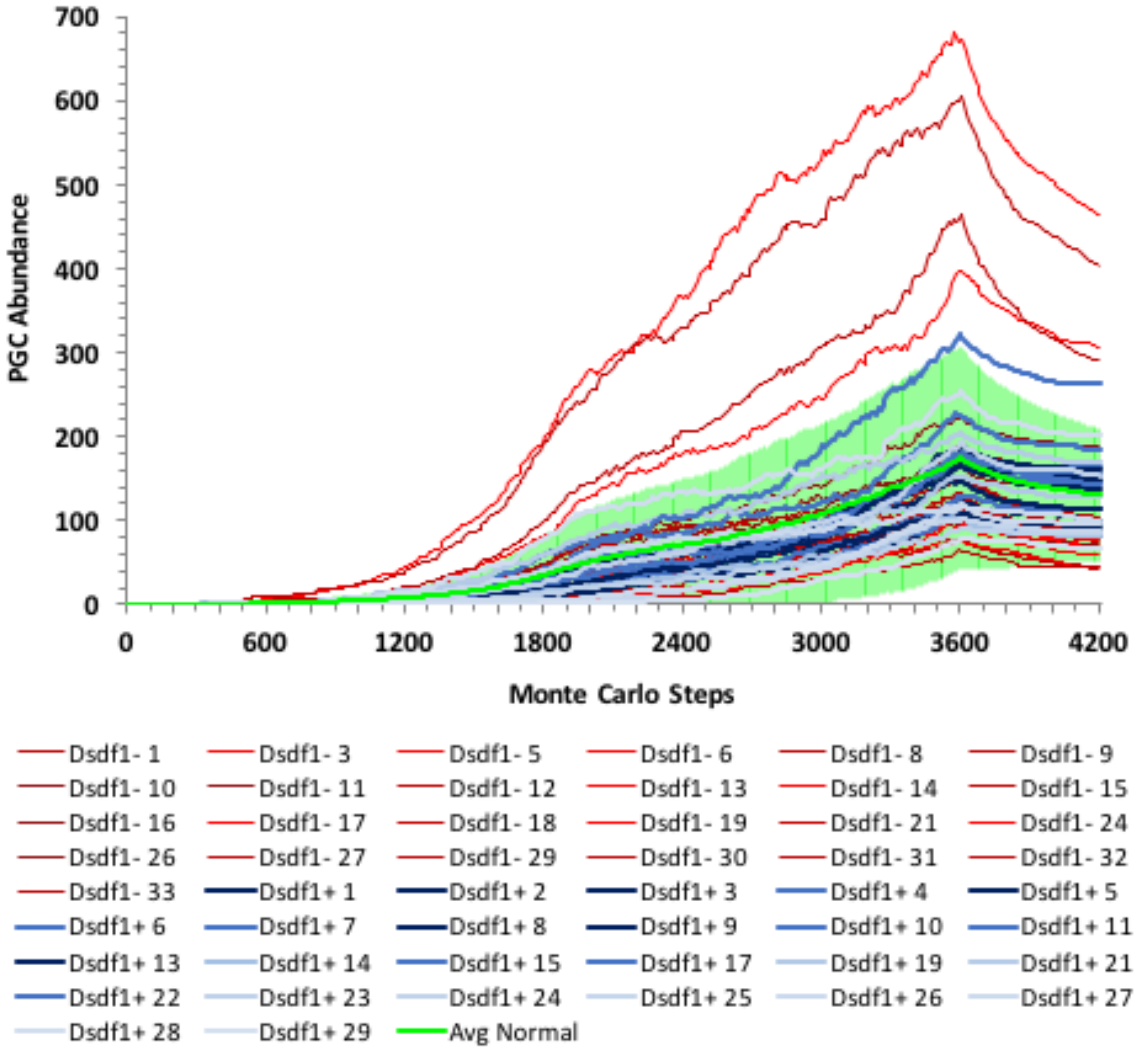


**Fig. 4.6.** Sensitivity analysis for the diffusion rate of SDF1 ($D_{SDF1}$), showing the abundance of PGCs in Phase I of the early ovarian development model. Each line represents one trial simulation with a 10% decrease (reds) or a 10% increase (blues) to the original parameter value. The green line shows the average ± one standard deviation of all simulations run under normal conditions.

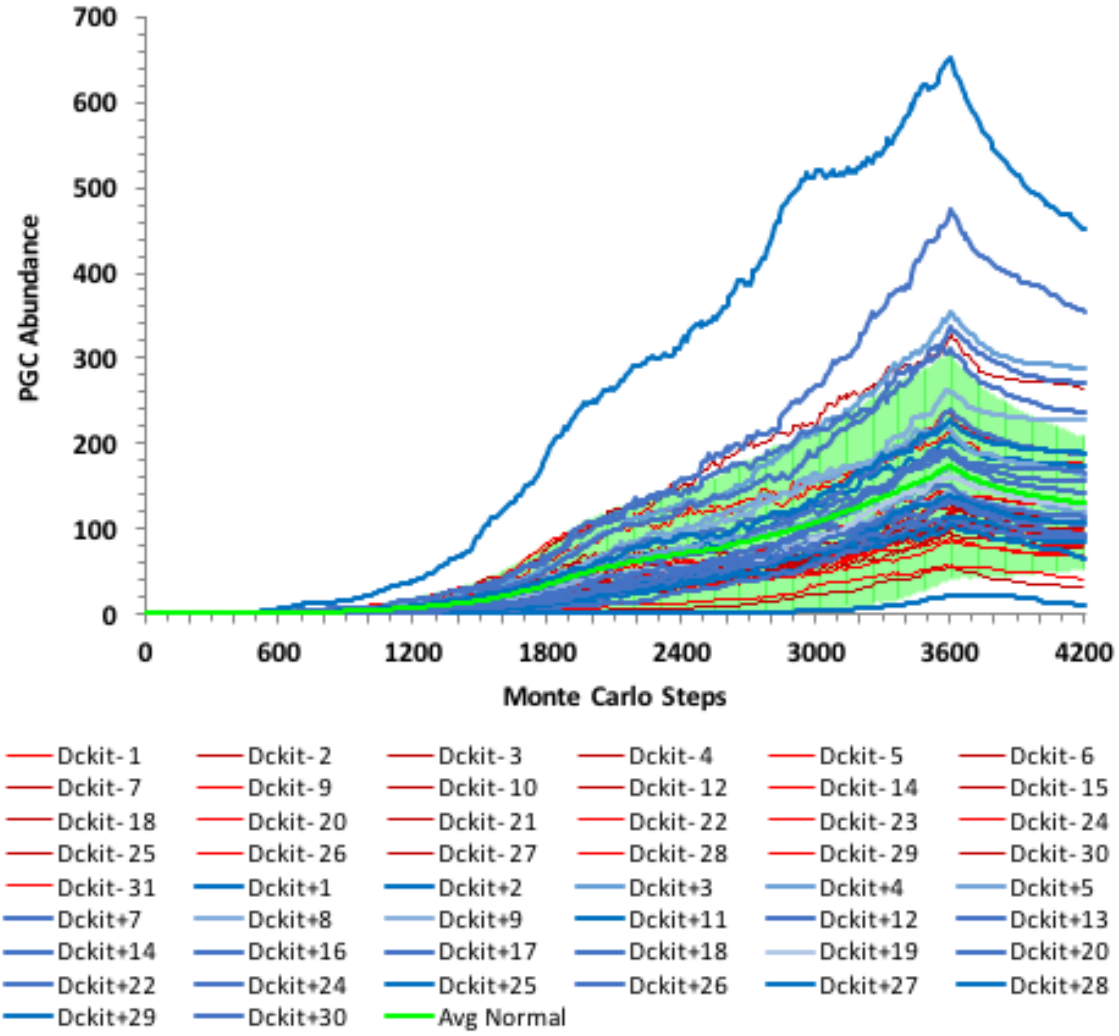


**Fig. 4.7.** Sensitivity analysis for the diffusion rate of KIT ($D_{KIT}$), showing the abundance of PGCs in Phase I of the early ovarian development model. Each line represents one trial simulation with a 10% decrease (reds) or a 10% increase (blues) to the original parameter value. The green line shows the average ± one standard deviation of all simulations run under normal conditions.

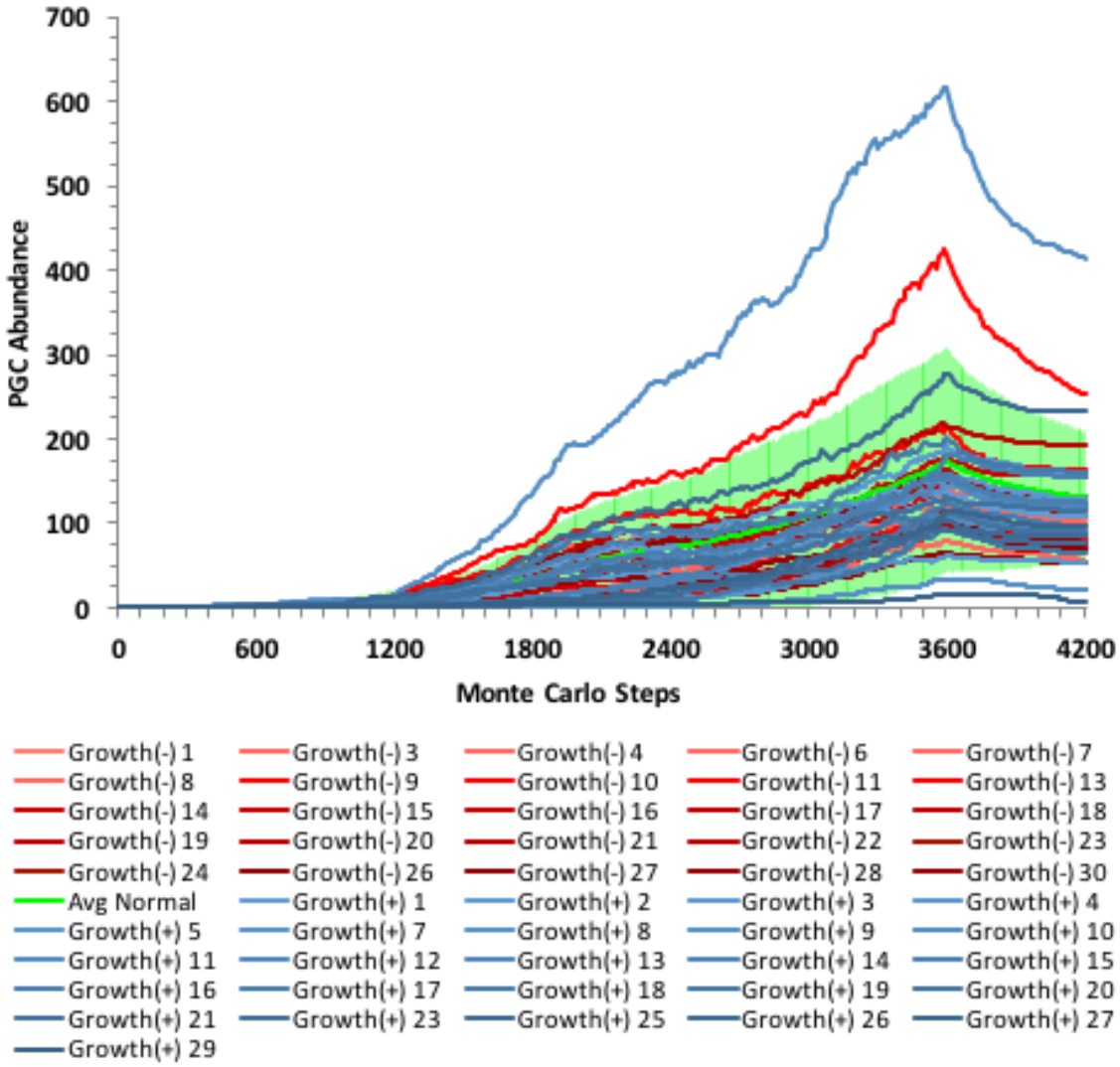


**Fig. 4.8**. Sensitivity analysis for the growth rate of PGCs ($g_{\tau 1}$), showing the abundance of PGCs in Phase I of the early ovarian development model. Each line represents one trial simulation with a 10% decrease (reds) or a 10% increase (blues) to the original parameter value. The green line shows the average ± one standard deviation of all simulations run under normal conditions.

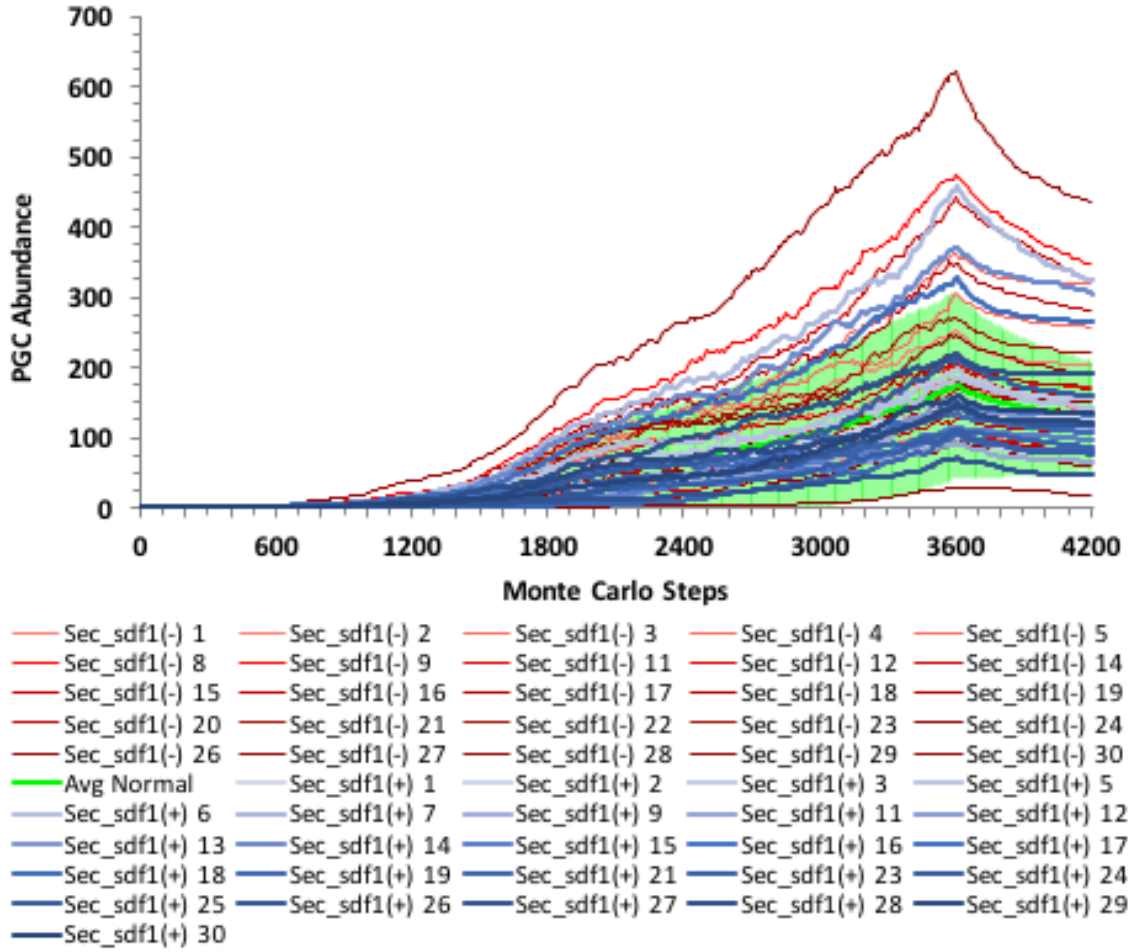


**Fig. 4.9**. Sensitivity analysis for the secretion rate of SDF1 ($\Theta_{SDF1}$), showing the abundance of PGCs in Phase I of the early ovarian development model. Each line represents one trial simulation with a 10% decrease (reds) or a 10% increase (blues) to the original parameter value. The green line shows the average ± one standard deviation of all simulations run under normal conditions.

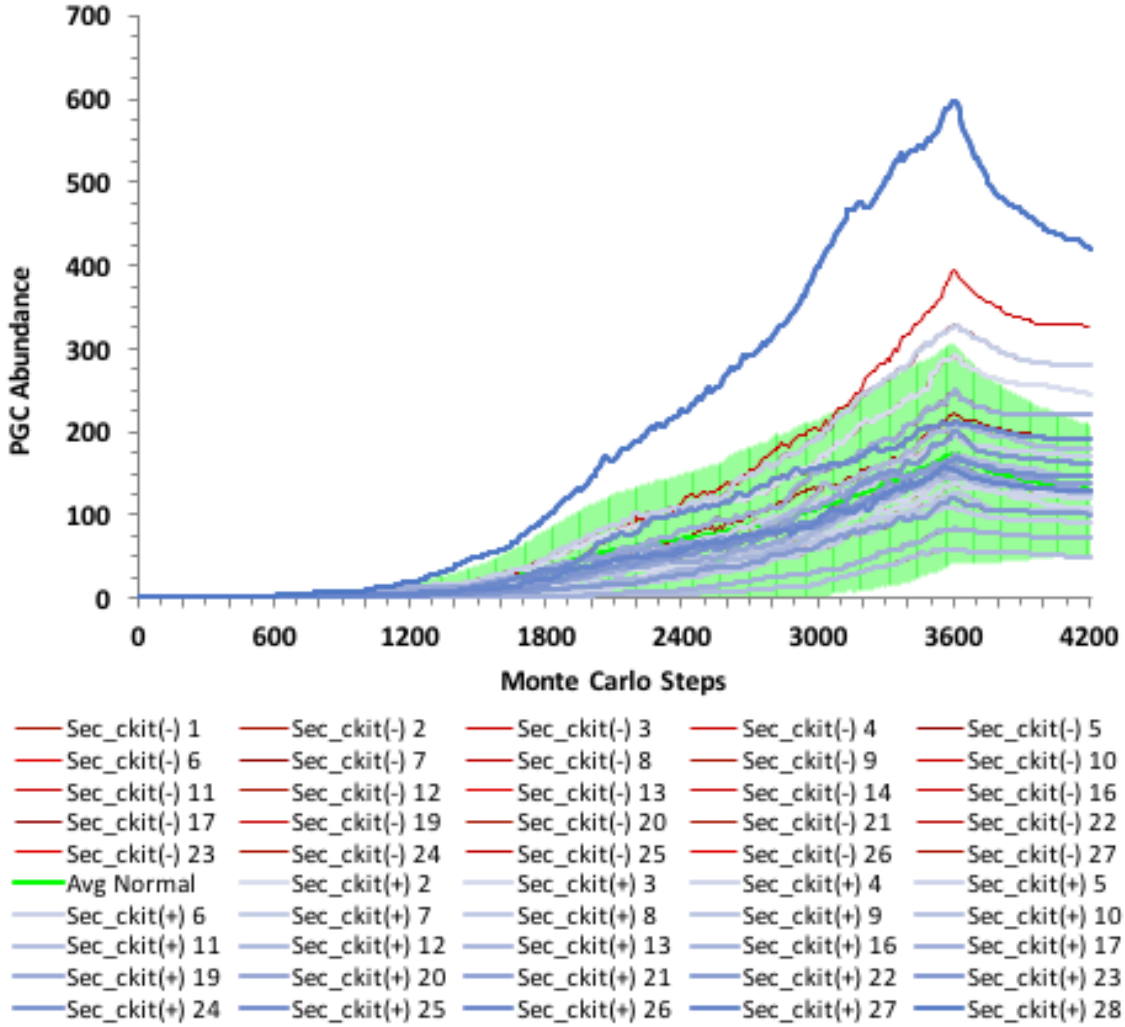


**Fig. 4.10**. Sensitivity analysis for the secretion rate of KIT ($\Theta_{KIT}$), showing the abundance of PGCs in Phase I of the early ovarian development model. Each line represents one trial simulation with a 10% decrease (reds) or a 10% increase (blues) to the original parameter value. The green line shows the average ± one standard deviation of all simulations run under normal conditions.

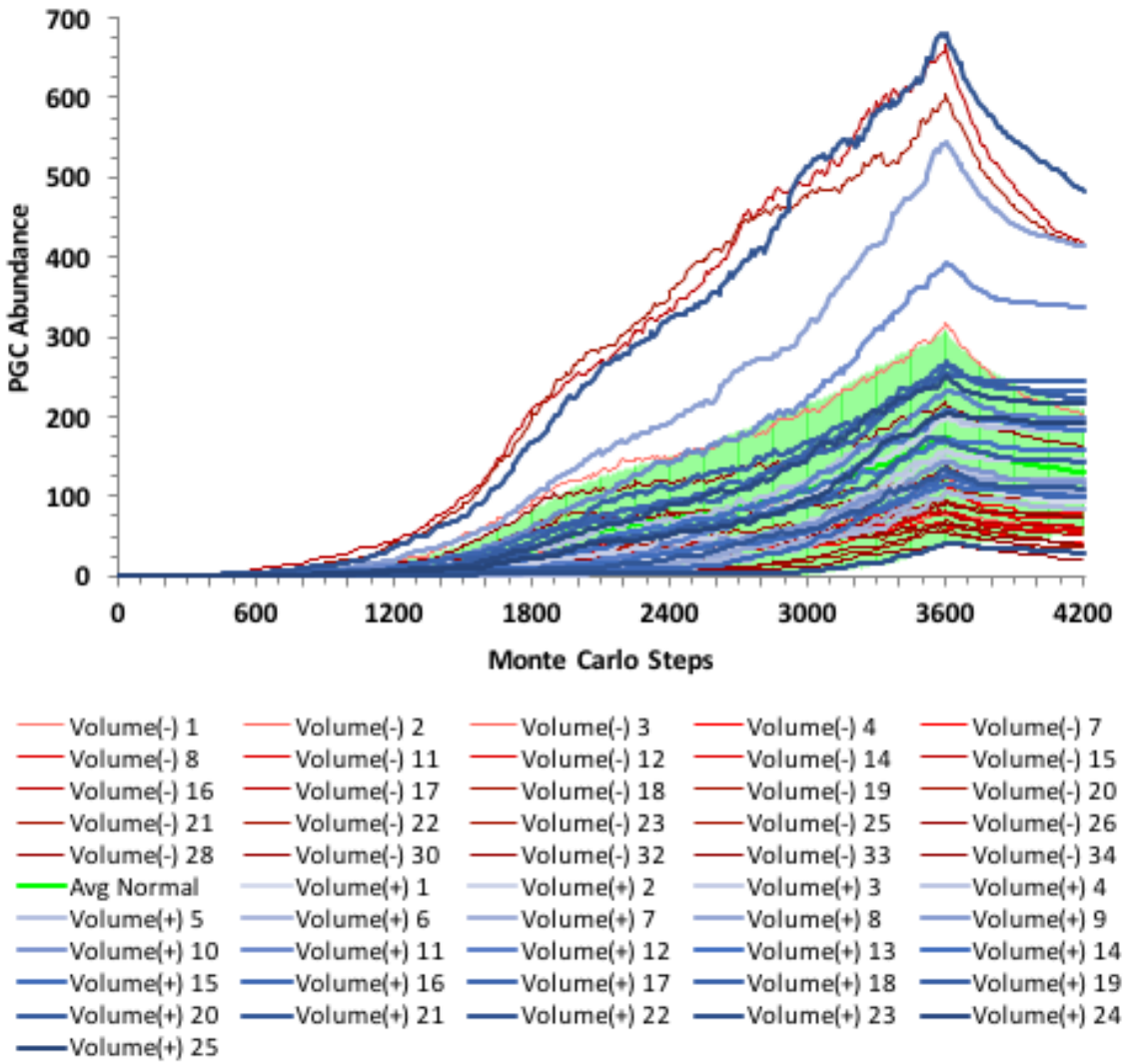


**Fig. 4.11**. Sensitivity analysis for the target volume ($V_\tau$), showing the abundance of PGCs in Phase I of the early ovarian development model. Each line represents one trial simulation with a 10% decrease (reds) or a 10% increase (blues) to the original parameter value. The green line shows the average ± one standard deviation of all simulations run under normal conditions.

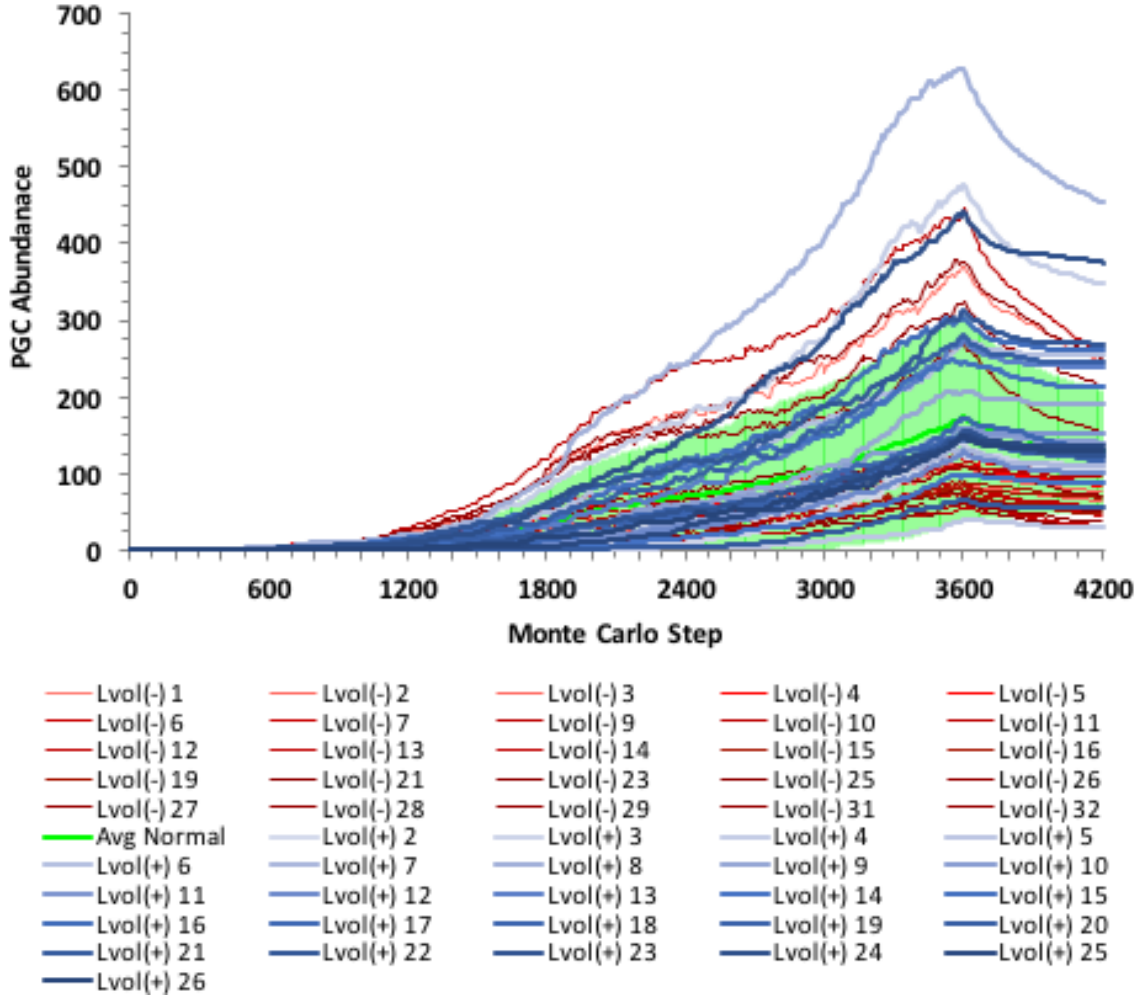


**Fig. 4.12.** Sensitivity analysis for the lambda volume ($\lambda_{V\tau}$), showing the abundance of PGCs in Phase I of the early ovarian development model. Each line represents one trial simulation with a 10% decrease (reds) or a 10% increase (blues) to the original parameter value. The green line shows the average ± one standard deviation of all simulations run under normal conditions.

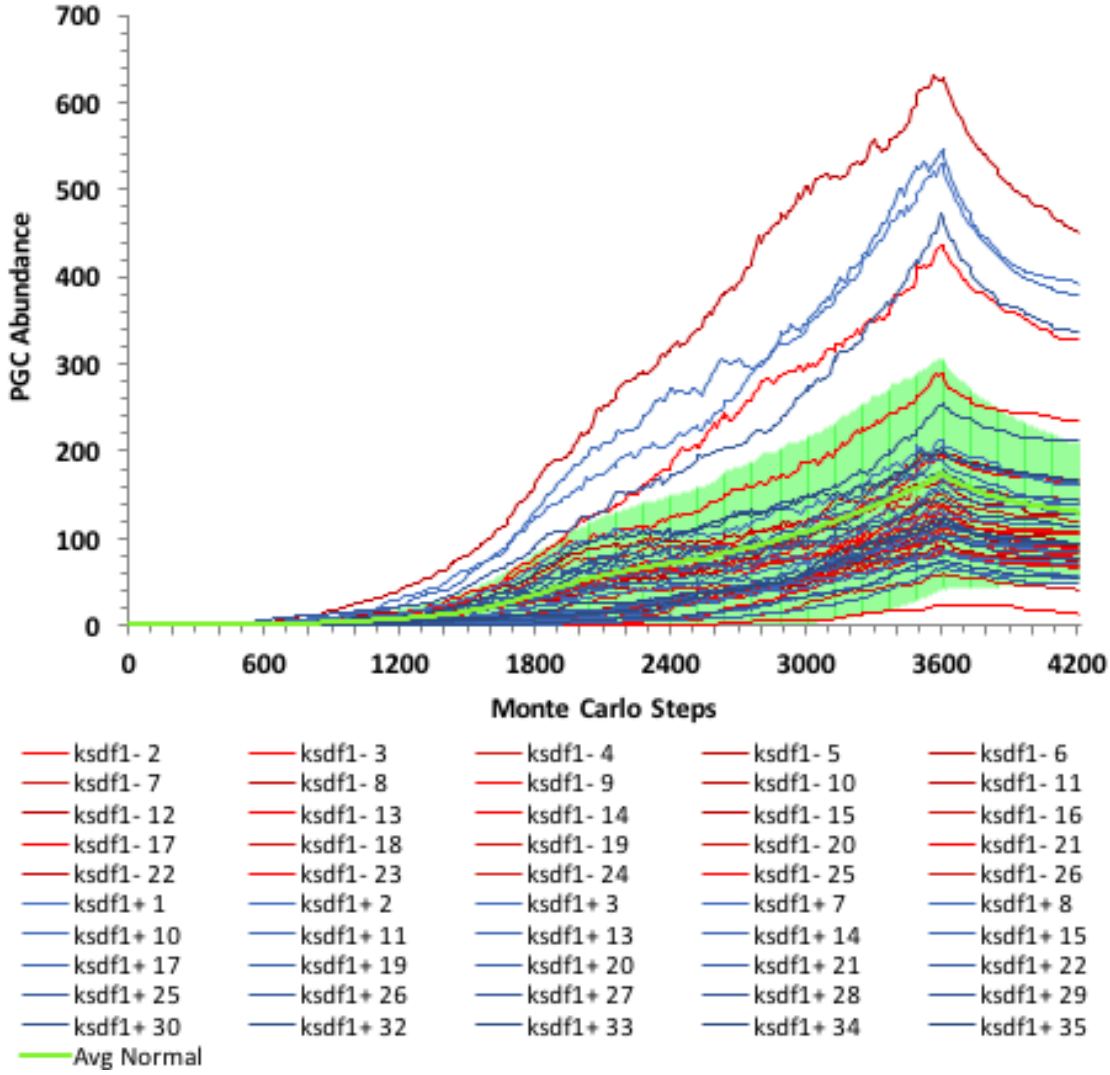


**Fig. 4.13.** Sensitivity analysis for the decay rate of SDF1 ($k_{SDF1}$), showing the abundance of PGCs in Phase I of the early ovarian development model. Each line represents one trial simulation with a 10% decrease (reds) or a 10% increase (blues) to the original parameter value. The green line shows the average ± one standard deviation of all simulations run under normal conditions.

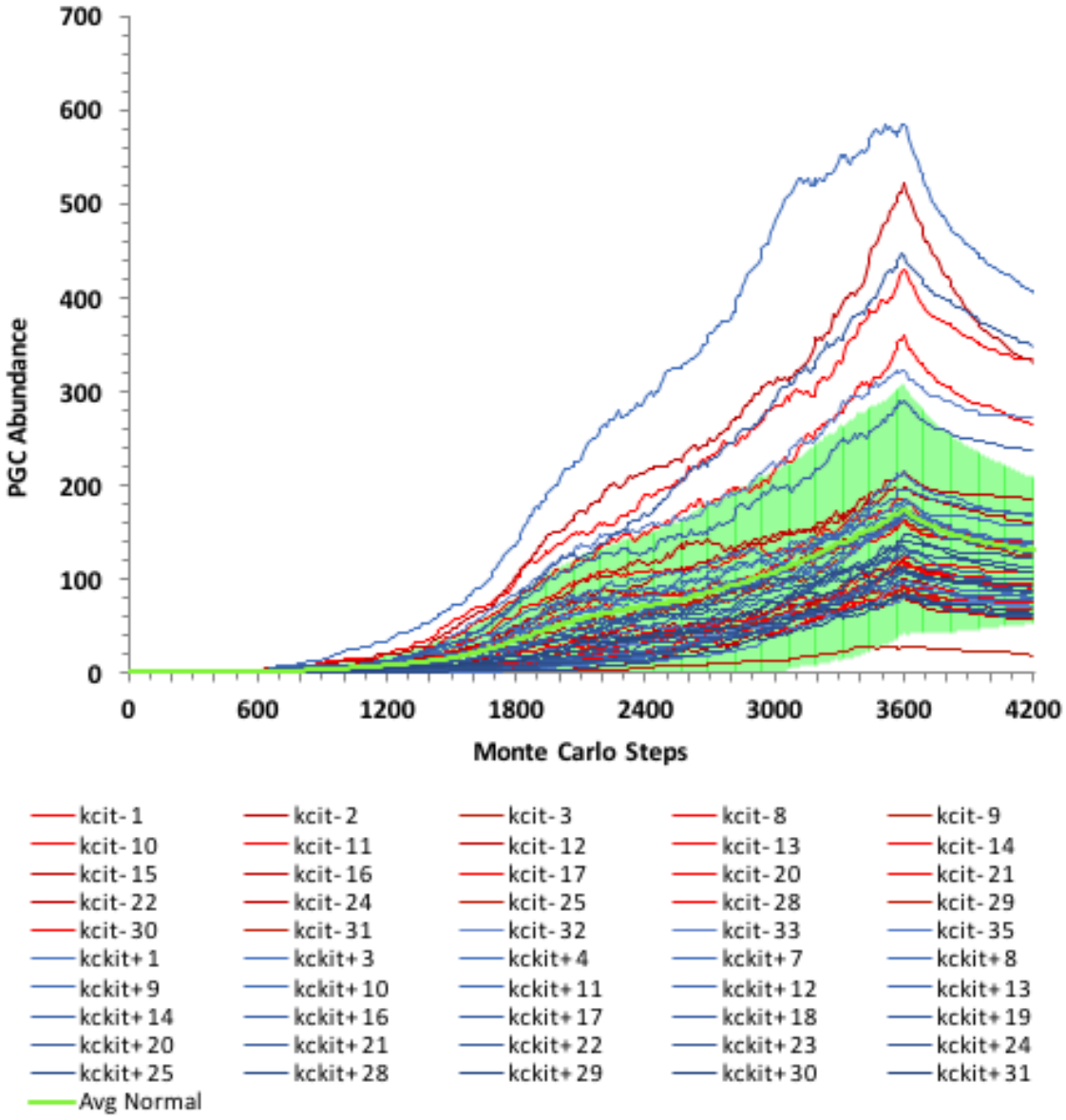


**Fig. 4.14.** Sensitivity analysis for the decay rate of KIT ($k_{KIT}$), showing the abundance of PGCs in Phase I of the early ovarian development model. Each line represents one trial simulation with a 10% decrease (reds) or a 10% increase (blues) to the original parameter value. The green line shows the average ± one standard deviation of all simulations run under normal conditions.

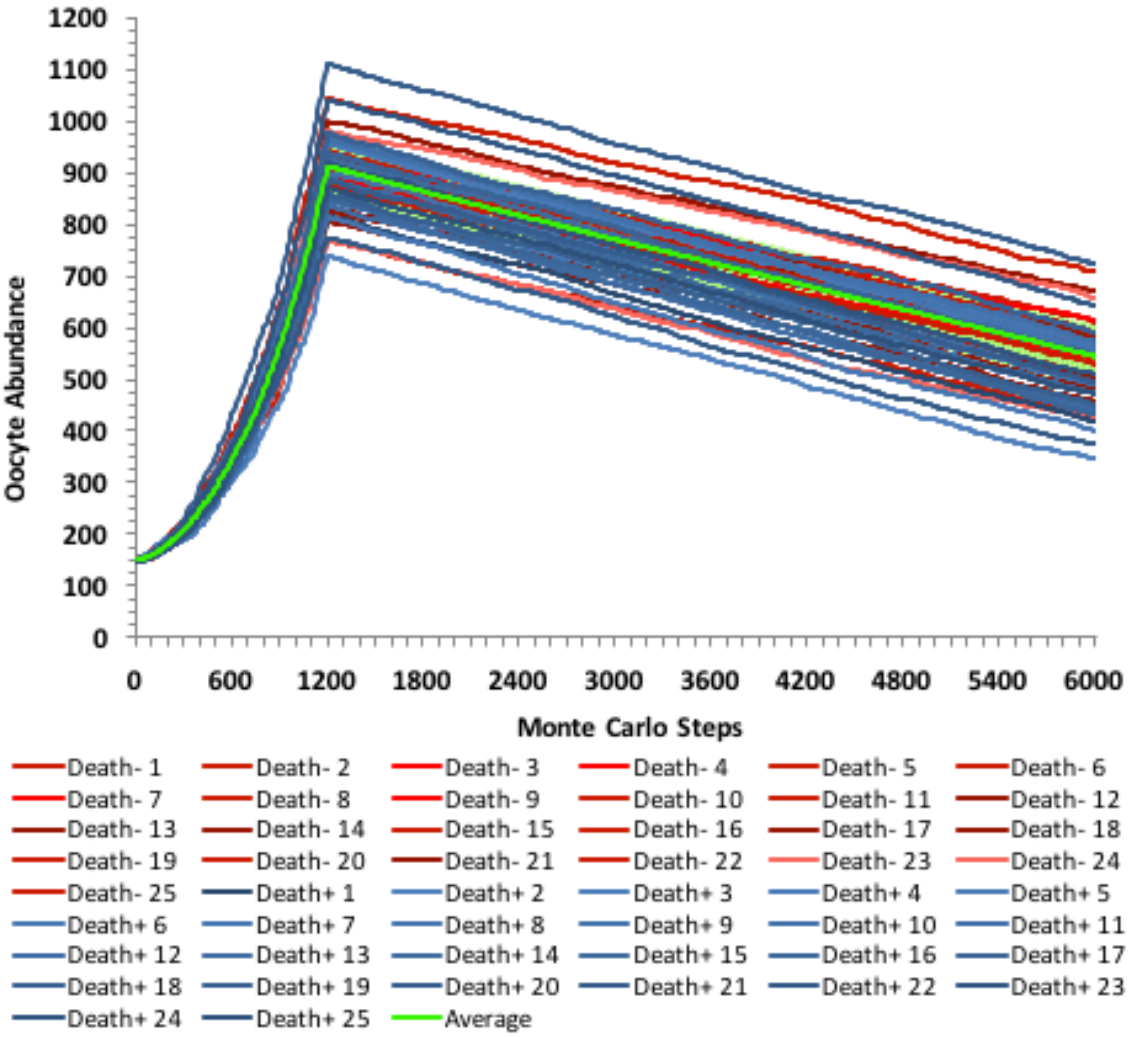


**Fig. 4.15.** Sensitivity analysis for the death rate ($d_{\tau'}$), showing the abundance of oocytes in Phase II of the early ovarian development model. Each line represents one trial simulation with a 10% decrease (reds) or a 10% increase (blues) to the original parameter value. The green line shows the average ± one standard deviation of all simulations run under normal conditions.

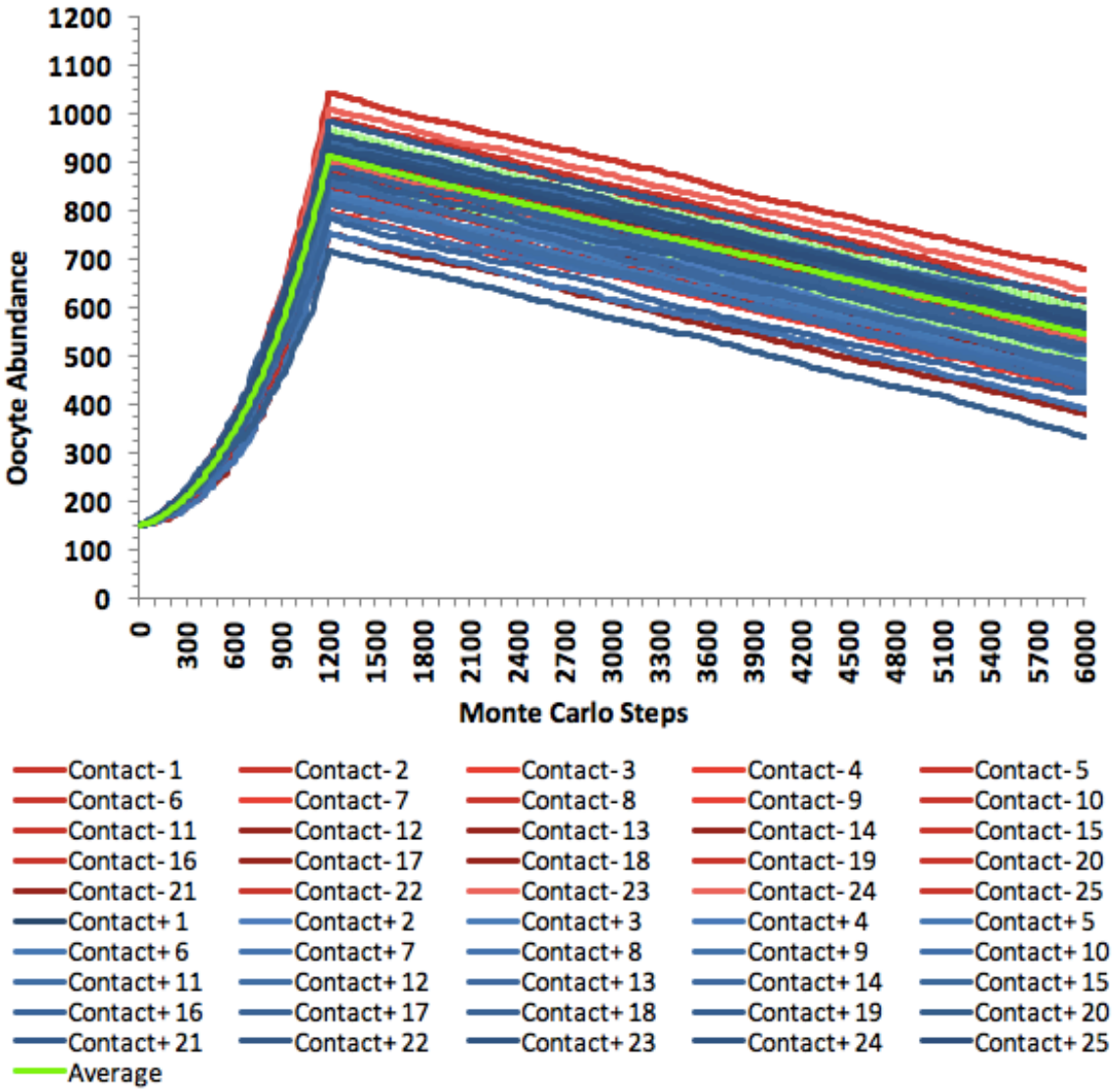


**Fig. 4.16.** Sensitivity analysis for the contact energies ($J_{\tau'\text{-}\tau'}$), showing the abundance of oocytes in Phase II of the early ovarian development model. Each line represents one trial simulation with a 10% decrease (reds) or a 10% increase (blues) to the original parameter value. The green line shows the average ± one standard deviation of all simulations run under normal conditions.

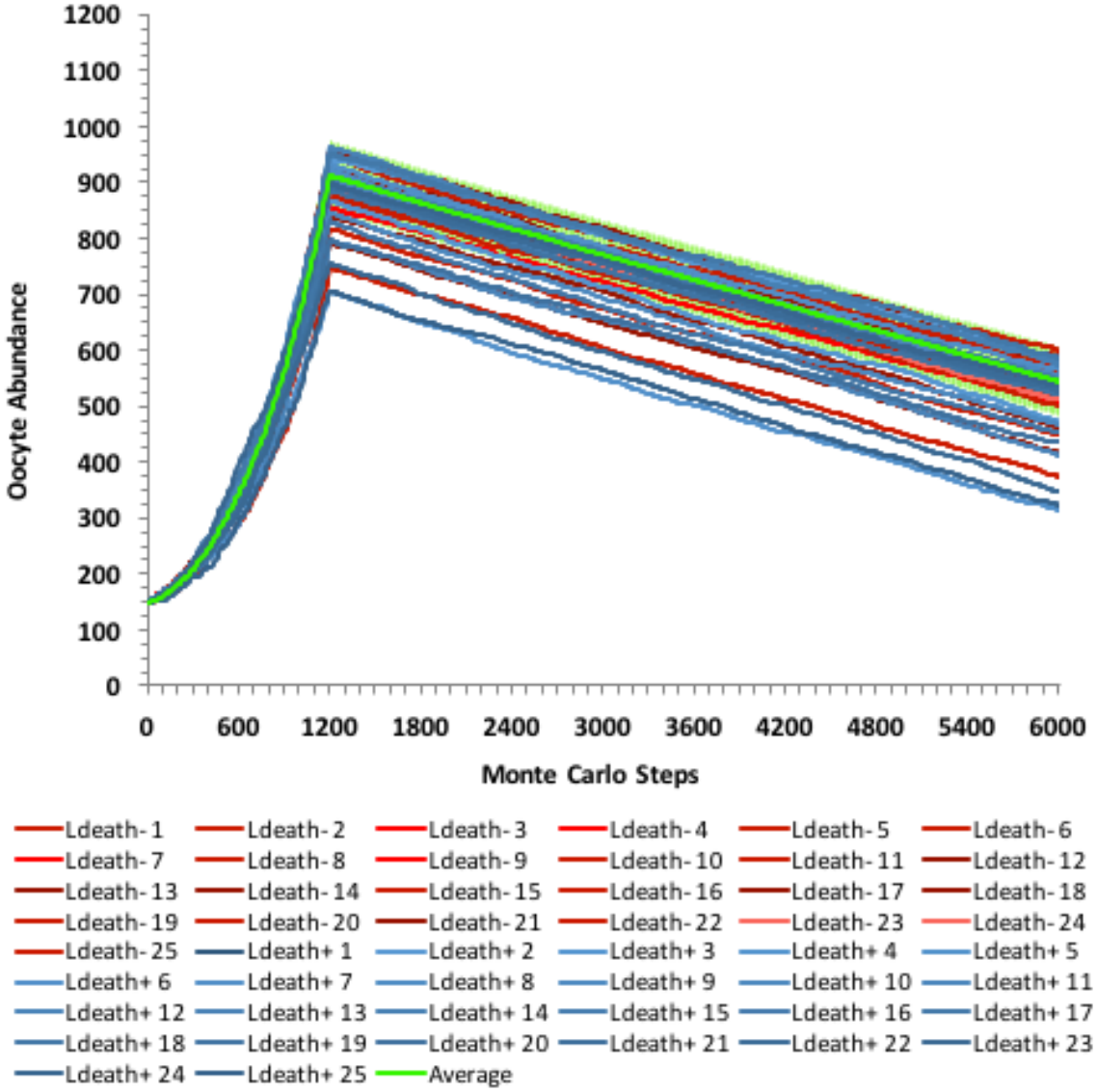


**Fig. 4.17.** Sensitivity analysis for the lambda value for the death rate ($\lambda_{d\tau}$), showing the abundance of oocytes in Phase II of the early ovarian development model. Each line represents one trial simulation with a 10% decrease (reds) or a 10% increase (blues) to the original parameter value. The green line shows the average ± one standard deviation of all simulations run under normal conditions.

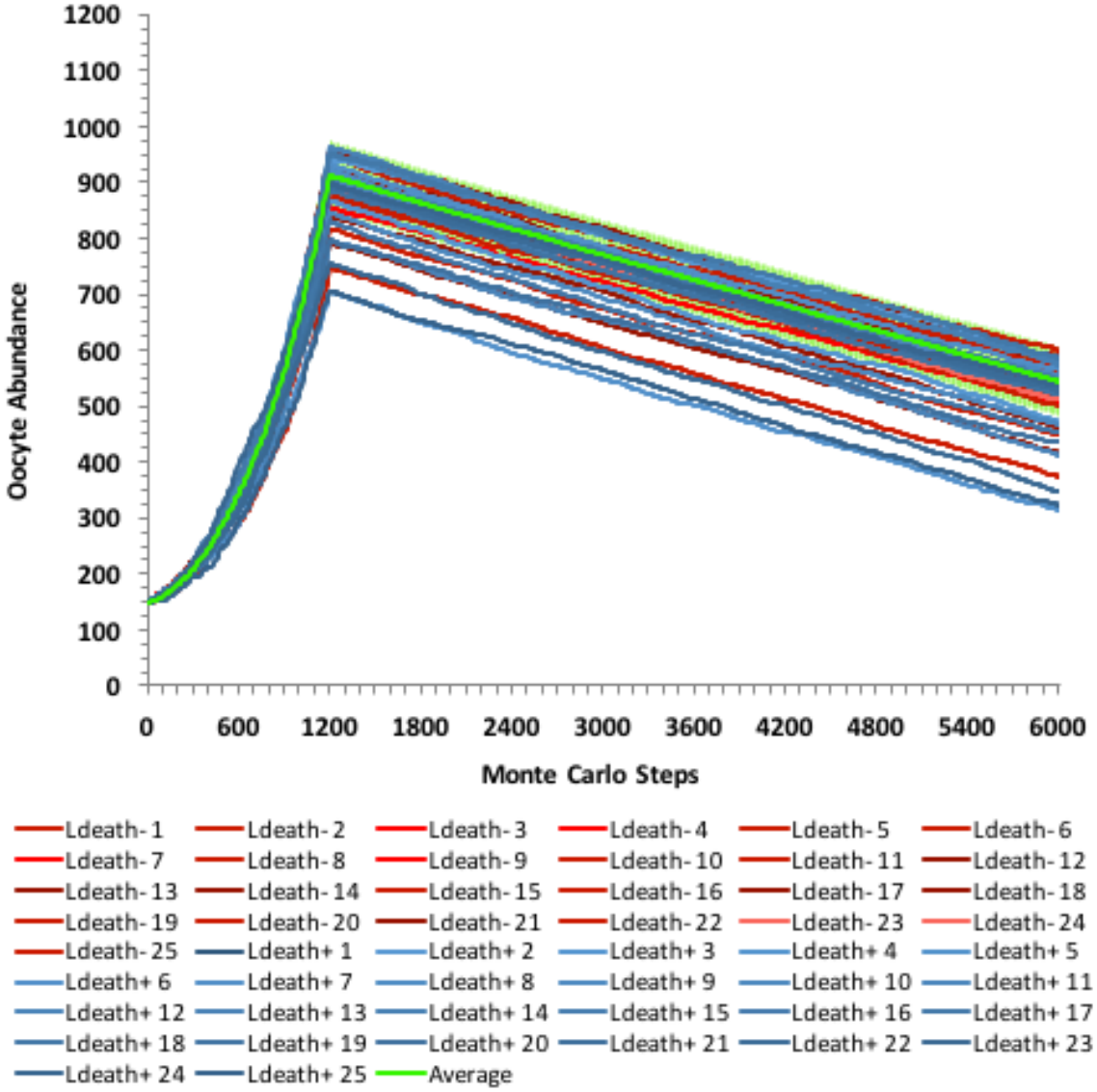


**Fig. 4.18.** Sensitivity analysis for the mitotic rate of all cells in Phase II ($m_{\tau'}$), showing the abundance of oocytes in Phase II of the early ovarian development model. Each line represents one trial simulation with a 10% decrease (reds) or a 10% increase (blues) to the original parameter value. The green line shows the average ± one standard deviation of all simulations run under normal conditions.

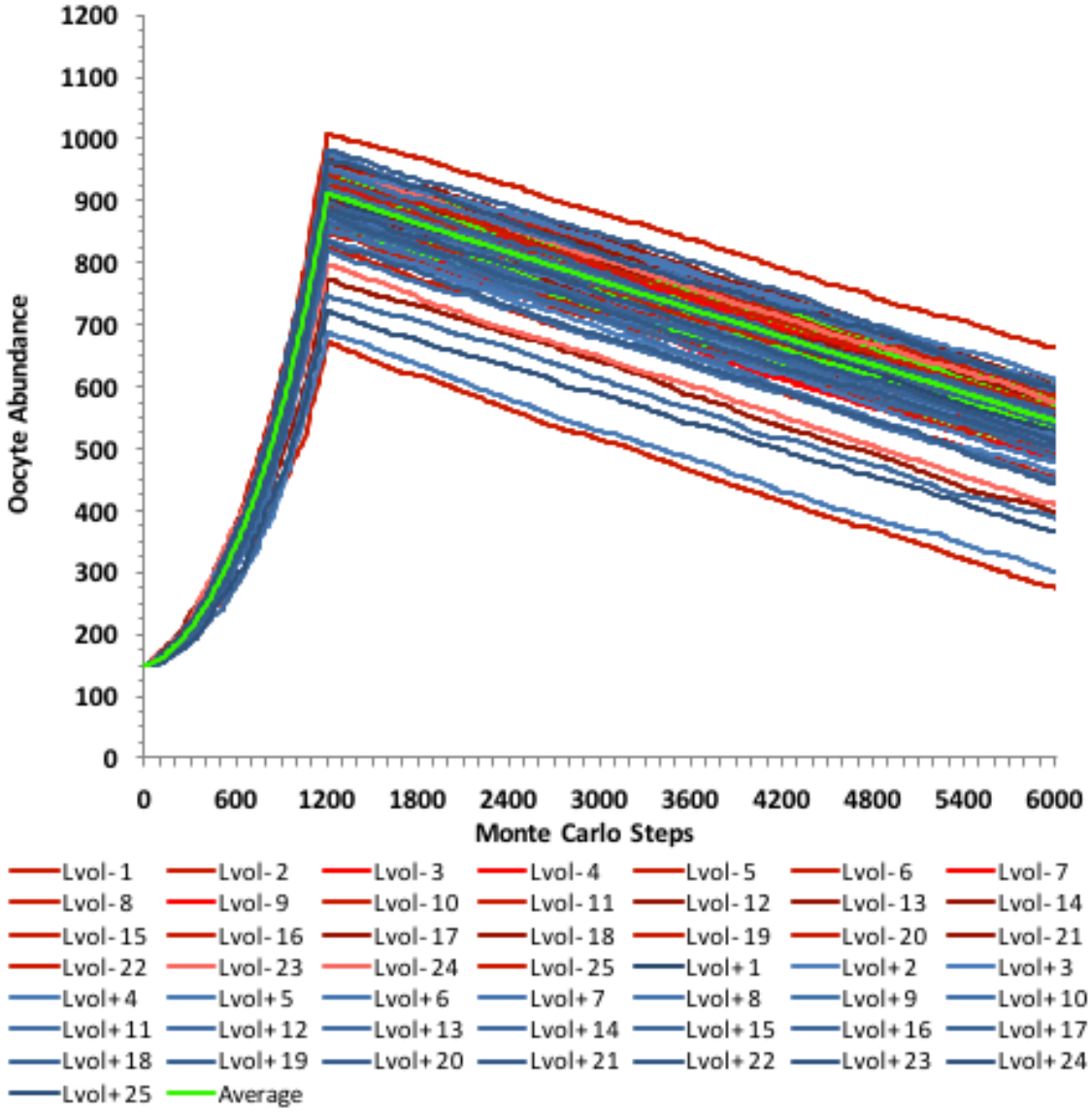


**Fig. 4.19.** Sensitivity analysis for the lambda value for the target volume ($\lambda_{V_T}$), showing the abundance of oocytes in Phase II of the early ovarian development model. Each line represents one trial simulation with a 10% decrease (reds) or a 10% increase (blues) to the original parameter value. The green line shows the average ± one standard deviation of all simulations run under normal conditions.

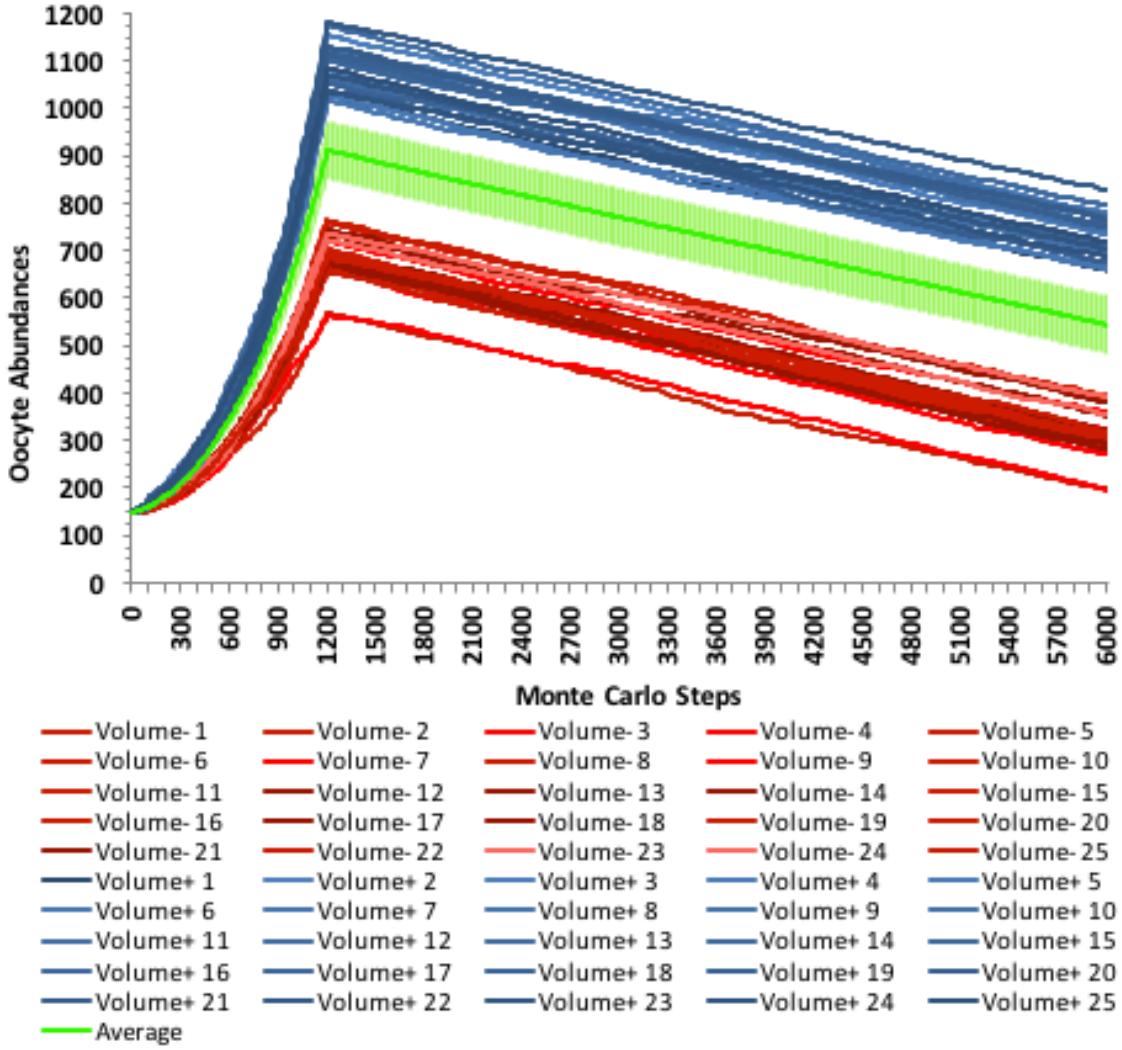


**Fig. 4.20.** Sensitivity analysis for the target volume ($V_{\tau}$), showing the abundance of oocytes in Phase II of the early ovarian development model. Each line represents one trial simulation with a 10% decrease (reds) or a 10% increase (blues) to the original parameter value. The green line shows the average ± one standard deviation of all simulations run under normal conditions.

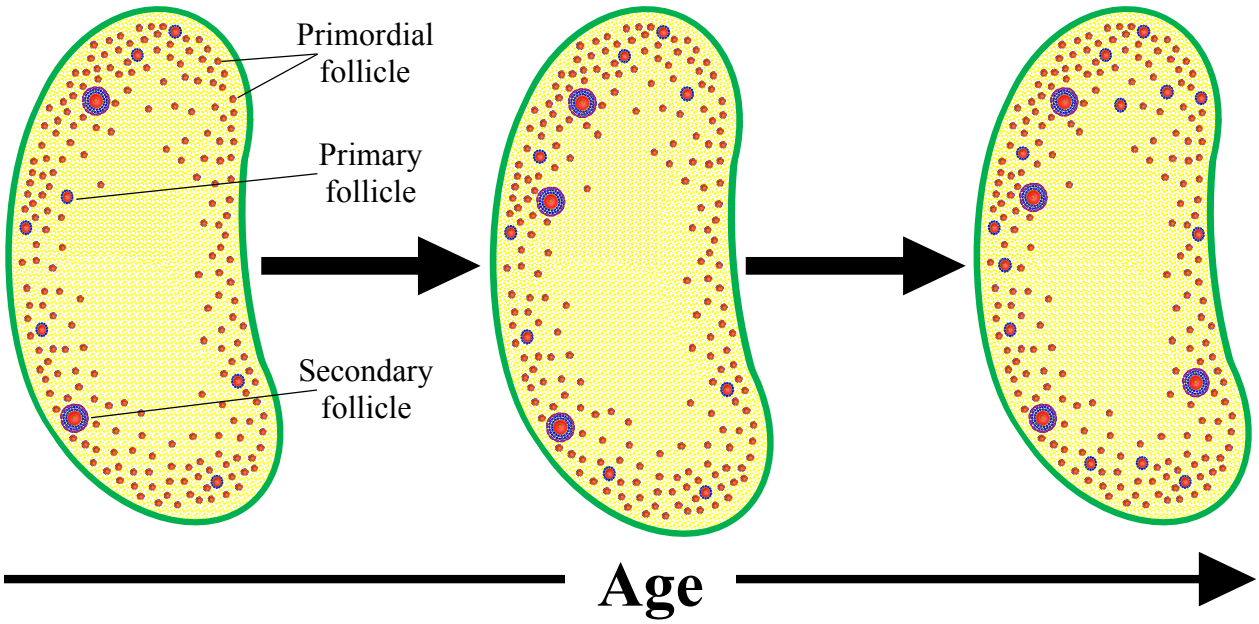


**Fig. 5.1.** Representation for the expected simulation results of the model. The model will simulation the growth of multiple follicles in the whole monkey ovary from primordial to secondary stages. The figure shows an increase in the abundance of secondary follicles and a decrease in the abundance of primordial follicles as age increases. Cell types shown are oocytes (red), granulosa cells (blue), theca cells (magenta), somatic cells (yellow), and epithelial cells (green).

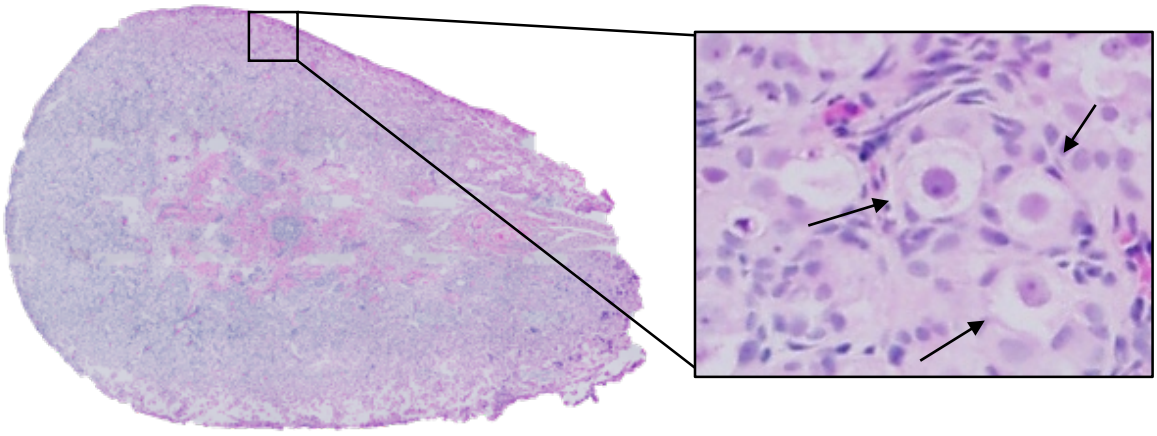

**Fig. 5.2.** An H&E stained section of ovarian tissue from a gestational day 130 rhesus macaque. The abundance of follicles in this tissue sample and morphology are the most representative of the average follicle counts and morphology of all H&E tissues sections analyzed in this study. Close-up section of ovary shows primordial follicles present in ovary (shown by arrows). Animal ID 22724, slide 10C, 1st tissue sample.